uOttawa

L'Université canadienne
Canada's university

FACULTÉ DES ÉTUDES SUPÉRIEURES ET POSTOCTORALES

uOttawa

L'Université canadienne
Canada's university

FACULTY OF GRADUATE AND POSDOCTORAL STUDIES

Xiaoping Tian

AUTEUR DE LA THÈSE / AUTHOR OF THESIS

M.A.Sc. (Civil Engineering)

GRADE / DEGREE

Department of Civil Engineering

FACULTÉ, ÉCOLE, DÉPARTEMENT / FACULTY, SCHOOL, DEPARTMENT

Modeling Reinforced Concrete Cracking Due to Corrosion with a Fracture Mechanics Approach

TITRE DE LA THÈSE / TITLE OF THESIS

Dr. B. Martin-Perez

DIRECTEUR (DIRECTRICE) DE LA THÈSE / THESIS SUPERVISOR

CO-DIRECTEUR (CO-DIRECTRICE) DE LA THÈSE / THESIS CO-SUPERVISOR

EXAMINATEURS (EXAMINATRICES) DE LA THÈSE / THESIS EXAMINERS

Dr. D. Palermo

Dr. M. Mohareb

Dr. Isgor

Gary W. Slater

Le Doyen de la Faculté des études supérieures et postdoctorales / Dean of the Faculty of Graduate and Postdoctoral Studies

MODELING REINFORCED CONCRETE CRACKING DUE TO CORROSION WITH A FRACTURE MECHANICS APPROACH

XIAOPING TIAN

Thesis submitted to the
Faculty of Graduate and Postdoctoral Studies
In partial fulfillment of the requirements
For the MASc degree in name of program

Department of Civil Engineering
Faculty of Engineering
University of Ottawa

Your file Votre référence
ISBN: 978-0-494-18473-8
Our file Notre référence
ISBN: 978-0-494-18473-8

Abstract

With the increasing need of developing service life models for corrosion-induced damage in reinforced concrete structures, there has been a movement to model the concrete cover as a thick-wall cylinder subjected to an internal pressure due to corrosion products accumulation on the reinforcing steel. These models allow determining the amount of corrosion product necessary to initiate and propagate cracks along the cover. The first generation of models assume that concrete behaves linearly elastic and that the concrete cover does not have any residual tensile capacity once the tensile strength of the concrete has been reached. More advanced models include the softening behaviour of concrete beyond cracking initiation. This thesis proposes such a model wherein the state stress of the concrete cover due to accumulation of corrosion products is determined by analyzing an equivalent thick-wall cylinder subjected to a uniform internal pressure. Concrete is assumed to be an isotropic material, and deformations due to Poisson's ratio are ignored. To describe the behaviour of concrete in the softening region, a linear relation of stress versus displacement and a constant strain field are assumed. Mathematical expressions that determine the state of stress due to corrosion build-up at any point in the concrete cover are obtained by integrating the softening equations along the concrete cover. Analytical models for cracking initiation as well as longitudinal cracking of the concrete cover are formulated for both unconfined and confined conditions. The latter are the result of the presence of shear stirrups or tie/spiral reinforcement. To determine the validity of these models, their results are compared to published experimental data and finite element analyses. Finally, a parametric analysis using the models is carried out in order to establish the role of significant model parameters on the resulting state of stress of the concrete cover and the associated damage.

Acknowledgments

I am thankful for the financial support provided by the Natural Sciences and Engineering Research Council of Canada (NSERC) during my research period.

Contents

List of Tables

List of Figures

Notation

The following symbols are used in this thesis:

A_{eq} = equivalent area of spiral bar (mm^2/mm)

c = concrete cover thickness (mm)

d = bar diameter (mm)

d_b = reinforcing steel diameter (mm)

E_c = elastic modulus of concrete (MPa)

E_s = elastic modulus of general strength steel (MPa)

E_r = elastic modulus of red rust (MPa)

E = crack front (mm)

F = Faraday's constant (= 96,486.7 C/mol of electrons)

f_c' = concrete compressive strength (MPa)

f_t' = concrete tensile strength (MPa)

G_f = fracture energy (Nm/m^2)

K_r = bulk modulus of red rust (MPa)

i_{cor} = corrosion rate (A/m^2)

l = bar longitudinal length (mm)

l_{eq} = equivalent transfer length (mm)

l_p = characteristic length (mm)

M_r = rust mass (kg)

M_s = steel mass (kg)

n = number of cracks

p_b = outwards bar pressure applying against the internal concrete ring face (MPa)

p_i = pressure acting on the interface between cracked and uncracked concrete surfaces (MPa)

p_i^e = pressure contributed from the uncracked elastic concrete region (MPa)

p_i^s = pressure contributed from the spiral confinement (MPa)

p_0 = pressure acting on the outer concrete surfaces (MPa)

Q_r = rust density (kg/m^3)

Q_s = steel density (kg/m^3)

r = radius of concrete ring where stresses are calculated (mm)

r_b = radius of corroded bar (mm)

r_i = radius of concrete cracking opening tip (mm)

r_m = molecular ratio of iron to rust

r_0 = radius of the concrete ring (mm)

r_s = radius of confinement (mm)

t = time (s)

t_{cr} = time at which concrete cover cracks (s)

u_r = radial displacement (mm)

w = crack opening width at calculation point (mm)

w_c = maximum crack opening width (mm)

ε_{ct} = maximum concrete tensile strain

ε_r = concrete radial strain

ε_s = total strain of the confinement

ε_s^c = strain of the confinement in the cracked concrete

ε_s^e = strain of the confinement in the uncracked concrete

ε_t = concrete tensile strain

ν = Poisson's ratio

Chapter 1. Introduction

1.1. Background

The heavy use of de-icing chemicals on North American reinforced concrete infrastructure is the leading cause of corrosion of the reinforcing bars. The corrosion of reinforcing steel results in the accumulation of corrosion products around the perimeter of the rebars. These corrosion products have a lower density than the parent metal, resulting in a volume increase. The expansion generated by corrosion build-up at the steel/concrete interface induces tensile stresses in the surrounding concrete, and if these stresses exceed the tensile strength of the concrete cover, longitudinal cracking, spalling and/or delamination occurs. Over time, the accumulation of corrosion-induced damage can lead to a decrease in structural capacity. This decrease in strength is due to:

1. Accumulation of cracking in the concrete surrounding the corroding rebar;
2. Decrease in reinforcement cross-sectional area; and,
3. Deterioration of the bond action between the reinforcing steel and the surrounding concrete.

Corrosion-induced cracking of the concrete cover is an important milestone towards assessing the performance of reinforced concrete structures affected by reinforcing steel

corrosion. The time to cover cracking is a meaningful index of the intensity of the corrosive environment to which the structural member is exposed, and estimating this quantity is a necessary step in quantifying the residual structural capacity of affected reinforced concrete elements. Previous attempts at modelling this problem have resulted in two types of models. The first set of models have only been based on observed and recorded data without an attempt to model the actual mechanics of the problem, and thus their applicability is limited to the range of used data. The use of numerical models based on the finite element method has shed light on the variables governing the mechanics of the problem. However, because of their much higher level of sophistication and complexity, they are not likely to be adopted by the professionals in the field. Ideally, engineering models should be both sufficiently accurate to be meaningful and simple enough to be widely used. The development of analytical models with closed-form solutions has been somewhat limited. Modelling corrosion-induced damage in concrete is a complex problem due to the many uncertainties involved, such as the type of corrosion product formed, the rate of corrosion growth, the geometry of corrosion accumulation around the reinforcing bars, and the pressure induced in the concrete by the corrosion build-up.

1.2. Corrosion of reinforcing steel and associated damage

In general, the high-alkaline environment (pH ~ 13) provided by the hydration products of cement protects reinforcing steel from corrosion by creating a very thin layer of iron oxide,

wherein the corrosion rate is minimized to a negligible value. However, this protection is broken (i.e., depassivation occurs) if the pH of the pore solution drops to around 9 due to carbonation of the concrete cover or a sufficient amount of chloride ions reaching the reinforcement (known as the 'chloride threshold'). Once this protection is taken away, iron is oxidized at the anode releasing two electrons according to:

$$Fe \rightarrow Fe^{2+} + 2e^{-} \tag{1.1}$$

Reinforcement that is still in a 'passive' state will act as a cathode, in which oxygen is reduced according to:

$$O_2 + 2H_2O + 4e^{-} \rightarrow 4OH^{-} \tag{1.2}$$

The electrons released at the anode move towards the cathode through the reinforcing steel bar, and the ferrous ion are dissolved into the surrounding concrete pore solution. The hydroxyl ions released at the cathode migrate towards the anode through the electrolyte provided by the pore solution. At the anode, they combine with the dissolved ferrous ions to yield ferrous hydroxide, i.e.,

$$Fe^{2+} + 2OH^{-} \rightarrow Fe(OH)_2 \tag{1.3}$$

If sufficient oxygen is available at the anodic sites, ferrous hydroxide can be further oxidized into other corrosion products. It is the transformation of ferrous ions into higher oxidation states that results in an increase in volume, since these corrosion products have a lower density than that of the original steel of the reinforcing bar. Depending on the level of

oxidation, this increase in volume can be as much as six times the original one.

Since the reinforcing steel bar is embedded in concrete, the increase in volume of the reinforcing steel due to the accumulation of corrosion products generates a pressure against the surrounding concrete, where tensile stresses are induced. If the tensile capacity of the surrounding concrete is exceeded, the concrete starts cracking, eventually leading to longitudinal cracking and/or spalling/delamination of the concrete cover (see Fig.1.1). This corrosion-induced damage results in two serious effects. One is that the reinforcing steel bar loses the physical protection provided by the surrounding concrete against further penetration of aggressive agents that accelerate the corrosion process (e.g., chloride ions, moisture, and oxygen). The other is that the bond action between the reinforcing steel and the concrete is jeopardized as the intensity of the cover cracking increases. This reduction in bond resistance over time can lead to serious structural consequences, especially at anchorage zones if the problem is left unattended.

There are other factors that also affect the cracking process of the concrete cover. Reinforced concrete structures affected by corrosion are also sustaining mechanical loads as well as other types of environmental-related loads such as those created by freeze and thaw cycles. Moreover, concrete confinement provided by shear stirrups or tie/spiral reinforcement plays a positive role in this process, delaying the appearance of corrosion-induced cracks.

Fig. 1.1: Corrosion-induced damage in reinforced concrete

In order to accurately estimate the induced stresses in the surrounding concrete cover, the following two phenomena must be expressed mathematically: (a) the corrosion process and the build-up of its products around the steel bar; and, (b) the initiation and propagation of cracks from the steel/concrete interface to the outer surface of the concrete cover.

1.3. Objectives of the study

The objective of this thesis is to develop an analytical model capable of predicting the concrete cover cracking resistance due to reinforcing steel corrosion. The mechanical problem is modelled by assuming the concrete cover to be a thick-wall cylinder subjected to the internal pressure resulting from the corrosion products build-up. The purpose of this model is to describe the relationship between the pressure produced by corrosion growth and the stresses developed in the surrounding concrete, and to identify key parameters governing

the concrete cover resistance to the corrosion-induced load. An important aspect of the work presented herein is that it takes into account the residual tensile capacity of concrete once cracking has initiated by means of a fracture mechanics approach.

1.4. Outline of the thesis

Chapter 2 provides a literature review of previously published analytical models that describe the cracking resistance of the concrete cover due to pressure induced by either corrosion growth or bond stresses. Chapter 3 presents the formulation of the proposed analytical model, which determines the amount of pressure necessary to initiate cracking at the steel/concrete interface and propagate those cracks through the concrete cover. Chapter 4 compares model results with published experimental data of the associated mechanical problem and finite element analysis. Chapter 5 presents the parametric analysis conducted with the proposed model in order to identify the role of key model parameters on the cracking resistance of the concrete cover. Finally, concluding remarks and suggestions for future work are listed in Chapter 6.

Chapter 2. Literature Review

2.1. Introduction

The corrosion mechanism of most published service life models is idealized as two main stages as proposed by Tuutti (1982):

Stage 1, Initiation phase, during which chloride ions penetrate through the concrete cover and begin to accumulate around the steel bar surface. The end of this stage corresponds to steel depassivation due to accumulation of chlorides above a threshold value.

Stage 2, Propagation phase, during which the accumulated corrosion products induce a large pressure against the interface between the surrounding concrete and the steel bar, and eventually cause the concrete cover to crack when its tensile resistance is reached. Many service life models define this point as the "service life end" (Weyers, 1998).

Chloride-induced corrosion of reinforcement is a very complicated process and is affected by many factors. The length of both stages outlined above is dependent on the chloride ion concentration in concrete, concrete porosity and distribution, depth of concrete cover, as well as its fracture properties. During the whole corrosion process, corrosion products around the steel bar surface gradually accumulate and exert pressure against the interface between the bar and the surrounding concrete. Once the pressure reaches the tensile capacity at the surrounding concrete, a crack starts to develop. At the same time, the bar cross-section area reduces significantly and the bond action between the rebar and the concrete is compromised. The time for the corrosion growth induced pressure to reach a critical value depends on many factors such as the rate of corrosion product accumulation, density of corrosion products, current that flows through the steel bar, concrete and steel physical properties, concrete cover depth, bar locations, and the degree of concrete confinement.

The relationship between this critical pressure and the corrosion products build-up is a necessary step for engineers to estimate the damage degree that occurs in reinforced concrete structures affected by reinforcing steel corrosion.

2.2. Modelling corrosion build-up

The volume of corrosion products deposited around the reinforcing bar may expand as 6 times the original steel bar volume. The ratios ξ of the volumes of various rust products to that of their original parent metal are listed in the following (Liu and Weyers, 1998):

$\xi FeO = 1.7$ $\xi Fe_3O_4 = 2$ $\xi Fe_2O_3 = 2.1$,

$\xi Fe(OH)_2 = 3.6$ $\xi Fe(OH)_3 = 4.0$ $\xi Fe(OH)_3 3H_2O = 6.15$

Since the molecular weight of iron is equal to 55.85 g/mol, the molecular ratio of iron to rust, denoted as r_m, is taken as 0.523 for hydrated red rust $Fe(OH)_3$ and 0.622 for ferrous hydroxide $Fe(OH)_2$. Actually, the real volume ratio usually varies in different pore solutions of cement matrix in concrete. It is very difficult to assign a value for this ratio because the components of the corrosion products are complex. For the sake of simplicity, the density ratio ξ of rust to its parent metal is usually fixed within the range of 2 to 4 (Liu and Weyers, 1998). It is this density discrepancy between iron and its corrosion products that causes the volume of the reinforcing steel bar to increase rather than decrease during corrosion.

Faraday's law establishes a relationship between the consumed iron mass dM_s/dt and the current amount i_{cor} going through the steel bar as:

$$dM_s/dt = i_{cor}A/(nF) \tag{2.1}$$

where A is the atomic mass of iron, taken as 55.85 g/mol, F is Faraday's constant (96,500 C/mol), n is the atomic valency, which is 2 mol because it is impossible to exactly know all the components of the corrosion products, i_{cor} is the current amount that flows through the metal conductor and is assumed a constant value during the corrosion process.

When integrating Eq.2.1 with respect to time from corrosion initiation to time t, the total

iron mass consumed during this period is obtained as M_s. It is easy to conclude that Faraday's law shows a linear relationship between the consumed iron mass and the time duration of the corrosion propagation stage.

Once the consumed iron mass is known, the produced rust mass M_r can be obtained based on the relationship of $M_s=M_r r_m$, where r_m is the molecular ratio of iron to rust, usually taken as 0.523 for hydrated red rust $Fe(OH)_3$ and 0.622 for ferrous hydroxide $Fe(OH)_2$ (Bažant, 1979; Liu and Weyers, 1998). From the consumed iron mass M_s and produced rust mass M_r, the final volume increase of the reinforcing steel bar can be calculated by subtracting the iron volume from the rust volume. If a fracture mechanics approach is used, the internal bar pressure exerted by the corrosion build-up can be finally set up as a function of the bar radial strain ε_r, which is dependent on the volume increase of the reinforcing steel bar.

Many of the models found in the literature, which simulate the corrosion of reinforcement in reinforced concrete structures (Bažant, 1979; Andrade et al, 1993; Liu and Weyers, 1998; Pantazopoulou and Papoulia, 2001), established the relationship between the internal pressure and the time to cover cracking by following five steps. These are:

Step 1: formulate the relationship between internal bar pressure (p_b) around the bar and the bar's radial strain (ε_r) such that p_b can be a function of ε_r (assuming linear behaviour), as shown below:

$$p_b = \varepsilon_r E_r / [2(1+v)(1-2v)] \approx 2\varepsilon_r \text{ [GPa]} \qquad (2.2)$$

where ε_r is the unknown rebar radial strain, calculated from initial status to current status, E_r is the elastic modulus of red rust and equal to $3(1-2v)K_r$, v is the Poisson's ratio of red rust (given as 0.499, Molina et al, 1993), and K_r is the bulk modulus of red rust (taken as 2 GPa). The relationship between internal bar pressure P_b and bar's radial strain ε_r is illustrated in Fig. 2.1.

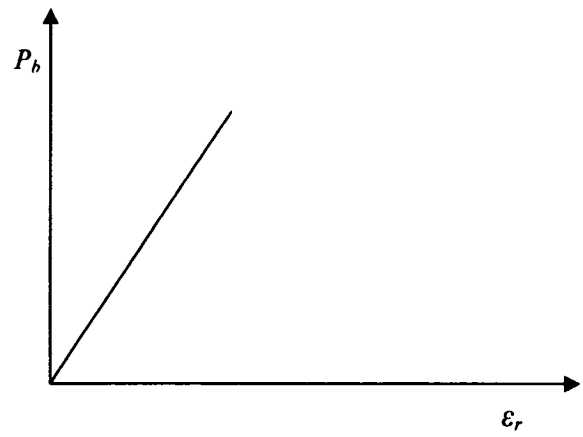

Fig. 2.1: Internal pressure-strain relationship in the radial direction

Step 2: build the equation between the bar volume increase (ΔV) and its strain ε_r:

$$\varepsilon_r = \Delta V/V = \frac{4\Delta M_r}{\pi d_b^2}\left(\frac{1}{Q_r} - \frac{0.523}{Q_s}\right) \approx 5.6478\times10^{-4}\ \frac{\Delta M_r}{d_b^2} \qquad (2.3)$$

where d_b is the original bar diameter, ΔV is equal to V_1-V_o (V_o is the reduced consumed rebar volume and V_1 is the increased red rust volume, see step 3), Q_s is the density of steel (7.85×10^3 kg/m^3), Q_r is the density of hydrated red rust (about 1.96×10^3 kg/m^3), and ΔM_r is the increase in red rust mass. The relationship of volume increase-ΔV and bar's radial strain-ε_r is illustrated in Fig. 2.2.

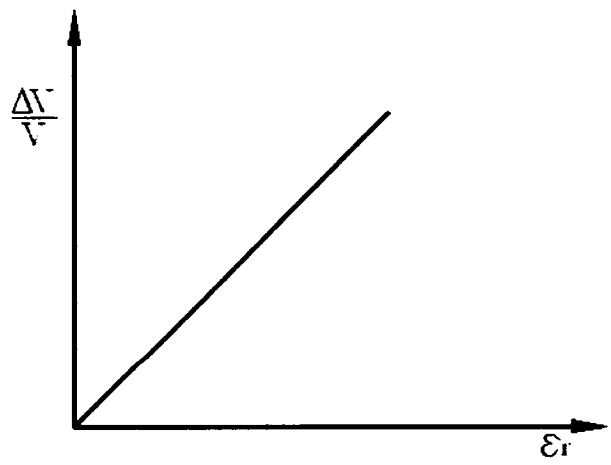

Fig. 2.2: Relationship of bar volume increase and radial strain

Step 3: deduce the relation between bar volume increase and the consumed iron mass

amount, as well as increased red rust mass amount:

$$V_1 = \Delta M_r / Q_r \tag{2.4}$$

$$V_o = \Delta M_s / Q_s \tag{2.5}$$

where ΔM_s is the consumed steel rebar mass.

Step 4: find the iron mass amount participating in the electro-chemical corrosion reactions. It can be a function of both the corrosion current i_{cor} and corrosion time Δt:

$$\Delta M_s = f(\Delta t, i_{cor}) \tag{2.6}$$

where Δt is the corrosion time, and i_{cor} is the mean annual corrosion current per unit anodic surface area of rebar. The mass of iron ΔM_s consumed over time Δt is related to the amount of current i_{cor} that flows through the electrochemical corrosion cell including anodic and cathodic bar areas, as well as the pore solution through which irons are conducted. This process is prescribed by Faraday's law as $\Delta M_s/\Delta t = i_{cor} A/(nF)$, where A is the atomic weight of iron being dissolved, and Faraday's constant F=96,500 C/mol. The valency of the reaction n is empirically usually taken as 2 (since little is known about the chemical composition of the corrosion products, all corrosion products are assumed to be $Fe(OH)_2$). It follows that $\Delta M_s/\Delta t = 2.893x10^{-4}\ i_{cor}$. Integration of $\Delta M_s/\Delta t$ gives the total mass of iron consumed since initiation of corrosion. The constant i_{cor} is quantified as $i_{cor}\pi d_b l$, where l is the anode length, d_b is the rebar diameter, and i_{cor} is the mean annual corrosion current per unit anodic surface area of steel. Faraday's law is the basis for all published models that assume a constant rate of steel mass consumption and rust production. Faraday's law implies a linear increase of the mass of rust with time. Under certain assumptions, all models are particular instances of Faraday's law.

Step 5: obtain the transformation relationship between ΔM_r and ΔM_s:

$$\Delta M_r = \Delta M_s / r_m \tag{2.7}$$

where r_m is the ratio of iron to its rust products for hydrated red rust $Fe(OH)_3$ (taken as 0.523, Bažant, 1979).

For all the preceding steps, step 4 presents the most difficulty. Different researchers have provided different approaches, which are summarized in the following sections.

2.2.1 Bažant's model (1979)

In this model, Bažant's (1979) defined the rate of red rust production as $J_r = dM_r / dt = 5.536 \times 10^{-7}\ i_{cor}$ (kg/m^2·s). Within every unit length of bar surface, the accumulated red rust mass ΔM_r can be calculated from $\pi d_b J_r \Delta t$. Because the mass ratio of iron to hydrated red rust r_m is equal to 0.523, the mass and volume of bar consumed are calculated from:

$$\Delta M_s = 2.895\times10^{-7}\ \pi\ d_b\ i_{cor}\ \Delta t \text{ (kg/m)} \tag{2.8}$$

$$\Delta V_s = 3.68\times10^{-11}\ \pi\ d_b\ i_{cor}\ \Delta t \text{ (m}^3\text{/m)} \tag{2.9}$$

Eq. 2.8 coincides with Faraday's law. The volume change of the bar due to corrosion build-up is estimated from:

$$\Delta V = (\Delta M_r/Q_r) - (\Delta M_s/Q_s) = 1.107\times10^{-10}\pi\ d_b\ i_{cor}\ \Delta t \text{ (m}^3\text{/m)} \tag{2.10}$$

In the above expression, Q_r is equal to Q_s / 2.09 (approximately 3.75×10^3 kg/m^3).

2.2.2 Andrade et al's model (1993)

According to many experimental results, Andrade et al (1993) developed an empirical formula to describe the relationship between the consumed volume ΔM_s of steel bar at the bar anodic surface and the current density i_{cor} (μA/m^2). Compared with the steel bar's diameter, the consumed bar thickness is very thin and is ignored in the analysis of this model. Thus ΔM_s and ΔV_s are given by:

$$\Delta M_s = 2.862\times10^{-7}\ \pi\ d_b\ i_{cor}\ \Delta t \text{ (kg/m)} \tag{2.11}$$

$$\Delta V_s = 3.6466\times10^{-11}\ \pi\ d_b\ i_{cor}\ \Delta t \text{ (m}^3\text{/m)} \tag{2.12}$$

where ΔM_s is the consumed bar mass (kg), d_b is the steel bar initial diameter (m), and Δt is the time elapsed from corrosion (second).

2.2.3 Liu and Weyers' model (1998)

Liu and Weyers (1998) considered the rate of rust production as a non-linear function of time, i.e.,

$$\int M_r dM_r = \beta \int dt \Rightarrow M_r = \sqrt{6.656 \times 10^{-10} \pi d_b i_{cor} t} \quad (2.13)$$

where β is a function of the corrosion current in consistent units. According to Eq. 2.13 the time needed for the rust mass accumulated around the steel bar to reach a critical value is clearly longer than that in Bažant's (1979) and Andrate et al's (1993) models.

2.2.4 Pantazopoulou and Papoulia's model (2001)

Pantazopoulou and Papoulia proposed in their model that rust could be deposited in the space between cracks and consequently the pressure acting on the interface between rebar and surrounding concrete would be reduced. Based on this theory, a certain amount of liquid rust product is carried away from the rust layer and then directly deposits in the opening cracks until the space is full. After all cracks are filled with this liquid rust, only the extra liquid rust product contributes to the internal pressure acting on the surrounding concrete. Therefore, the mass amount used for the calculation of the rust volume expansion in the radial direction should be equal to the difference between the total rust mass produced and the leaking mass depositing in the opening crack spaces. If t_r is denoted as the reduced thickness of the rebar during the corrosion process and ΔV_r is the expanded volume in this process, then t_r can be expressed as a function of ΔV_r and the reduced bar radius-R_{rb}, as shown below:

$$t_r = \sqrt{R_{rb}^2 + \frac{\Delta V_r}{\pi}} - R_{rb} \quad (2.14)$$

After the liquid rust goes into the space of the cracks, the above formula can be adjusted into the following equation:

$$t_r = \frac{(\Delta V_r / \pi) - (R_{rb} - R_b)(R_c - R_{rb})}{(R_c + R_b)} \quad (2.15)$$

where R_b is the initial rebar radius and R_c is the crack front depth measured from the rebar center to the crack end, see Fig.2.3.

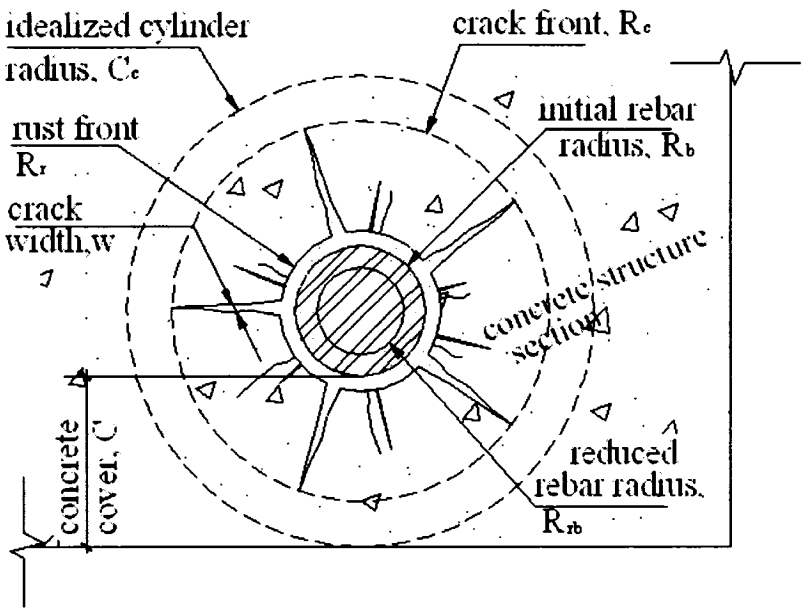

Fig. 2.3: Definition of terms in thick-wall cylinder model

Once the corrosion current density i_{cor} is determined from experiments, the volume change for the rust products and the thickness t_r is calculated. The thickness t_r is related to the concrete radial strain "ε_r" along the radial direction. Tensile capacity of the surrounding concrete is a function of ε_r. If the initial boundary condition for ε_r is known, the stresses in concrete can be solved at any time. Similarly, the maximum stress at which the surrounding concrete starts splitting can also be found. As a result, the cracking time due to corrosion build-up can be predicted.

2.2.5 Summary of corrosion-growth models

By using the different models in the above sections in step 4, the final relationship between corrosion time, consumed iron mass ΔM_s, and internal pressure p_b are explicitly summarized in Table 2.1.

Table 2.1: Summary of corrosion-growth models

Models	ΔM_s (kg)	p_b (MPa)
Bažant (1979)	$2.898\times10^{-7}\pi\, d_b\, i_{cor.}\, \Delta t$	$1.96\times10^{-6}\frac{i_{cor}\Delta t}{d_b}$
Andrade et al (1993)	$2.862\times10^{-7}\pi\, d_b\, i_{cor.}\, \Delta t$	$1.94\times10^{-6}\frac{i_{cor}\Delta t}{d_b}$
Liu and Weyers (1998)	$(6.656\times10^{-10}\pi\, d_b\, i_{cor.}\, \Delta t)^{1/2}$	$1.96\times10^{-6}\frac{i_{cor}\Delta t}{d_b}$
Pantazopoulou and Papoulia (2001)	Refer to Eqs. used	Refer to Eqs. used

2.3 Modelling cracking of the concrete cover

As the corrosion process progresses, corrosion products deposit around the surface of the reinforcing steel bar leading to a volume increase. As a result, the surrounding concrete is subjected to tensile stresses. If these stresses exceed the concrete tensile strength capacity, cracking of the concrete cover occurs. This phenomenon has been modeled by many researchers as a thick-wall concrete cylinder subjected to a uniform internal pressure (Tepfers, 1979; Noghabai, 1995; Seki and Oya, 1996; Pantazopoulou and Papoulia, 2001), as illustrated in Fig. 2.4.

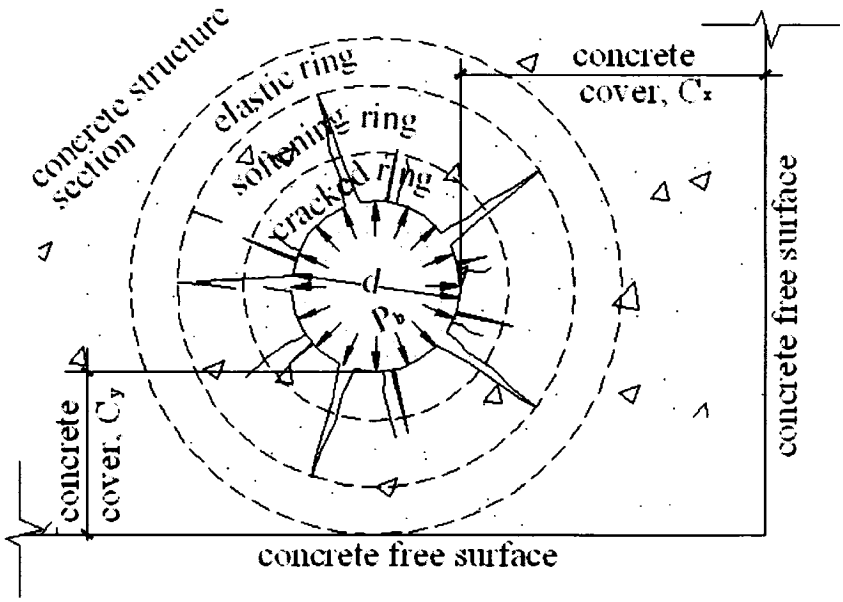

Fig. 2.4: Concrete thick-wall cylinder model

When the thick-wall concrete cylinder is subjected to an internal pressure p_b, which is caused by expansion of the volume of the corroded steel bar, tensile stresses are developed in the surrounding concrete. Once the concrete tensile capacity is exceeded, concrete starts cracking. As the internal pressure increases, the length of cracks develops until reaching the most outer surface of the concrete cylinder. The thick-wall concrete cylinder can be viewed as consisting of three zones: an intact part (elastic part), a micro-cracking part (softening part), and a traction-free part (refer to Fig. 2.4).

In early models based on the theory of linear elastic fracture mechanics (LEFM), concrete was only modeled as an elastic material, in which the tensile stresses in concrete are calculated according to Hooke's law, i.e., $\sigma = E\,\varepsilon$, where σ is the stress in concrete, E is the concrete elastic modulus, and ε is the strain in concrete. Stress varies from zero to a maximum value corresponding to the concrete tensile strength capacity. After this peak value is reached, the stress drops to zero (shown in Fig. 2.5).

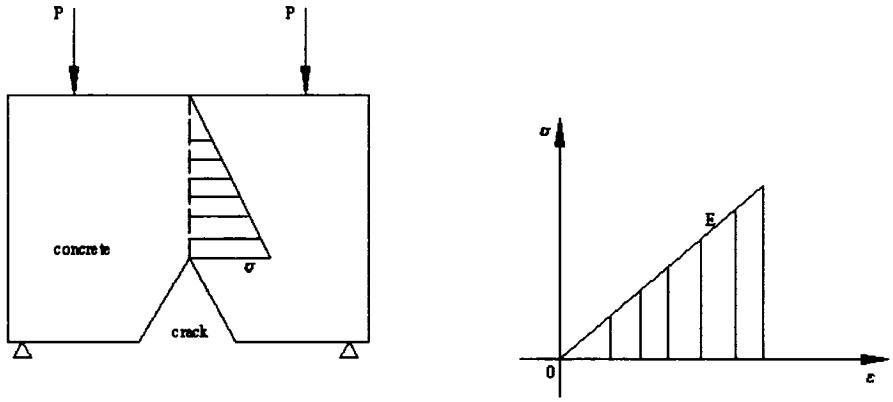

Fig. 2.5: Tensile elastic stress-strain curve

Later, however, with the development of analysis techniques, many experimental studies have demonstrated that concrete still sustains tensile stresses after cracking initiation. In the experiment of a notched concrete beam subjected to a tensile load, Karihaloo (1995) observed deformations of an outspread fracture process zone ahead of the pre-existing notch/crack. The concrete in this area exhibits a softening behaviour as illustrated in Fig.2.6. Both the linear behaviour prior to reaching the tensile strength of concrete (curve AB in Fig. 2.6) and softening behaviour beyond exceeding tensile capacity (curve BD) were observed by Karihaloo (1995). The last region (CD) is caused by aggregate interlock and other frictional mechanisms.

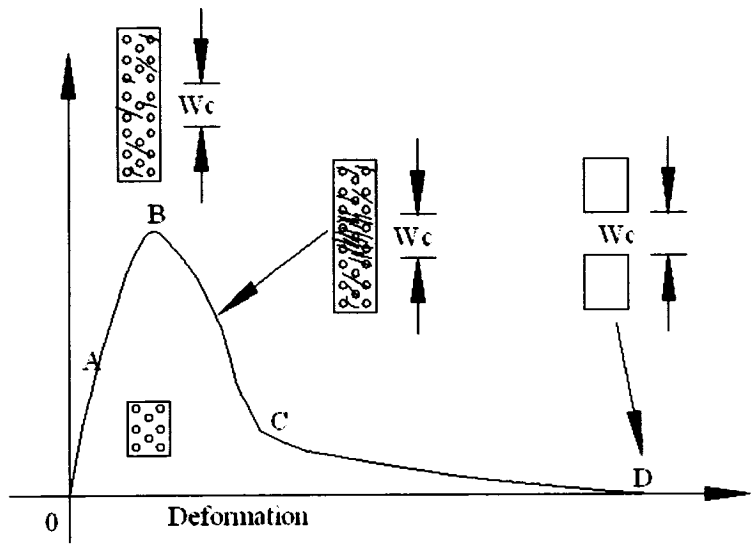

Fig. 2.6: Deformation response of a loaded concrete specimen

When subjected to a tensile force, concrete experiences this softening behaviour in a

zone called the fracture process zone (FPZ). Microcracks form within the FPZ. Along with the increase of load, these microcracks tend to connect to each other, always seeking the least resistance path to go through, as shown in Fig. 2.7.

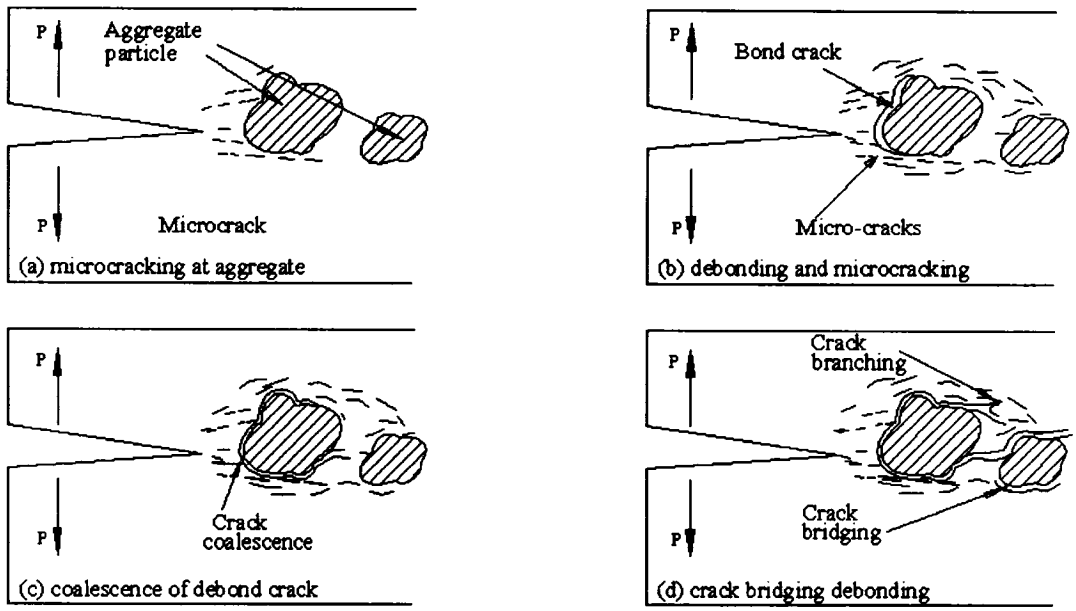

Fig. 2.7: Development of fracture process zone (Karihaloo, 1995)

Under the electron microscope, many micro-phases, such as crack bridging, micro-cracks, and crack coalescence were observed in FPZ by researchers. These micro-phases play very important roles in sustaining the concrete tensile capacity. In the FPZ, microcracks are not continuous and called fictitious cracks. The term "fictitious" is used to underline the fact that this portion of the crack cannot be continuous with full separation of its faces as in a real traction-free crack, see Fig. 2.7.(c). In the FPZ, the appearance of microcracks means the loss of tensile capacity in the direction perpendicular to the cracks. Long cracks mean large loss of strength capacity and short cracks mean small loss of strength capacity.

The difference between the FPZ model and LEFM model is very obvious. First, unlike the LEFM model, the size of the fracture process zone may not be small in comparison with the length of the pre-existing macrocracks. Second, unlike the LEFM model, the adjacent stresses in the FPZ are not constant. They vary from zero at the ends of the pre-existing

traction-free macrocracks to the full tensile strength f_t' at the tips of the fictitious cracks. Therefore, in FPZ models, the relationship of stress σ and fictitious crack width w is used instead of that of stress σ and strain ε. Once this relationship is figured out by applying the concrete ring model, an equation can be set up between the internal bar pressure caused by the rebar volume expansion during the corrosion process and the induced tangential and radial stresses in the surrounding concrete.

In the following sections, different relationships for the tensile softening behaviour in concrete used by various researchers, such as Tepfers (1979), Van der Veen (1990), Reinhardt (1992), Rosati and Schumm (1992), and Pantazopoulou and Papoulia (2001), are summarized.

2.3.1 Tepfers' model (1979)

The cracking process is divided into three stages.

1. Elastic stage

This stage corresponds to crack initiation; no material softening takes place. Assuming the concrete cover as a thick-wall cylinder, the internal pressure due to the rebar volume expansion can be written as:

$$\frac{p_b}{f_t'} = \frac{r^2{}_0 - r_b^2}{r_0^2 + r_b^2} \tag{2.16}$$

where P_b is the internal rebar pressure due to corrosion build-up, f'_t is the concrete tensile strength, r_0 is the outer diameter of the thick-wall cylinder, and r_b is the rebar radius.

2. Partially cracked-elastic stage

This stage corresponds to crack development and material softening behaviour. Cracks develop to a maximum depth of $r_i^{max} = 0.486\ r_0$. The internal pressure and induced tangential stress can be formulated as:

$$\frac{p_b}{f_t'} = \frac{r_i}{r_b}\frac{r^2{}_0 - r_i^2}{r_0^2 + r_i^2} \tag{2.17}$$

and

$$\frac{p_b^{max}}{f_t'} = \frac{0.3r_0}{r_b} \tag{2.18}$$

3. Plastic stage

In this stage, the material has reached its maximum capacity in its entirety, i.e., it behaves as a plastic material. The bar internal pressure is calculated from:

$$\frac{p_b}{f_t'} = \frac{r_0 - r_b}{r_b} \tag{2.19}$$

The maximum bond capacity τ_b can be obtained as: $\tau_b = p_b / tan\alpha$, where the angle α is determined by the crushing degree in front of the bar-rib and the geometry of bar-rib. The pressure p_b is assumed constant along the interface between the rebar and concrete. The above three stages can be illustrated in Fig.2.8.

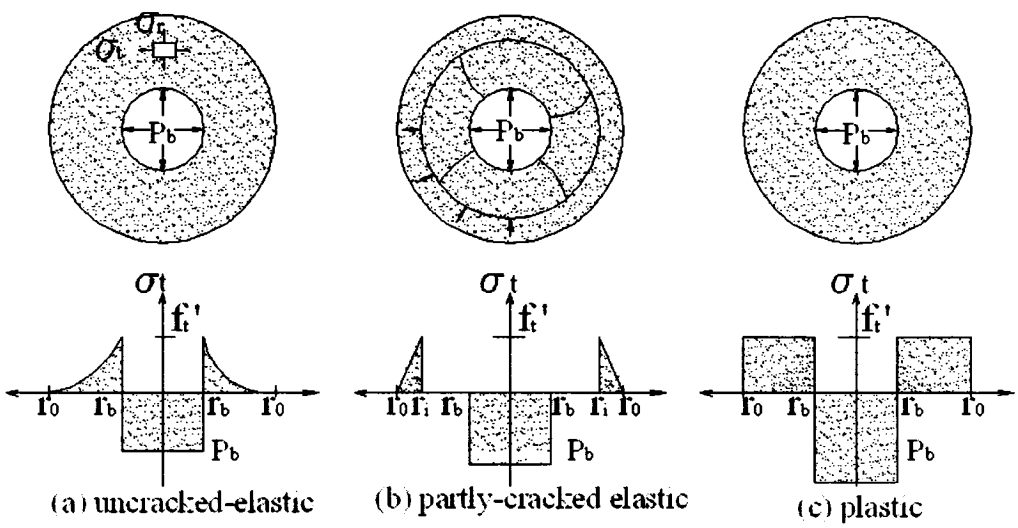

Fig. 2.8: Stress distribution response (Tepfers, 1973)

2.3.2 Van Der Veen's model (1990)

In this model, the softening relation in the cracked region is formulated as:

$$\frac{\sigma_t}{f_t'} = 1 - (\frac{w}{w_c})^k \tag{2.20}$$

where k = 0.248 for a concrete with f_c' = 49 MPa, f'_t = 3.1 MPa, and G_f = 110 N/m (Reinhardt, 1984). The cracked region is limited to $r_b \leq r \leq r_i$. The constant tangential

displacement is calculated as: $u_t = 2\pi \varepsilon_{ct} r_i = nw + 2\pi \varepsilon_t r$ (see Fig. 2.9).

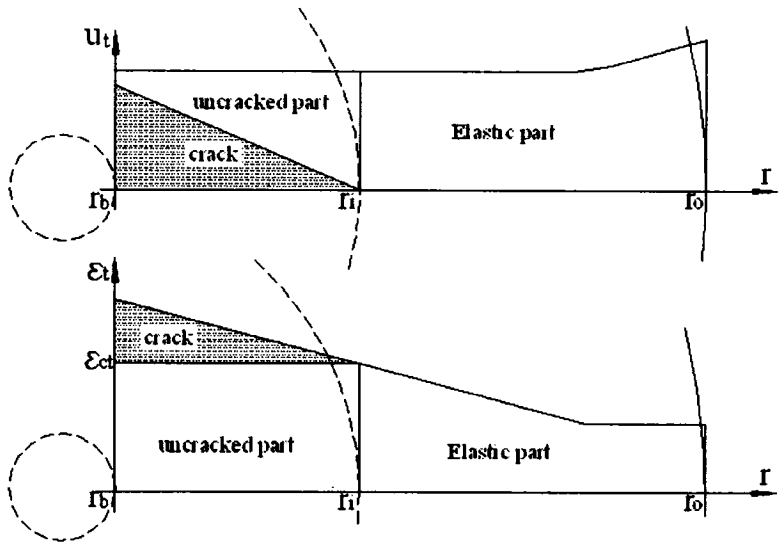

Fig. 2.9: Strain compatibility in the softening region (Van Der Veen, 1990)

The concrete strain in the uncracked region is constant (i.e., $\varepsilon_t(r)=\varepsilon_{ct}$,). The crack width is given by $w(r) = 2\pi \varepsilon_{ct} (r_i - r)$. By introducing the maximum crack width as $w_c=5.14G_f/f_t'$ the internal bar pressure is related to the critical crack location in the concrete cylinder ring as follows:

$$\frac{p_b}{f_t'} = \frac{1}{r_b}\left[r_i\left(\frac{r_0^2 - r_i^2}{r^2{}_0 + r^2{}_i}\right) + (r_i - r_b)\left(1 - \left(\frac{2\pi\varepsilon_{cr}}{nw_c}(r_i - r_b)\right)^k \frac{1}{1+k}\right)\right] \qquad (2.21)$$

By differentiating p_b with respect to r_i and setting the equation to zero, an optimum depth r_i is calculated where the bar pressure is maximum. The maximum bond capacity can be found as $\tau_b^{max} = p_b^{max}/tan(\alpha)$.

2.3.3 Reinnhardt's model (1992)

The relationship between stress σ_t and crack width w in the softening zone is given by:

$$\frac{\sigma_t}{f_t'} = \left[1 + \left(c_1 \frac{w}{w_c}\right)^3\right] e^{-c_c \frac{w}{w_c}} - \left(1 + c_1{}^3\right)\frac{w}{w_c} e^{-c_2} \qquad (2.22)$$

In the above equation, $c_1 = 3.0$, $c_2 = 6.93$ and $w_c = 0.2$ mm, for a concrete with a splitting strength of $f_t' = 3.2$ MPa, a compressive strength of $f_c' = 47$ MPa, and a fracture energy of G_f = 103 N/m.

The cracked region is limited to of $r_b \leq r \leq r_i$. In the softening region, concrete can be divided into an uncracked zone and a cracked zone. In the uncracked zone, concrete still shows elastic behaviour i.e., $\sigma = E\varepsilon$. Meanwhile in the cracked zone, the relation of stress and strain within the crack bandwidth no longer follows Hooke's Law; it varies from point to point. According to the strain compatibility required above, the tangential displacement u_t from the tip of the crack to the end of crack should be a constant value, as shown Fig. 2.10

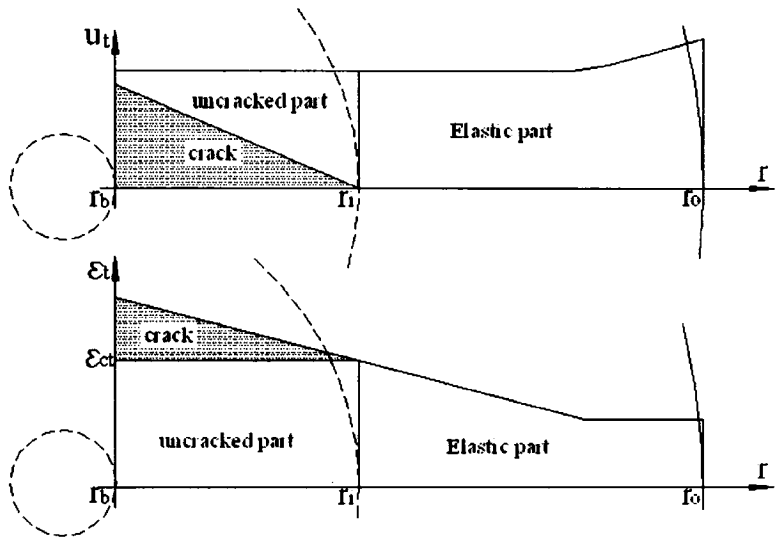

Fig. 2.10: Compatibility in a thick-wall concrete ring (Reinnhardt, 1992)

This displacement is expressed as:

$$u_t = 2\pi\, \varepsilon_{ct}\, r_i = nw + 2\pi\, \varepsilon_t\, r \tag{2.23}$$

where

$$w(r) = 2\pi\, \varepsilon_{ct}\, (r_i - r) \tag{2.24}$$

The pressure of volume expansion due to rebar corrosion can be expressed as a function of r_0, r_b and r_i, as follows:

$$\frac{p_h}{f_t'} = \frac{1}{r_b}\left[r_i\left(\frac{r_0^2 - r_i^2}{r^2{}_0 + r^2{}_i}\right) + \frac{1}{c_2 a}\left(1 - e^{-abc_2}\right) + \right.$$

$$\left. \frac{6c_1^2}{c^4{}_2 a} - \frac{(ac_1)^3}{c_2 a} e^{-abc_2}\left(b + \frac{3b^2}{ac_2} + \frac{6b}{(ac_2)^2} + \frac{6}{(ac_2)^3}\right) - (1 + c_1^3)\, e^{-bc_2}\right] \tag{2.25}$$

where $a = \frac{2\pi\varepsilon_{cl}}{nw_c}$ and $b=r_i-r_b$.

By differentiating p_b in terms of r_i and setting that equation to zero, an optimum depth r_i can be calculated where the bar pressure is maximum. The maximum bond capacity can then be found as: $\tau_b^{max} = p_b^{max}/tan\ (\alpha)$.

2.3.4 Rosati and Schumm's model (1992)

In this model, the equation describing concrete softening in the cracked part is taken as:

$$\frac{\sigma_t}{f_t'} = \frac{1 - w/w_c}{1 + (kw)/D_{max}} \tag{2.26}$$

where D_{max} is the maximum aggregate size, and k is a coefficient depending on the slope of the softening curve as shown in Fig. 2.11.

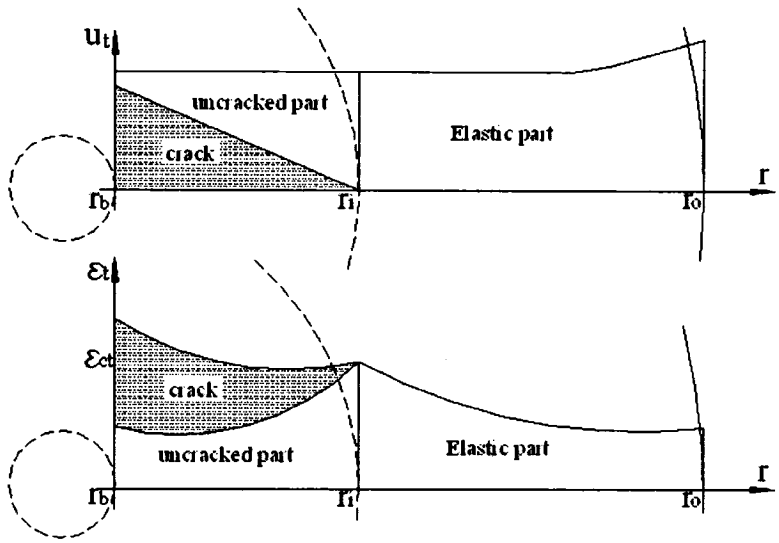

Fig. 2.11: Strain compatibility in the softening zone (Rosati and Schumm, 1992)

The cracked region is limited to $r_b \leq r \leq r_i$. The tangential displacement is calculated from:

$$u_t = 2\pi\ \varepsilon_{ct}\ r_i = nw + 2\pi\ \varepsilon_t\ r \tag{2.27}$$

In the uncracked region, the strain is no longer constant but varies along the radial direction as follows:

$$\varepsilon_t(r) = \frac{\sigma_t(r)}{E_c} \tag{2.28}$$

The pressure of the volume expansion due to rebar corrosion can be formulated as a function of r_0, r_b, and r_i as follows:

$$\frac{p_b}{f_t'} = \frac{r_i}{r_b}\left(\frac{r_0^2 - r_i^2}{r^2{}_0 + r^2{}_i}\right) + \left(\sqrt{A}\ln\frac{r_i}{r_b}\right) - \left[\sqrt{C}l(r_i - 2r_b)\right] -$$

$$\psi[r_i] + \psi[r_b] - \frac{B}{2\sqrt{C}}\ln\left[\frac{\psi[r_i] + r_i\sqrt{C} + \frac{B}{2\sqrt{C}}}{\psi[r_b] + r_b\sqrt{C} + \frac{B}{2\sqrt{C}}}\right] + \sqrt{A}\ln\left[\frac{\frac{\psi[r_i] + \sqrt{A}}{r_i} + \frac{B}{2\sqrt{A}}}{\frac{\psi[r_b] + \sqrt{A}}{r_b} + \frac{B}{2\sqrt{A}}}\right] \tag{2.29}$$

where

$$\psi[x] = \sqrt{Cx^2 + Bx + A} \tag{2.30}$$

$$A = \left(r_i f_{ct} + \frac{nE_c D_{\max}}{2\pi k}\right)^2 \tag{2.31}$$

$$B = \frac{f_{ct} D_{\max}}{k}\left[\frac{2r_i f_{ct}}{w_c} - \frac{nE_c}{\pi}\left(\frac{D_{\max}}{kw_c} - 2\right)\right] \tag{2.32}$$

$$C = \left(\frac{f_{ct} D_{\max}}{kw_c}\right)^2 \tag{2.33}$$

and r_i is the distance of the crack penetration into the concrete cover, measured from rebar centre to the crack tip.

2.3.5 Noghabai's model (1995)

In this model, the softening relation in the cracked region is taken as:

$$\frac{\sigma_t}{f_t'} = 1 - \frac{w}{w_c} \tag{2.34}$$

The cracked region is limited to $r_b \leq r \leq r_i$. The constant tangential displacement is estimated from $u_t = 2\pi\,\varepsilon_{ct}\,r_i = nw + 2\pi\,\varepsilon_t\,r$ (see Fig. 2.12).

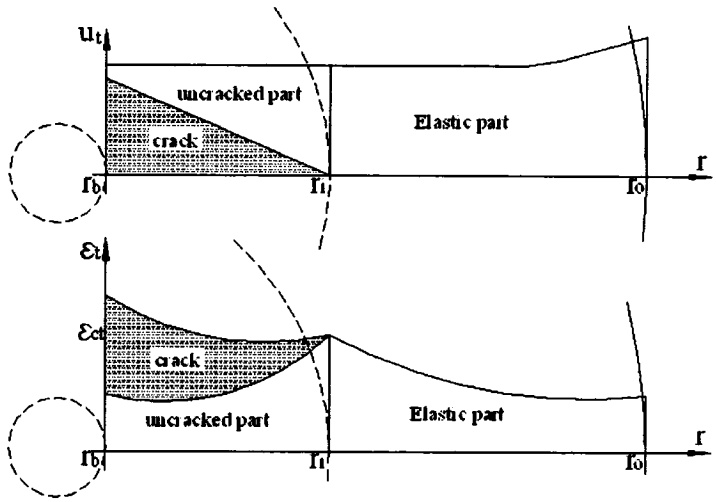

Fig. 2.12: Strain compatibility in concrete softening region (Noghabai, 1995)

The strain in the uncracked part remains constant as $\varepsilon_t(r) = \varepsilon_{ct}$ and the crack width is given by:

$$nw(r) = 2\pi[\varepsilon_{ct} r_i - \frac{\sigma_t}{E_c} r] \tag{2.35}$$

where n is the number of cracks. By introducing the maximum crack width as $w_c = 2G_f / f_t'$ and the material characteristic length $l_p = E_c G_f / f_t'^2$, the internal bar pressure p_b and the critical crack location r_i in the concrete hollow ring are related as follows:

$$\frac{p_b}{f_t'} = \frac{r_i}{r_b}\left(\frac{r_0^2 - r_i^2}{r^2_0 + r^2_i}\right) + \frac{nl_p - \pi r_i}{\pi r_b} \ln \frac{nl_p - \pi r_b}{nl_p - \pi r_i} \tag{2.36}$$

By ignoring the term $\frac{nl_p - \pi r_i}{\pi r_b} \ln \frac{nl_p - \pi r_b}{nl_p - \pi r_i}$, differentiating p_b with respect to r_i, and setting the simplified equation to zero, an optimum depth r_i, which gives the cracking penetration depth, is calculated at the location where the bar pressure reaches the maximum value.

2.3.6 Pantazopoulou and Papoulia's model (2001)

This model departs from the previous ones in that anisotropic behaviour is assumed. The state of stress is formulated as:

$$E_r\varepsilon_r=\sigma_r - \nu_{r\theta}\sigma_\theta-\nu_{rz}\sigma_z$$

$$E_\theta\varepsilon_\theta=\sigma_\theta - \nu_{\theta r}\sigma_r-\nu_{\theta z}\sigma_z$$

$$E_z\varepsilon_z=\sigma_z - \nu_{zr}\sigma_r-\nu_{z\theta}\sigma_\theta \quad (2.37)$$

where E_r, E_θ, and E_z are the moduli along the radial, tangential, and longitudinal directions, respectively, ε_r, σ_r, ε_θ, σ_θ, ε_z, and σ_z are the strains and stresses along the same direction, and $\nu_{r\theta}$ is the Poission's ratio on the tangential direction due to radial deformation. Likewise, $\nu_{\theta r}$, $\nu_{\theta z}$, $\nu_{z\theta}$, ν_{rz}, and ν_{zr} correspond to the different Posson's ratios along one direction due to deformations on the perpendicular direction.

At time t, given the radius of the rust front $R_r(t)$, the radial displacements are calculated from:

$$[K][u_r]=[B] \quad (2.38)$$

where $[u_r]$ is the array of unknown radial displacements, $[u_r]^T = [u_{r,1}\ u_{r,2}\ldots\ u_{r,N}]$, and matrices $[K]$ and $[B]$ are given by:

$$[B]_{Nx1}{}^T=[(R_r-R_b)(\frac{1}{h^2}-\frac{1}{2r_1h})\,0\,0\ldots 0] \quad (2.39)$$

$$[K_{NxN}]=\begin{bmatrix} \left(\frac{2}{h^2}+\frac{1}{r_1^2}\frac{E_{\theta,1}}{E_{r,1}}\right) & -\left(\frac{1}{h^2}+\frac{1}{2r_1h}\right) & 0 & \ldots & 0 & 0 & \ldots \\ -\left(\frac{1}{h^2}-\frac{1}{2r_2h}\right) & \left(\frac{2}{h^2}+\frac{1}{r_2^2}\frac{E_{\theta 2}}{E_{r2}}\right) & -\left(\frac{1}{h^2}+\frac{1}{2r_2h}\right) & \ldots & 0 & 0 & \ldots \\ \ldots & \ldots & \ldots & \ldots & \ldots & \ldots & \ldots \\ 0 & 0 & 0 & \ldots & -\left(\frac{1}{h^2}-\frac{1}{2r_{N-1}h}\right) & \left(\frac{2}{h^2}+\frac{1}{r^2_{N-1}}\frac{E_{g,N-1}}{E_{r,N-1}}\right) & \ldots \\ 0 & 0 & 0 & \ldots & 0 & -\frac{2}{h^2} & \ldots \end{bmatrix} \quad (2.40)$$

where $u_{r,i}$ is the displacement of node i in the radial direction, and h is the distance between two adjacent nodes along the radial direction. The moduli $E_{\theta,i}$ and $E_{r,1}$ are variables, depending on the corresponding strains at the points along the radial grid (denoted by subscript i according to the preceding equations). Once the values of $u_{r,i}$ and the

corresponding stresses are computed at time t, the model is advanced to the next time step. The solved values of $u_{r,i}$, $E_{\theta,i}$, and $E_{r,i}$ can be used as the new boundary conditions for next step. This procedure is carried out until the final solutions are obtained.

2.3.7 Summary of models

All of the previous models are summarized in the diagram illustrated in Fig. 2.13, which describes the relationship between the ratio of stress versus maximum tensile capacity σ_t/f_t' and that of crack opening width to maximum crack width w/w_c.

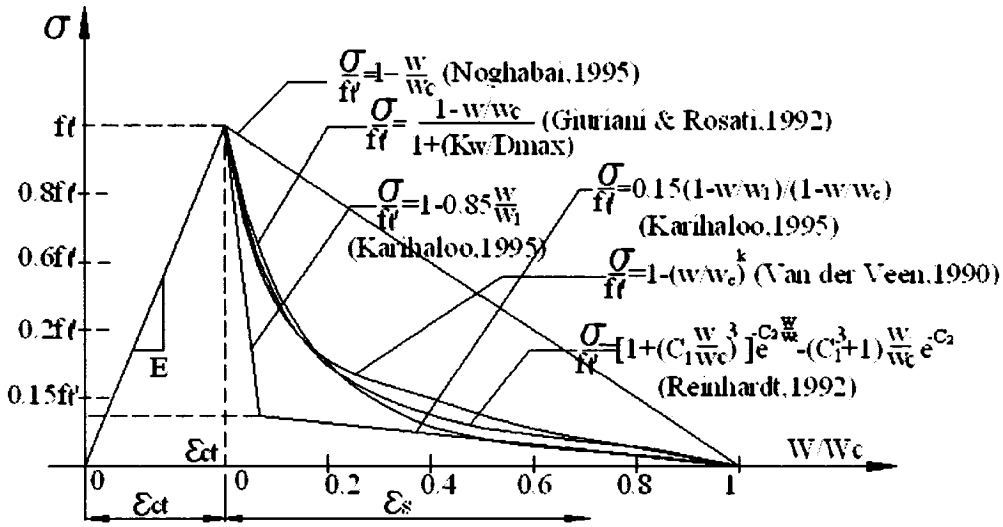

Fig. 2.13: Summary of stress- strain relations in the softening region

Chapter 3. Analytical Model

3.1. Introduction

Corrosion-induced damage in reinforced concrete structures is manifested by cracking, spalling, and delamination of the concrete cover. The volume of corrosion products is greater than the original steel due to their lower density. This increase in volume induces tangential tensile stresses and radial compressive stresses in the concrete surrounding the rebars. Only the tangential tensile stresses govern the concrete cover resistance. Once these tensile stresses exceed the concrete tensile capacity, cracking, spalling, and/or delamination of the concrete cover can take place.

A quantification of the damage caused by corroded reinforcing bars requires an accurate description of the relationship between the stresses and strains in the surrounding concrete. To do that, the volume expansion generated by the accumulation of corrosion products can be simulated by applying a uniform radial pressure on the interface between the steel bar and the concrete. To obtain the solution of the state of stress and strain in the concrete surrounding the reinforcing steel bars, a concrete ring model treated as a thick-wall cylinder subjected to an internal pressure is used in this thesis (refer to Fig. 2.4). The approach adopted here follows the same methodology proposed by others to analyze the state of stress in concrete due to bond forces (Tepfers, 1979; Van der Veen, 1990; Reinhardt, 1992; Rosati and Schumm, 1992; Noghabai, 1995).

The process predicting corrosion-induced cracking in concrete can be summarized into two steps. First, the relationship between the consumed bar mass and the induced pressure acting on the interface of the concrete/steel bar needs to be established. This has been done in chapter 2 (for details, refer to section 2.2). Second, the relationship between the corrosion-induced pressure and the state of stress and strain in the concrete cover is

formulated.

This chapter proposes an analytical model that relates the corrosion-induced pressure and the state of stress and strain in the surrounding concrete. This analytical model accounts only for cracking due to corrosion. In this formulation, it is assumed that concrete is an isotropic and homogeneous material.

3.2. Concrete ring model

Since the region of interest when modelling corrosion-induced cracking is that of the concrete surrounding the reinforcing bars, the concrete cover can thus be idealized as a hollow cylinder subjected to an internal expanding pressure acting on the contact surface between the rebar and the concrete. This expanding pressure is due to corrosion products build-up around the reinforcing steel bar. The thickness of this cylinder is given by the concrete cover depth (see Fig. 3.1). This distance represents the shortest path for a crack to propagate until it reaches a stress-free surface.

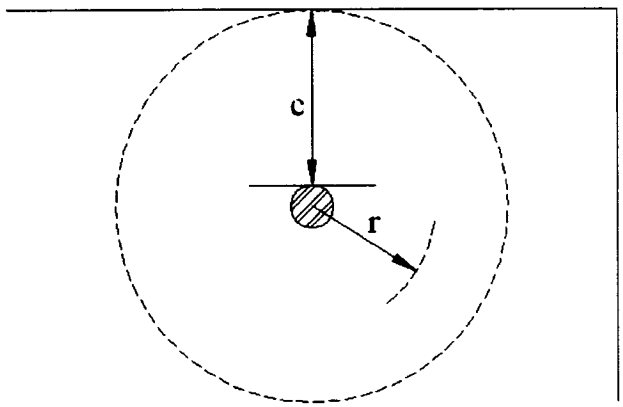

Fig. 3.1: Concrete ring model

Because the surrounding concrete restricts the movement of the expanding corroded bar, compressive stresses in the radial direction and tensile stresses in tangential direction are induced in the surrounding concrete. Concrete is a strong material in compression but weak in tension. As the corrosion-induced pressure increases, the accumulated tensile stresses in the surrounding concrete become larger and larger until they reach the concrete tensile

capacity. As soon as they reach this tensile capacity, the concrete cover begins to crack. This initiation of cracking does not correspond to the maximum tensile capacity of the concrete cover. However, once the crack propagates to a maximum critical depth, it will propagate through the remaining uncracked concrete until a stress-free surface is reached. At this point, the concrete ring's tensile capacity has been fully reached.

In this thesis, the longitudinal dimension of the concrete member is assumed infinitely long, and the strain along this direction is neglected, i.e., plane-strain conditions are applied. Thus, a 3-D analysis can be simply converted to a 2-D one. In modelling the cracking process of a concrete ring subjected to internal pressure, three distinct regions can be differentiated: (1) the outer uncracked elastic zone; (2) the fictitious cracked softening intermediate zone; and, (3) the inner cracked zone (see Fig. 3.2).

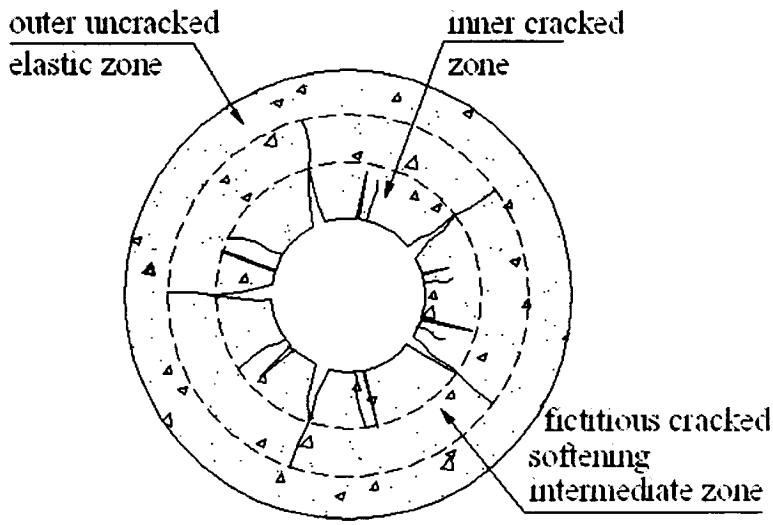

Fig. 3.2: Three regions of the concrete ring

The states of stresses and strains in these three regions are distinct and will be explained in the next sections.

3.2.1. Elastic region

The stress-strain relations for a thick-wall cylinder made of an isotropic and linearly elastic material are given by:

$$\varepsilon_r = \frac{1}{E}(\sigma_r - \upsilon\sigma_t - \upsilon\sigma_z) \quad \text{and} \quad \varepsilon_t = \frac{1}{E}(\sigma_t - \upsilon\sigma_r - \upsilon\sigma_z) \tag{3.1}$$

where

ε_r = strain in the radial direction

ε_t = strain in the tangential direction

v = Poission's ratio

σ_r = stress in the radial direction

σ_t = stress in the tangential direction

σ_z = stress in the longitudinal direction

E = modulus of elasticity

Based on plane-strain conditions (ε_z =0), solving for stresses σ_r and σ_t results in:

$$\sigma_r = \frac{E}{(1+\upsilon)(1-2\upsilon)}\left[(1-\upsilon)\varepsilon_r + \upsilon\varepsilon_t\right]$$
$$\sigma_t = \frac{E}{(1+\upsilon)(1-2\upsilon)}\left[\upsilon\varepsilon_r + (1-\upsilon)\varepsilon_t\right] \tag{3.2}$$

In the hollow ring, the elongations along the radial and tangential directions are given by:

$$\varepsilon_r = \frac{\partial u}{\partial r} \quad \text{and} \quad \varepsilon_t = \frac{u}{r} \tag{3.3}$$

where u is the radial displacement at a distance r in the thick-walled cylinder.

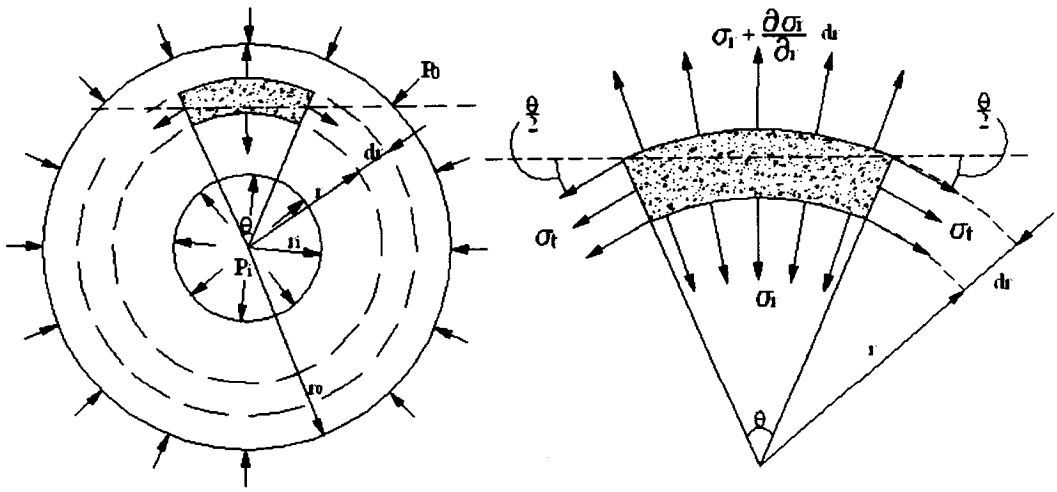

Fig. 3.3 Thick-wall cylinder subjected to internal and external pressures

Establishing force equilibrium in an isolated small piece as illustrated in Fig. 3.3 leads

to:

$$\sigma_r + r\frac{\partial \sigma_r}{\partial r} - \sigma_t = 0 \tag{3.4}$$

Substituting Eqs. 3.2 and 3.3 into Eq. 3.4 results in the following differential equation:

$$\frac{\partial^2 u}{\partial r^2} + \frac{1}{r}\frac{\partial u}{\partial r} - \frac{u}{r^2} = 0 \tag{3.5}$$

The general solution for Eq. 3.5 is: $u = Ar + \frac{B}{r}$, where A and B are constants depending on the boundary conditions. By combining this general solution, Eqs. 3.2, and 3.3, and applying the boundary conditions, the stresses can be calculated from:

$$\sigma_r = \frac{r_i^2 p_i - r_0^2 p_0}{r_0^2 - r_i^2} - \frac{r_0^2 r_i^2 (p_i - p_0)}{r^2 (r_0^2 - r_i^2)} \tag{3.6}$$

$$\sigma_t = \frac{r_i^2 p_i - r_0^2 p_0}{r_0^2 - r_i^2} + \frac{r_0^2 r_i^2 (p_i - p_0)}{r^2 (r_0^2 - r_i^2)} \tag{3.7}$$

$$u_r = \frac{1-\upsilon}{E_c}\frac{r_i^2 p_i - r_0^2 p_0}{r_0^2 - r_i^2} r + \frac{1+\upsilon}{E_c}\frac{r_i^2 r_0^2 (p_i - p_0)}{r_0^2 - r_i^2}\frac{1}{r} \tag{3.8}$$

where

p_0 = pressure acting on the outer free surface of the hollow ring

p_i = pressure acting on the inner surface of the hollow ring

r_0 = outer radius of hollow ring measured from the rebar centre

r_i = inner radius of hollow ring measured from the rebar centre to the inner surface

r = radius of the selected point where stresses are calculated, $r_i \le r \le r_0$

If no outer pressure p_0 is acting on the thick-wall cylinder, Eq.3.7 can be simplified:

$$\sigma_t = p_i \frac{r_i^2 (r^2 + r_0^2)}{r^2 (r_0^2 - r_i^2)} \tag{3.9}$$

Equation 3.9 can be rewritten as:

$$p_i = \sigma_t \frac{r^2 (r_0^2 - r_i^2)}{r_i^2 (r^2 + r_o^2)} \tag{3.10}$$

Equation 3.10 gives the relationship between the corrosion-induced pressure p_i and the

corresponding tangential tensile stress σ_t in the surrounding concrete. The maximum tangential tensile stress occurs at the inner surface ($r=r_i$). As the pressure p_i increases, σ_t increases accordingly until it reaches the concrete tensile strength f_t'. Once the concrete tensile strength is reached, a crack starts to initiate at the steel bar/concrete interface. Therefore the critical bar expansion pressure, at which the inner concrete starts to crack, is given by:

$$p_i = f_t' \frac{r_0^2 - r_i^2}{r_i^2 + r_o^2} \tag{3.11}$$

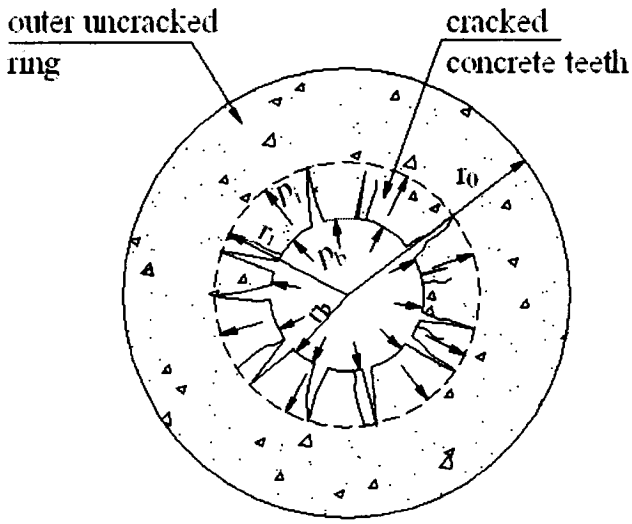

Fig. 3.4: Concrete ring subjected to an attenuated pressure p_i

As the crack propagates through the concrete cover, the uncracked outer ring (see Fig. 3.4) can be treated as a thick-wall cylinder of thickness r_0-r_i and subjected to an internal pressure p_i. This pressure p_i is the attenuated build-up pressure transferred through the concrete teeth between cracks ($p_i=p_b r_b/r_i$). When the expanding pressure p_b reaches a maximum critical value, corresponding to the concrete tensile capacity f_t', cracks initiate at the surface located at a distance of r_b measured from the rebar centre. As more cracks develop, the accumulated bar pressure p_b due to the rust is released. At this moment a force balance between the reinforcing bar pressure p_b and the concrete resistance provided by the uncracked concrete cover is built up. However, with the continuous generation of rust along

the bar surface, this force balance is broken and the released bar pressure gradually builds up to f_t' again. As a result, more cracks originate and a new force balance between the bar pressure and the concrete resistance is set up again. This process of concrete cracking is repetitive rather than continuous. Finally, when a crack approaches a certain depth, the tangential tensile stress in the uncracked concrete reaches the concrete maximum tensile strength, and beyond that depth, the cracking process is no longer iterative. The remaining uncracked concrete cannot provide enough resistance to balance the built-up bar pressure. At this point, the crack suddenly penetrates the remaining concrete cover. Hence, Eq. 3.11 should be adjusted as:

$$p_b = f_t' \frac{r_i}{r_b} \frac{r_0^2 - r_i^2}{r_i^2 + r_o^2} \tag{3.12}$$

In Eq. 3.12, r_b and p_b are unknown variables. By differentiating p_b with respect to r_b and setting the result to zero, the optimum value of r_b for which the tensile capacity of the entire concrete cylinder is reached is given by:

$$r_b = 0.4858 r_0 \tag{3.13}$$

If the concrete cover depth is assumed to be c, then $r_0 = r_b + c$. Substituting them back into Eq. 3.13 results in:

$$c = 1.0576\, r_b \tag{3.14}$$

When $r_b = 0.4858\, r_0$, the corrosion-induced pressure p_b reaches the critical value—P_b^{max}, at which the surrounding concrete cover is completely cracked. Hence,

$$p_b^{max} = 0.3 f_t' r_0/r_b = 0.3 f_t' (r_b+c)/r_b \tag{3.15}$$

3.2.2. Softening region

Observation from laboratory experiments (Van der Veen, 1990; Reinhardt, 1992; Rosati and Schumm, 1992; Noghabai, 1995) have shown that the relationship of bar expansion pressure p_b and crack front r_i does not exactly follow Eq. 3.12. In fact, experimental values of p_b are consistently higher than those obtained from Eq. 3.12. This suggests that there must be an

intermediate transition layer between the uncracked and cracked concrete zones affecting the relationship between the bar pressure and crack depth. Researchers have named this intermediate transition layer as the fictitious cracking layer or softening layer (Karihaloo, 1995), and they have proposed various constitutive laws relating the stresses and strains in this layer (see Fig. 2.13). These various relationships are linear, bi-linear, exponential, and polynomial functions. Reinhardt's function is constituted of multiple algebraic terms (Reinhardt, 1992); the ratio of tangential stress to concrete tensile strength is related to the ratio of crack opening displacement to maximum crack width. Van Der Veen's law is easily embodied by a smooth concave curve starting from the maximum tensile strength and ending in a zero value (Van Der Veen 1990). Rosati and Schumm's model largely depends on the slope of the curve and maximum size of the aggregate in the concrete cylinder ring (Rosati and Schumm, 1992). Noghabai has used a linear relation to describe the concrete behaviour in the softening zone (Noghabai, 1995). Pantazopoulou and Papoulia used a bi-linear function to describe the stress state in the concrete softening area. Three important points in this bi-linear function are determined by the maximum aggregate size, the concrete tensile strength, and the crack-band width (Pantazopoulou and Papoulia, 2001).

In this work, for the sake of simplicity and in order to get a general solution, a linear relationship between the stress and crack opening width has been used to describe the concrete behaviour in the softening region, i.e.,

$$\sigma_t(w) = f_t'(1 - \frac{w}{w_c}) \tag{3.16}$$

where

σ_t = tensile stress in the softening region

f_t' = concrete tensile strength

w = fictitious crack width where tension is calculated

w_c = maximum fictitious crack width

Equation 3.16 ignores the effects of both Poisson's ratio and the perpendicular compressive

stress (i.e., reduction of tensile strength due to a normal compressive stress is neglected.)

The concrete softening region includes two parts: one that is uncracked, and the other that is fictitiously cracked. In the uncracked part, the maximum strain remains always the same and equal to ε_{ct} (see Fig. 3.5).

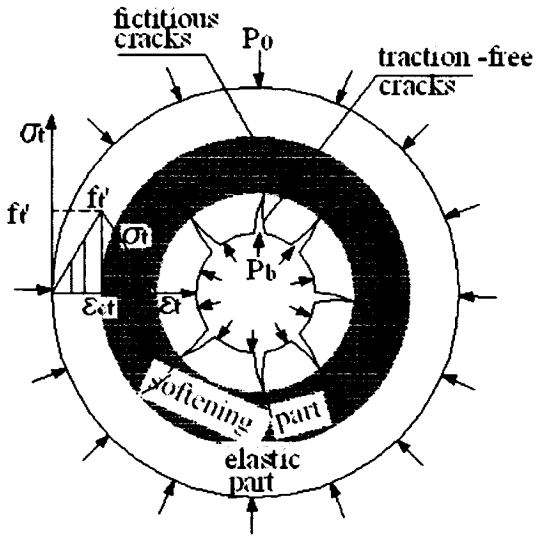

Fig. 3.5: Strains in elastic and softening regions

Fictitious cracks are not real cracks. The bond forces in these so-called fictitious cracks are very strong. With the increase of tensile strength along the radial direction, the bond forces gradually become weak; however, they still keep concrete uncracked and the strain in this uncracked region is always equal to the maximum critical value of ε_{ct}—i.e, the maximum strain capacity of concrete. In other words, part of the tensile stresses in the fictitious zone is used in keeping the uncracked elastic region in stable equilibrium; the remainder of the tensile stresses in the fictitious zone is used to overcome the increase of the fictitious crack widths. Thus, the strain remains constant and always equal to ε_{ct}.

$$\varepsilon_t = \varepsilon_{ct} \tag{3.17}$$

where ε_t is the tangential strain in the uncracked region of the softening area. Equation 3.17 differs from Noghabai's assumption in that $\varepsilon_t \neq \varepsilon_{ct}$ (Noghabai, 1995). As a rigid material,

only translational movement (no rotation) is assumed to take place when cracking occurs. Therefore, the relationship among w_c (maximum opening width of the fictitious cracks), w (opening width of the fictitious cracks), ε_t, and ε_{ct} can be derived based on Fig. 3.6, i.e.,

$$u_t = 2\pi r_i \varepsilon_{ct} = nw + 2 r \pi \varepsilon_t \tag{3.18}$$

where

u_t = increment of the perimeter of concrete ring in tangential direction at r_i

n = number of cracks

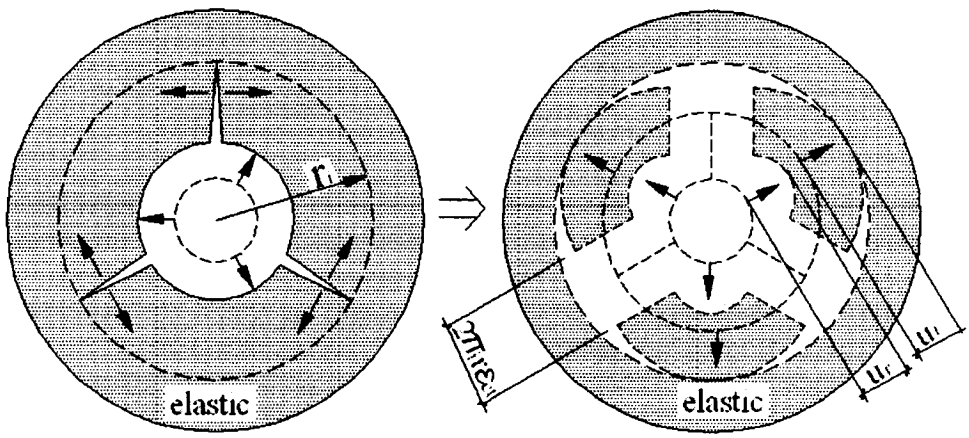

Fig. 3.6: Compatibility in the softening region (adapted from Van der Veen, 1990)

The process of cracking in a concrete ring follows five steps: (1), the increase of pressure due to corrosion products accumulation on the rebar surface; (2), the appearance of micro-cracks; (3), the propagation of micro-cracks and material softening; (4), the decrease in the size of the elastic zone and increase in the size of the traction-free zone; and (5), the penetration of cracks through the entire concrete cover. Therefore, the analytical model proposed should reflect all aspects in the cracking process. For convenience, the concrete cover is modelled into elastic and softening regions, as illustrated in Fig. 3.7.

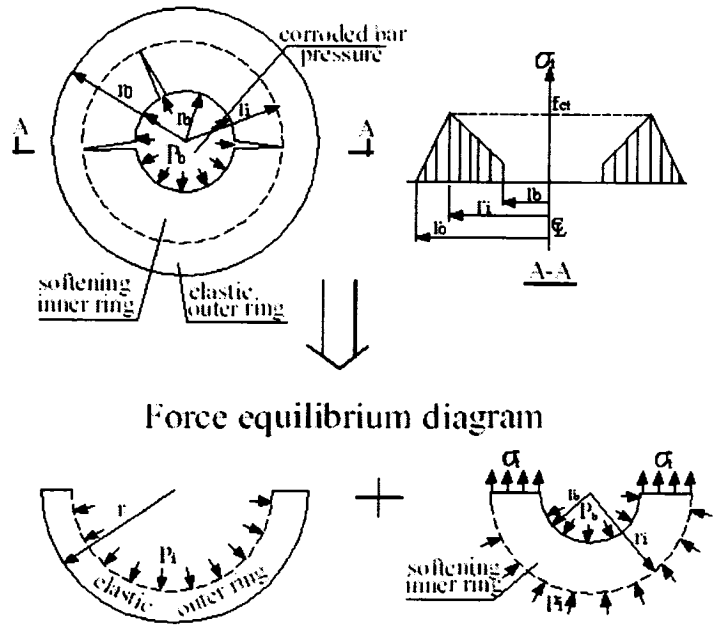

Fig. 3.7: Modelling cracking of the concrete cover

As shown in Fig 3.7, establishing force equilibrium of the inner half ring leads to:

$$2p_b r_b = 2 p_i r_i + 2 \int_{r_b}^{r_i} \sigma_t dr \tag{3.19}$$

By substituting Eq. 3.17 into Eq. 3.18, the following relation results:

$$nw = 2\pi\varepsilon_{ct} (r_i - r) \tag{3.20}$$

Substituting Eq. 3.20 back into Eq. 3.16 results in:

$$\sigma_t(w) = f_t'[1 - \frac{2\pi\varepsilon_{ct}(r_i - r)}{nw_c}] \tag{3.21}$$

By substituting Eq. 3.21 into Eq. 3.19, the following expression is obtained:

$$p_b r_b = p_i r_i + \int_{r_b}^{r_i} f_t'[1 - \frac{2\pi\varepsilon_{ct}(r_i - r)}{nw_c}]dr \tag{3.22}$$

The first term p_i in Eq. 3.22 is obtained from Eq. 3.11. By integrating the second term with respect to dr from r_b to r_i and combining with Eq. 3.11, Eq. 3.22 becomes:

$$\frac{p_b}{f_t'} = \frac{r_i}{r_b}\frac{r_0^2 - r_i^2}{r_i^2 + r_o^2} + \frac{(r_i - r_b)(nw_c + \pi\varepsilon_{ct} r_b - \pi\varepsilon_{ct} r_i)}{nr_b w_c} \tag{3.23}$$

where w_c is the cracking tip opening width, taken as $G_F/0.4969f_t'$(Karihaloo, 1995), which is approximately equal to $2G_F/f_t'$, and G_F is he fracture energy, calculated from $G_F = \int_0^{w_c} \sigma(w)dw$, which is equal to the area under the tension softening curve. The fracture energy G_F can be determined by a three point bending test where the beam has a central edge notch (see Fig. 3.8).

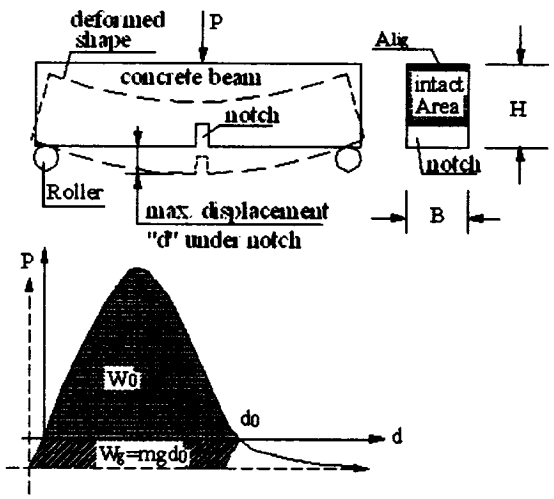

$G_F = (W_0+W_g d_0)/A_{lig}$

W_0 = area under P-d_0 curve up to d_0

W_g = sum of the self-weight of the specimen and twice the self-weight of any fixtures resting on it

d_0 = displacement as P returns to zero

A_{lig} = original uncracked concrete cross sectional area

Fig. 3.8: Experimental approach for determining G_F

Equation 3.23 is simplified by introducing another parameter l_p, known as the characteristic length (Noghabai, 1995), which is calculated from $l_p \approx E_c G_F / f_t'^2$. By applying the concept of characteristic length l_p, a new expression for w_c is obtained:

$$w_c = 2\, l_p \varepsilon_{ct} \tag{3.24}$$

By substituting Eq. 3.24 into Eq. 3.23, the following relation results:

$$\frac{p_b}{f_t'} = \frac{r_i}{r_b}\frac{r_0^2 - r_i^2}{r_o^2 + r_i^2} + \frac{(r_i - r_b)(2nl_p + \pi r_b - \pi r_i)}{2nr_b l_p} \tag{3.25}$$

Equation 3.25 can be rewritten by using $d/2=r_b$, $d/2+c = r_0$, and $e=r_i$:

$$\frac{p_b}{f_t'} = \frac{2e}{d}\frac{(c+d/2)^2 - e^2}{(c+d/2)^2 + e^2} + \frac{(2e-d)(4nl_p + \pi d - 2\pi e)}{4ndl_p} \tag{3.26}$$

where

d = reinforcing bar diameter, $r_b = d/2$

c = concrete cover thickness, $r_0 = c+d/2$

e = crack front surface distance measured from the rebar center

Equation 3.26 relates the corrosion-induced pressure p_b to the concrete cover c and crack front distance e. This relationship is illustrated in Fig. 3.9 by assuming d = 15 mm, c = 40 mm, n = 1, and l_p = 111 mm.

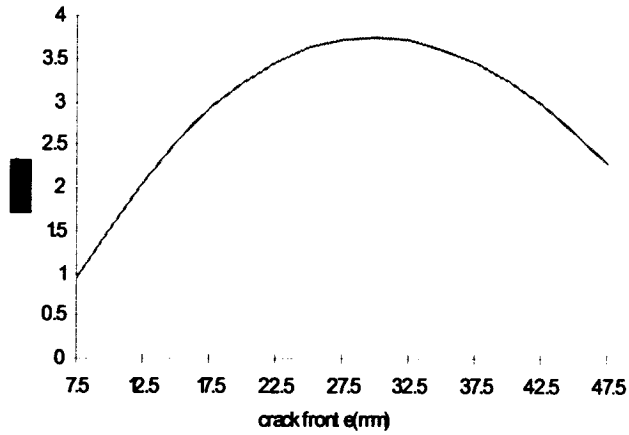

Fig. 3.9: Illustration of p_b/f_t' versus crack front e according to Eq. 3.26

Equation 3.26 clearly shows that each crack front corresponds to a unique pressure. Before the crack front e reaches a critical value, pressure p_b is approximately directly proportional to the depth of crack. Beyond that critical point, the pressure p_b drops down with the increase of crack front e. Alternatively, the curve of bar pressure versus crack depth r_i has a parabola-like top point, which represents the maximum or minimum of p_b here. Differentiating p_b/f_t' with respect to r_i and setting the result to zero gives a polynomial function in r_i. This function can be solved for an optimum value of r_i, which corresponds to the maximum or minimum value of $p_{b\max}$:

$$r_i^5 - r_b r_i^4 + 2r_0^2 r_i^3 + \left[\left(2nl_p r_0^2/\pi\right) - 2r_b r_0^2\right] r_i^2 + r_0^4 r_i - \left(2nl_p r_0^4/\pi\right) - r_b r_0^4 = 0 \qquad (3.27)$$

Since Eq. 3.27 is a fifth-order function, it cannot be solved directly. Solution to Eq. 3.27 is obtained by means of an iterative computation until the difference between two adjacent results is less than 10%.

From Eqs. 3.21 and 3. 24, the stress in the softening region can be calculated from:

$$\sigma_t(r) = f_t' \frac{nl_p + \pi r - \pi r_i}{nl_p} \tag{3.28}$$

where r_i is the depth of the selected point measured from the rebar centre. By rewriting Eq. 3.28 as:

$$r_i = \frac{nl_p}{\pi} + r - \frac{nl_p \sigma_t}{f_t' \pi} \tag{3.29}$$

By substituting Eq. 3.29 into Eq. 3.25, the following relationship between the pressure p_b, the tangential tensile stress σ_t, and distance r measured from the bar centre results:

$$\begin{aligned}
&\frac{p_b}{f_t'} \\
&= \frac{\left(nl_p f_t' + \pi f_t' r - nl_p \sigma_t\right)\left(r_0^2 \pi^2 f_t'^2 - n^2 l_p^2 \sigma_t^2 + 2n^2 l_p^2 f_t' \sigma_t + 2nl_p \pi f_t' \sigma_t r - n^2 l_p^2 f_t'^2 - 2n\pi l_p f_t'^2 r - \pi^2 f_t'^2 r^2\right)}{r_b \pi f_t' \left(r_0^2 \pi^2 f_t'^2 + n^2 l_p^2 f_t'^2 + r^2 \pi^2 f_t'^2 + 2nl_p \pi f_t'^2 r - 2n^2 l_p^2 f_t' \sigma_t - 2nl_p \pi f_t' r \sigma_t + n^2 l_p^2 \sigma_t^2\right)} \\
&+ \frac{\left(nl_p f_t' + \pi f_t' r - nl_p \sigma_t - \pi f_t' r_b\right)\left(nf_t' l_p + \pi f_t' r_b - \pi f_t' r + nl_p \sigma_t\right)}{2n\pi r_b l_p f_t'^2}
\end{aligned} \tag{3.30}$$

At the maximum crack depth, the tangential tensile stress is equal to zero, the aggregate interlock and bridge effects are lost thoroughly, and a sudden splitting from the current location to the closest free surface of the concrete cover occurs. By setting σ_t to zero, Eq. 3.30 can be rewritten as:

$$\begin{aligned}
\frac{p_b}{f_t'} &= \frac{\left(nl_p + \pi r\right)\left(r_0^2 \pi^2 - n^2 l_p^2 - 2n\pi l_p r - \pi^2 r^2\right)}{r_b \pi \left(r_0^2 \pi^2 + n^2 l_p^2 + r^2 \pi^2 + 2nl_p \pi r\right)} \\
&+ \frac{\left(nl_p + \pi r - \pi r_b\right)\left(nl_p + \pi r_b - \pi r\right)}{2n\pi r_b l_p}
\end{aligned} \tag{3.31}$$

where $r_b \le r \le r_i \le r_0$.

Equation 3.31 is a function of p_b in terms of the real crack tip location r, because the tangential tensile stress is equal to zero here. Setting the derivative expression of Eq. 3.31 with respect to r to zero yields the maximum bar pressure p_{bmax} and the real critical crack opening tip location r. Once this depth is exceeded, cracks penetrate through the entire

concrete cover.

3.3. Effect of spiral confinement reinforcement

Equation 3.25 assumes that there is no external pressure acting on the concrete thick-wall cylinder (i.e., $p_0 = 0$), and therefore any confinement provided by stirrups or ties is not accounted for. Equation 3.25 can be rewritten as follows:

$$p_b = \frac{r_i}{r_b} p_i + \frac{f_t'(r_i - r_b)(2nl_p + \pi r_b - \pi r_i)}{2nr_b l_p} \tag{3.32}$$

where p_i is given by Eq. 3.11.

The pressure p_i can be considered as a positive effect of the outer elastic ring acting on the inner ring. Further confinement effects can be taken into account by introducing spiral reinforcement into the model. Spiral reinforcement can either be located in the uncracked region or in the cracked one.

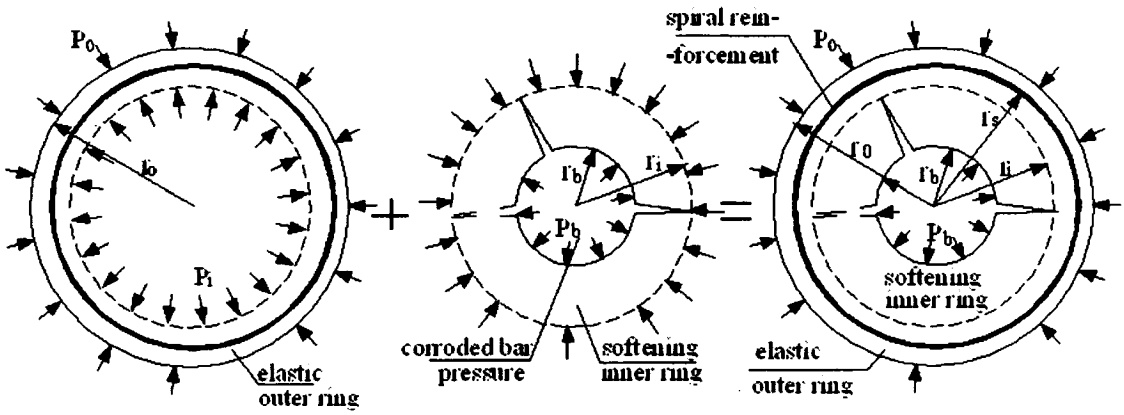

Fig. 3.10: Confinement in the uncracked region of the concrete ring model

If the spiral reinforcement is located in the uncracked zone, (Fig. 3.10), then the pressure p_i is the combination of the pressure acting on the outer uncracked region p_i^e and the pressure provided by the spiral confinement p_i^s, which is determined by the deformation of the spiral bar ε_s. By establishing equilibrium (see Fig. 3.11),

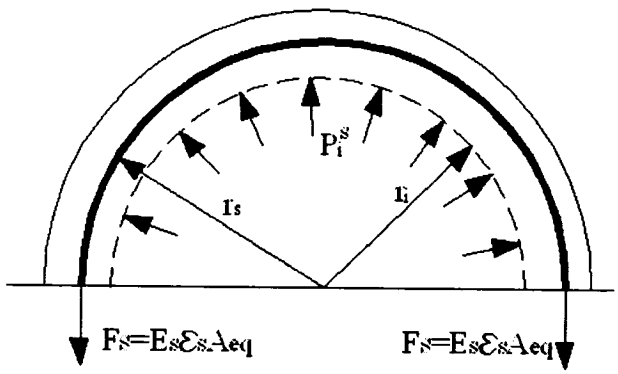

Fig. 3.11: Equilibrium in confined concrete

$$p_i^s = \frac{E_s \varepsilon_s A_{eq}}{r_i} \tag{3.33}$$

where A_{eq} is equal to the spiral steel area divided by the spiral pitch. Therefore, the resulting p_i combining the effects of the outer elastic part and the spiral confinement can be expressed as:

$$p_i = p_i^e + p_i^s = f_t' \frac{r_0^2 - r_i^2}{r_o^2 + r_i^2} + \frac{E_s \varepsilon_s A_{eq}}{r_i} \tag{3.34}$$

From Eq. 3.3, it is known that $\varepsilon_t = u/r$. Therefore, at the location of the confining reinforcement $r=r_s$, the strain of the spiral bar can be derived from Eq. 3.8, i.e.,

$$\varepsilon_s = \frac{u_s}{r_s} = \frac{1}{E_c\left(r_0^2 - r_i^2\right)}\left\{p_i r_i^2\left[(1-\upsilon)+(1+\upsilon)\frac{r_0^2}{r_s^2}\right] - p_0 r_0^2\left[(1-\upsilon)+(1+\upsilon)\frac{r_i^2}{r_s^2}\right]\right\} \tag{3.35a}$$

Neglecting Poisson's ratio υ yields:

$$\varepsilon_s = \frac{1}{E_c\left(r_0^2 - r_i^2\right)}\left[p_i r_i^2\left(1+\frac{r_0^2}{r_s^2}\right) - p_0 r_0^2\left(1+\frac{r_i^2}{r_s^2}\right)\right] \tag{3.35b}$$

At the location of $r=r_i$, Eq. 3.7 can be rewritten as:

$$\sigma_t = f_t' = \frac{1}{r_0^2 - r_i^2}\left[\left(r_i^2 + r_0^2\right)p_i^2 - 2p_0 r_0^2\right] \tag{3.36}$$

By combining Eqs. 3.34, 3.35b, and 3.36, the expressions for ε_s and p_i^s are obtained as follows:

$$\varepsilon_s = \frac{f_t' r_i^2}{E_c\left(r_0^2 + r_i^2\right)} \frac{2\left(r_0^2 + r_s^2\right)E_c r_i}{\left[2r_s^2 E_c r + E_s A_{eq}\left(r_s^2 - r_i^2\right)\right]} \tag{3.37}$$

$$p_i^s = \frac{E_s \varepsilon_s A_{eq}}{r_i} = \frac{2f_t' r_i^2\left(r_0^2 + r_s^2\right)}{\left(r_0^2 + r_s^2\right)\left(\frac{2r_i r_s^2 E_c}{E_s A_{eq}} + r_s^2 - r_i^2\right)} \tag{3.38}$$

By substituting Eq. 3.38 into Eq.3.34, the following expression for p_i results:

$$p_i = p_i^e + p_i^s = f_t' \frac{r_0^2 - r_i^2}{r_o^2 + r_i^2} + \frac{2 f_t' r_i^2 \left(r_0^2 + r_s^2\right)}{\left(r_0^2 + r_s^2\right)\left(\frac{2 r_i r_s^2 E_c}{E_s A_{eq}} + r_s^2 - r_i^2\right)} \tag{3.39}$$

Substituting the final expression of p_i back into Eq. 3.32 gives the new expression for the rebar pressure with confining reinforcement in the uncracked region of the concrete ring:

$$\frac{p_b}{f_t'} = \frac{r_i}{r_b}\frac{r_0^2 - r_i^2}{r_o^2 + r_i^2} + \frac{(r_i - r_b)(2nl_p + \pi r_b - \pi r_i)}{2nr_b l_p} + \frac{2r_i^3 (r_0^2 + r_s^2)}{r_b (r_0^2 + r_s^2)\left(\frac{2 r_i r_s^2 E_c}{E_s A_{eq}} + r_s^2 - r_i^2\right)} \tag{3.40}$$

By rewriting Eq. 3.40 using $r_b=d/2$, $r_0=d/2+c$, and $r_i=e$:

$$\frac{p_b}{f_t'} = \frac{2e}{d}\frac{(c+d/2)^2 - e^2}{(c+d/2)^2 + e^2} + \frac{(2e-d)(4nl_p + \pi d - 2\pi e)}{4ndl_p} + \frac{4e^3\left[\left(c+\frac{d}{2}\right)^2 + r_s^2\right]}{d\left[\left(c+\frac{d}{2}\right)^2 + r_s^2\right]\left(\frac{2 e r_s^2 E_c}{E_s A_{eq}} + r_s^2 - e^2\right)} \tag{3.41}$$

If the spiral reinforcement is located in the cracked region of the concrete ring model (see Fig. 3.12), the process to derive the expression for p_i is similar to the previous one. In this case, the strain of the spiral bar ε_s includes two parts: one is the normal elongation in the concrete teeth, the other is that taking place across cracks where the reinforcement carries all the tensile stresses, as shown in Fig. 3.13.

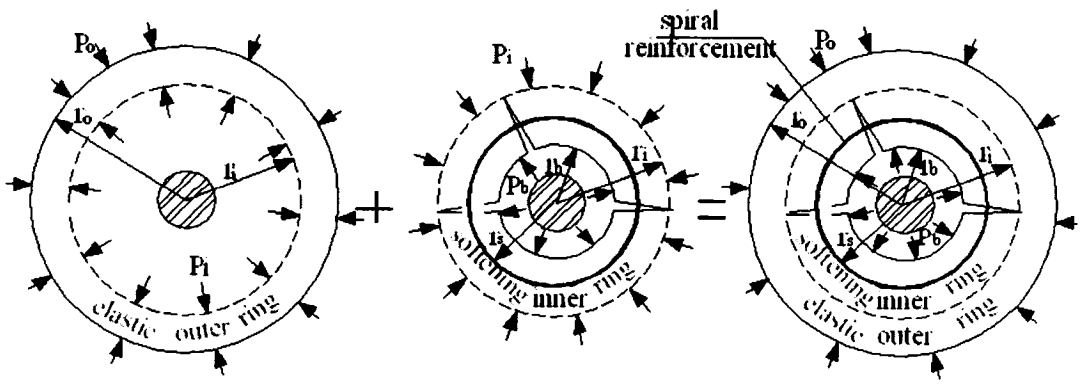

Fig. 3.12: Confinement in the cracked region of the concrete ring model

The spiral bar strain in the uncracked concrete is denoted as ε^e_s and the strain at the crack location is denoted as ε^c_s. The total bar elongation ε_s is the sum of both:

$$\varepsilon_s = \varepsilon^e_s + \varepsilon^c_s$$

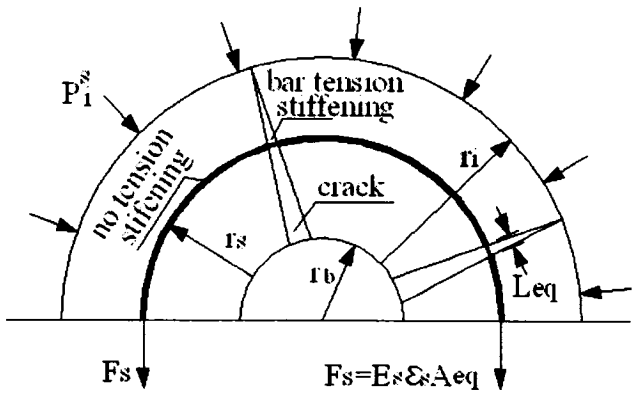

Fig. 3.13: Tensile stresses carried by the reinforcement at crack locations

According to Eq. 3.33, $E_s\varepsilon_s A_{eq} = r_i p^s_i$. Assuming perfect bond, the spiral bar elongation in the uncracked concrete ε^e_s is equal to ε_{ct}, therefore,

$$\varepsilon_s = \varepsilon_{ct} + \varepsilon^c_s = \frac{f_t'}{E_c} + \varepsilon^c_s \tag{3.42}$$

In order to obtain an expression for the strain ε^c_s, it is assumed that this strain only happens within the crack width w and is uniformly distributed within this length, therefore $\varepsilon^c_s = w/l_{eq}$. From Eq. 3.20 it is found that $w=2\pi f_t'(r_i - r)/(nE_c)$. Substituting the expression of ε^c_s back into Eq. 3.42 gives the expression of the spiral bar's strain as follows:

$$\varepsilon_s = \varepsilon_{ct} + \varepsilon^c_s = \frac{f_t'}{E_c}\left[1 + \frac{2\pi(r_i - r_s)}{nl_{eq}}\right] \tag{3.43}$$

where l_{eq} is the spiral bar's equivalent length only within which ε^c_s and the total crack width w occur, usually taken as $2\pi r_s/n$. By using the expression of ε_s in Eq. 3.43, the pressure provided by the confining reinforcement located in the softening region of the concrete ring model p^s_i is obtained from:

$$p_i^s = \frac{E_s \varepsilon_s A_{eq}}{r_i} = \frac{E_s f_t' A_{eq}}{E_c r_i}\left[1 + \frac{2\pi(r_i - r_s)}{n l_{eq}}\right] \tag{3.44}$$

The new expression for p_i is obtained by substituting Eq. 3.44 back into Eq. 3.34, i.e.,

$$p_i = p_i^e + p_i^s = f_t' \frac{r_0^2 - r_i^2}{r_o^2 + r_i^2} + \frac{E_s f_t' A_{eq}}{E_c r_i}\left[1 + \frac{2\pi(r_i - r_s)}{n l_{eq}}\right] \tag{3.45}$$

The final expression for the bar pressure with the spiral confinement located in the softening region of the ring model is obtained by substituting the new p_i in Eq. 3.45 back into Eq. 3.32, i.e.,

$$\frac{p_b}{f_t'} = \frac{r_i}{r_b}\frac{r_0^2 - r_i^2}{r_o^2 + r_i^2} + \frac{(r_i - r_b)(2nl_p + \pi r_b - \pi r_i)}{2nr_b l_p} + \frac{E_s f_t' A_{eq}}{E_c r_b}\left[1 + \frac{2\pi(r_i - r_s)}{n l_{eq}}\right] \tag{3.46}$$

By rewriting Eq. 3.46 using $r_b = d/2$, $r_0 = d/2 + c$, and $r_i = e$, the following results:

$$\frac{p_b}{f_t'} = \frac{2e}{d}\frac{(c + d/2)^2 - e^2}{(c + d/2)^2 + e^2} + \frac{(2e - d)(4nl_p + \pi d - 2\pi e)}{4ndl_p} + \frac{2E_s A_{eq} f_t'}{E_c d}\left[1 + \frac{2\pi(e - r_s)}{n l_{eq}}\right] \tag{3.47}$$

Equations 3.26, 3.41 and 3.47, which respectively express the required pressure to induce cracking when no confinement is provided, confinement is provided in the elastic region, and confinement is provided in the softening region, are plotted in Fig. 3.14 for comparison purposes. As observed from the figure, it is obvious that the critical corrosion-induced pressure p_b of a concrete cylinder with confinement in the cracked zone (softening region) is much higher than the one when no confinement at all is provided.

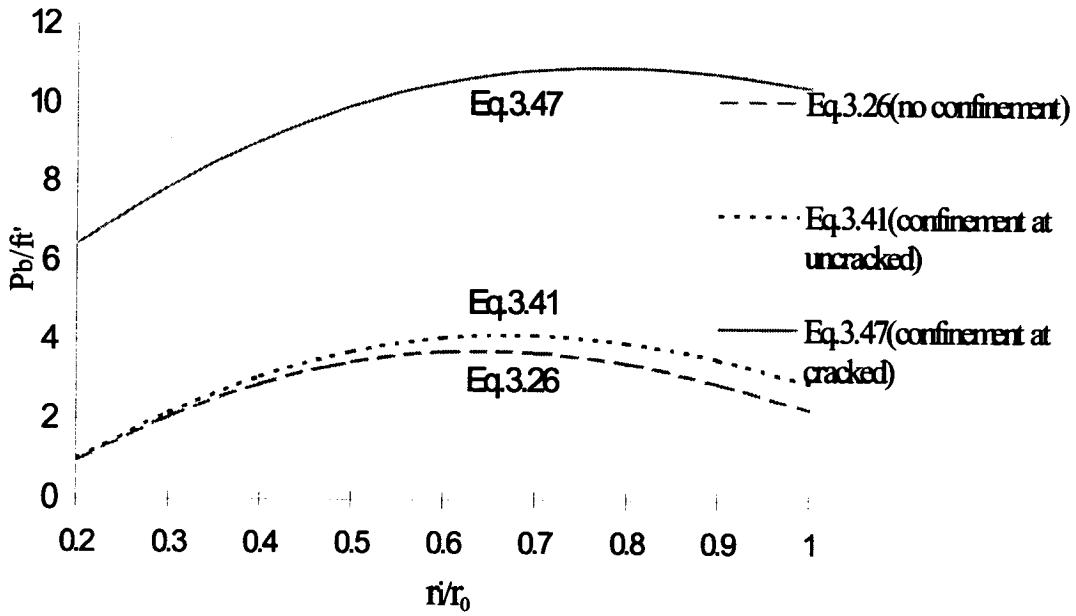

Fig. 3.14: Illustration of p_b/ft' versus crack front—*e*

3.4. Relation between corrosion build-up and induced pressure

As reinforcement corrosion progresses, the build-up produced by the accumulation of corrosion products on the rebar surface (denoted as Δd) induces the expanding pressure p_b, which acts on the interface between the reinforcing steel bar and the surrounding concrete. According to Eq. 3.8, the accumulation of corrosion products on the rebar surface Δd can thus be considered as "$2u$" at the location of $r=r_i=r_b$, i.e.,

$$\Delta d/2 = u(r=r_b) = \frac{1-\upsilon}{E_c}\frac{r_b^2 p_b - r_0^2 p_0}{r_0^2 - r_b^2} r_b + \frac{1+\upsilon}{E_c}\frac{r_b^2 r_0^2 (p_b - p_0)}{r_0^2 - r_b^2}\frac{1}{r_b} \tag{3.48}$$

For the sake of convenience, Eq. 3.48 can be rewritten by ignoring Poisson's ratio υ:

$$\Delta d \approx \frac{2}{E_c(r_0^2 - r_i^2)}[(r_b^3 + r_b r_0^2)p_b - 2r_b r_0^2 p_0] \tag{3.49}$$

Chapter 4. Model Validation

4.1. Introduction

In order to assess the validity of the proposed model in describing the cracking resistance of the concrete cover, Eqs. 3.12 (cracking initiation at steel/concrete interface), 3.26 (longitudinal cracking of the concrete cover), 3.41 (longitudinal cracking of the concrete cover when confinement is provided in the elastic region), 3.47 (longitudinal cracking of the concrete cover when confinement is provided in the cracked region), and 3.49 (corrosion build-up generating the previous pressures) are compared with some experimental and finite element results in this chapter.

4.2. Model comparison with experimental results

In order to simulate a practical case, only experimental data from specimens with concrete tensile strength varying from 3 MPa to 8 MPa and ratio of cover to rebar diameter from 0 to 2 are selected in the comparison. In this section, the proposed models for both unconfined and confined concrete cylinder rings are compared with the data of unconfined concrete specimens reported by Williamson and Clark (2000) and Morinaga (1988), and the data of confined concrete specimens reported by Noghabai (1995). These experimental studies were chosen for comparison purposes since they provide the required input data for the analytical

models as well as output information provided by the analytical results.

4.2.1. Comparison with unconfined experimental results

Based on experimental tests, Morinaga (1988) proposed the following empirical expression for the prediction of critical bar pressure in concrete cylinder models without confinement:

$$p_{max} = f_t' (1 + 2c/d)^{0.85} \tag{4.1}$$

where f_t' is the concrete tensile capacity and c/d is the ratio of concrete cover to rebar diameter. Maximum failure bar pressures according to Eq. 4.1 are tabulated in Table 4.1.

Table 4.1: Maximum bar failure pressures (MPa) from Morinaga (1988)

	c/d=0.5	c/d=1	c/d=1.5	c/d=2
f_t'=3.5 MPa	6.9	9.7	12.	15
f_t'=5 MPa	9	12.7	16.2	19.6
f_t'=8 MPa	14.4	20.4	26	31.4

Williamson and Clark (2000) designed a test program to simulate the expansion pressure created by the accumulation of corrosion products on the surface of reinforcing bars. They used 150-mm concrete cubes with vertical holes of 8 or 16 mm diameter to simulate the location of the reinforcing bars. The rebar expansion pressure due to the corrosion was simulated by injecting high-pressure water into the holes. The failure pressure was defined as the maximum load sustained by the concrete cube at cracking of the cover.

Data from Williamson and Clark (2000) as well as from Morinaga (1988) are compared with the proposed model given by Eq. 3.26, which provides the required pressure necessary to crack the concrete cover when no confining reinforcement is provided. The results are plotted in Figs. 4 .1, 4.2, and 4.3, where "W. & C" denotes data from Williamson and Clark (2000) and "Mori." denotes data from Morinaga (1988). In the calculation of failure bar pressures using Eq. 3.26, the following parameters are used: bar diameter d = 8 mm, concrete cover c varies from 4 mm to 16 mm, crack number n = 1, and the characteristic length l_p = 240 mm, 228.5 mm, 110.7mm for f_t'=3.5, 5, and 8 MPa, respectively.

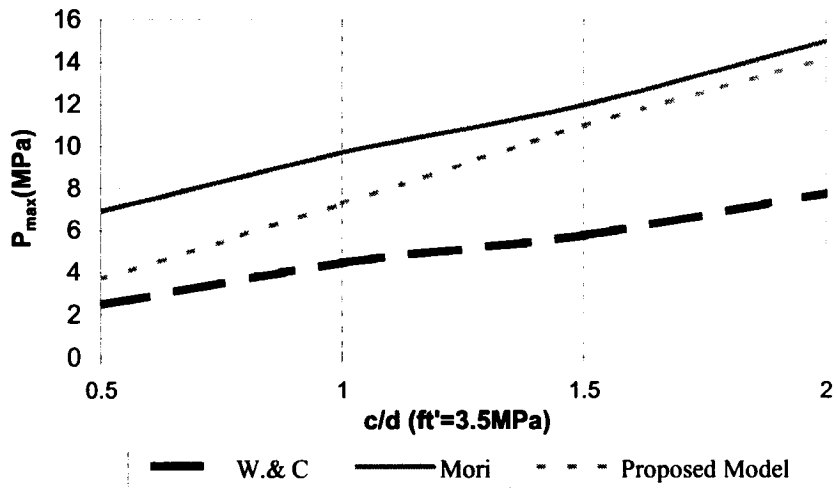

Fig. 4.1: Comparison of the bar failure pressures between Eq. 3.26 and some experimental results with f_t'=3.5 MPa

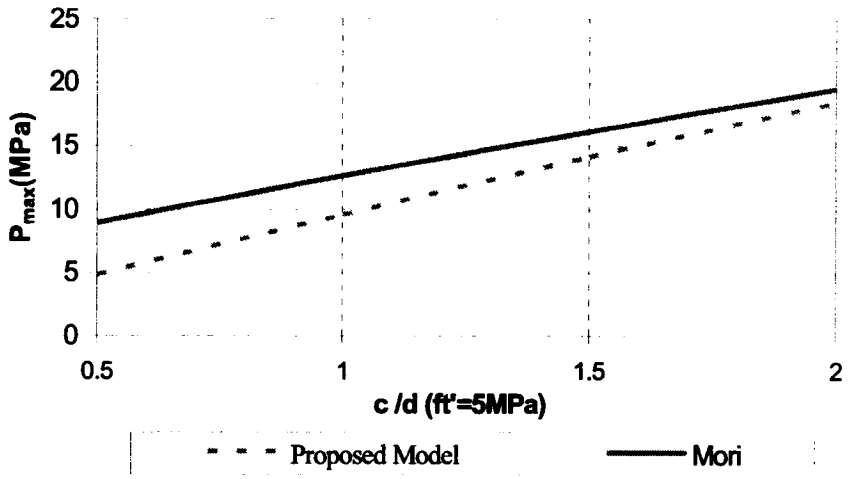

Fig. 4.2: Comparison of the bar failure pressures between Eq. 3.26 and some experimental results with f_t'=5 MPa

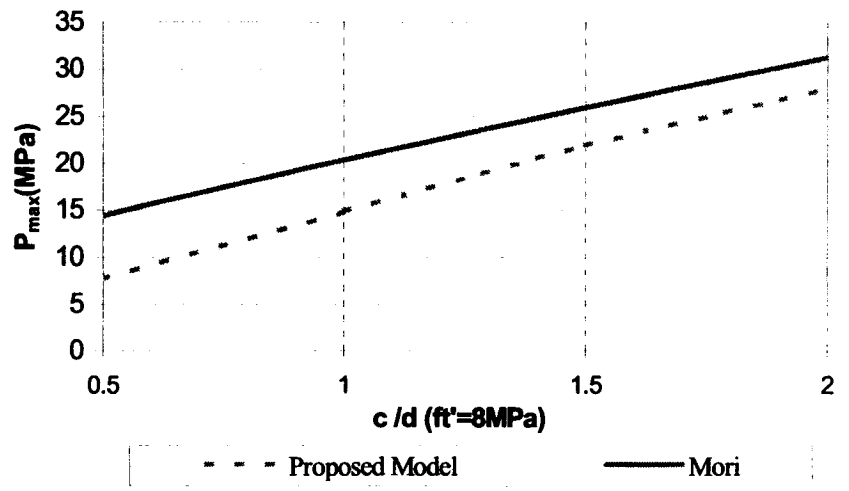

Fig. 4.3: Comparison of the bar failure pressures between Eq. 3.26 and some experimental results with f_t'=8 MPa

Compared with the experimental data from Williamson and Clark (2000) and Morinaga (1988), the results from the proposed model show similar trends. Values of the bar failure pressures from the proposed model are generally higher than those of Williamson and Clark (2000) and lower than those of Morinaga (1988). As the *c/d* increases, this divergence

becomes larger from Williamson and Clark's data and smaller from Morinaga's results. Unlike Williamson and Clark's experimental data, the bar failure pressures of the proposed model increase with the increase of concrete strength. Generally speaking, the failure bar pressures linearly increase with the ratio *c/d*. For the same concrete cover, as the bar diameter increases, the failure pressure is reduced. This is because the larger rebars have larger surfaces areas, and therefore have higher possibility to cause the surrounding concrete to crack. Along with the increase of concrete strength, the maximum bar failure pressure also increases.

4.2.2. Comparison with confined experimental results

From experimental tests, Noghabai (1995) obtained the critical bar pressures required to induce cracking of the concrete cover for concrete cylinders with confinement located in the cracked region (see Table 4.2).

Table 4.2: Maximum bar failure pressures (MPa) from Noghabai (1995)

	Confinement=Ø6@28 mm		Confinement=Ø6@14 mm	
	n	p_{max}(MPa)	*n*	p_{max}(MPa)
f_t'=3.78 MPa	4	28.9	5	31.8
f_t'=5 MPa	4	31.7	5	38.7
f_t'=8 MPa	1	50	6	48.7

where *n* is the number of observed cracks.

In order to assess the validity of the proposed Eq. 3.47, which provides the required pressure to induce longitudinal cracking when confining reinforcement is located in the cracked region, data from Noghabai (1995) are compared with the results from the proposed model. In the calculation of failure bar pressures using Eq. 3.47, the values of parameters used are those used by Noghabai (1995), as listed in Table 4.3.

Table 4.3: Parameters used in calculating the bar failure pressures using Eq. 3.47

	E_c(GPa)	G_f(Nm/m^2)	l_p	d_b	r_s	e	n
f_t'=3.78 MPa	33	105	240	18	40.5	138.5	4
f_t'=5 MPa	39.4	145	229	18	40.5	138.5	4
f_t'=8 MPa	41.2	172	111	18	40.5	138.5	4 6

The comparison results are plotted in Fig. 4.4, where "Nog.(14,28)" denotes the bar failure pressures with confinement of Ø6@14 mm and Ø6@28 mm from Noghabai (1995), and "proposed(14,28)" denotes the bar failure pressures with confinement of Ø6@14 mm and Ø6@28mm from the proposed model given by Eq. 3.47.

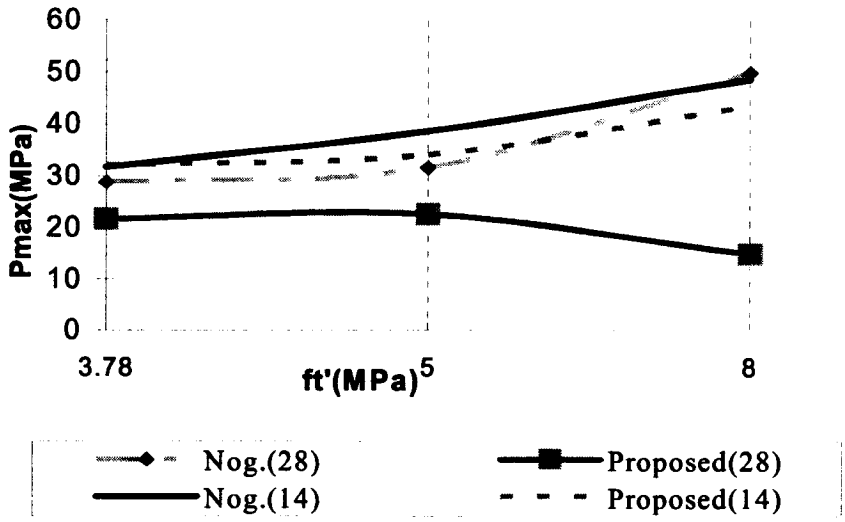

Fig. 4.4: Comparison of the bar failure pressures between Eq. 3.47 and Noghabai's experimental data (1995)

From the comparisons, it is found that the proposed model with confinement of Ø6@14 mm located at a distance of r_s=40.4 mm measured from the rebar center is very close to the experimental data from Noghabai (1995). On the other hand, the proposed model with confinement of Ø6@28 mm shows large discrepancy when compared with Noghabai's data. The discrepancy between the proposed model and Noghabai's data becomes very large when using n=1 and f_t'= 8 MPa to calculate the bar failure pressure. This is because Noghabai's experimental data is not affected by the number of observed cracks; on the contrary, the proposed model is very sensitive to the crack number, n.

4.3. Comparisons of model with finite element analysis

For the sake of investigating the corrosion-induced damage of reinforced concrete (rc) bridge decks, Zhou (2005) set up a numerical model using the finite element program

ABAQUS/Standard. In his model, the geometry of the rc bridge deck was dependent on the diameter of the rebar, d, the clear cover of the reinforced concrete bridge deck, c, and the spacing between rebars, s (see Fig. 4.5).

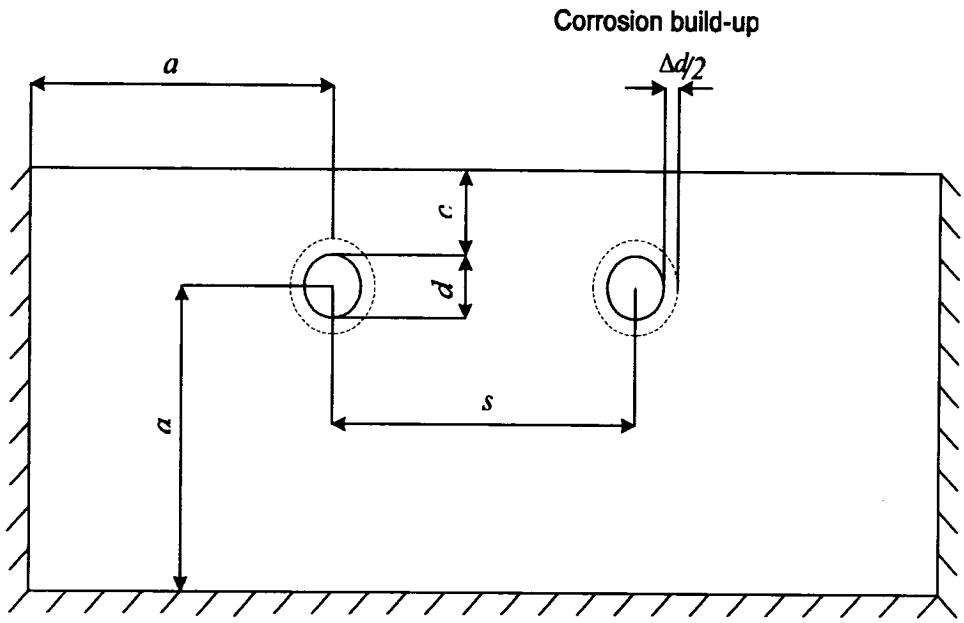

Fig. 4.5: Geometry of bridge deck model (adapted from Zhou (2005))

To simulate the actual damage of rc bridge decks due to corrosion, he meshed the above model into two finite element models (see Figs. 4.6 and 4.7) with linear and quadratic elements. In his models, he made three assumptions:

1. The rc deck was in a state of plain strain (i.e, ε_z=0).
2. The corrosion products were uniform around the surface of the rebar.
3. The quality and strength of the concrete were assumed to be time-independent.

The performance of both meshes was established by using a damaged plasticity model for concrete. The uniform displacement increments were applied on every node of the finite

elements along the rebar surface to simulate corrosion build-up around the rebar surface. The damage caused by corroding reinforcing bars was predicted by observing the displacement Δd around the rebar surface by using the Visualization module of ABAQUS/CAE.

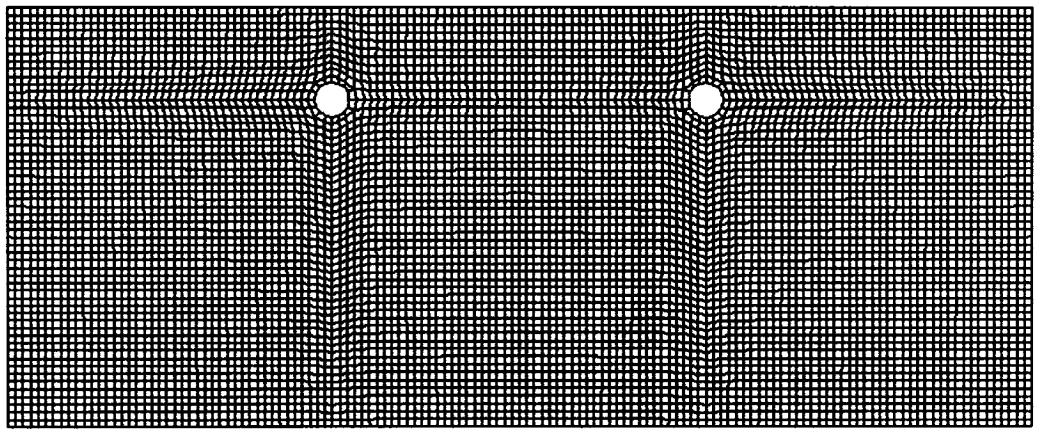

Fig. 4.6: Finite element mesh for linear elements (adapted from Zhou (2005))

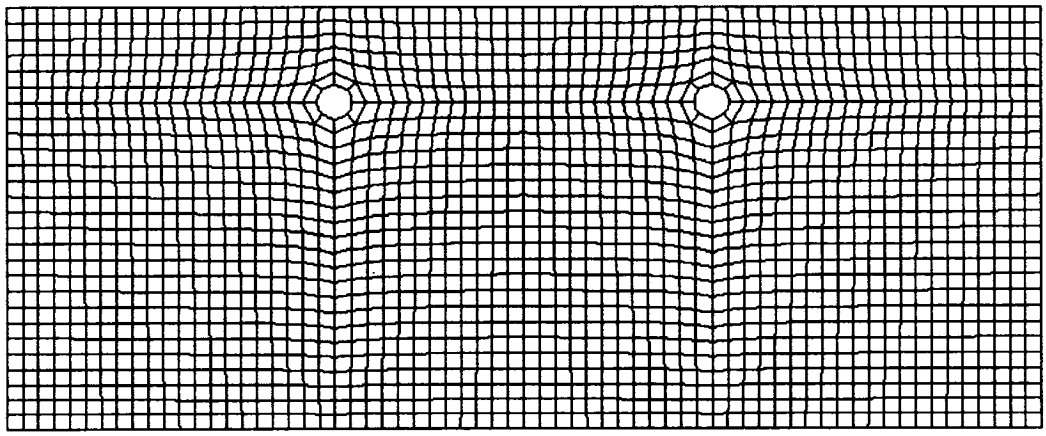

Fig. 4.7: Finite element mesh for quadratic elements (adapted from Zhou (2005))

In Zhou's models, the concrete splitting strength was taken as $f_t' = 0.33\sqrt{f_c'}$ and the modulus of elasticity of concrete E_c was taken as $E_c = 4700\sqrt{f_c'}$. By running the model in

the finite element program ABAQUS, Zhou obtained a series of values for the rebar radial displacement corresponding to the critical corrosion build-up levels at which initial and longitudinal cracking occur.

A comparison of the values of corrosion build-up causing cracking initiation and longitudinal cracking of concrete cylinders obtained by the analytical models presented in Chapter 3 and the finite element analyses presented by Zhou (2005) is made in this section.

4.3.1. Cracking initiation

The model for initiation of cracking at the surface of the reinforcing bar is formulated by combining Eq. 3.12 and Eq. 3.49 as follows:

$$\Delta d_1 = \frac{2f_t'}{E_c[(d/2+c)^2+(d/2)^2]}[(d/2)^3+(d/2)(d/2+c)^2] \tag{4.2}$$

Tables 4.4 and 4.5 present the comparative results between the finite element results obtained from Zhou (2005) for an rc bridge deck and the results from Eq. 4.2. Material properties used in this comparison between the finite element model and the proposed model are taken as follows: f'_c = 30 MPa, f'_t = 1.8 MPa, E_c = 25.7 GPa, and ν = 0.2.

Table 4.4: Δd_1 for an rc bridge deck with rebar diameters of 11 and 16 mm

c (mm)	d (mm)	s (mm)	Δd_1 (mm) (Zhou (2005)) (FEM)	Δd_1(mm)(Author's results) (Eq. 4.2)
35	11	81	0.0016	0.001467
35	11	86	0.0016	0.001467
35	11	92	0.0016	0.001467
35	11	100	0.0020	0.001467
35	11	110	0.0020	0.001467
35	11	120	0.0020	0.001467
35	11	160	0.0020	0.001467
50	11	80	0.0016	0.001612
50	11	111	0.0016	0.001612
50	11	120	0.0016	0.001612
50	11	152	0.0020	0.001612
50	11	160	0.0020	0.001612
50	11	218	0.0020	0.001612
65	11	80	0.0016	0.001613
65	11	141	0.0016	0.001613
65	11	160	0.0020	0.001613
65	11	195	0.0020	0.001613
65	11	205	0.0020	0.001613
65	11	275	0.0020	0.001613
35	16	80	0.0016	0.002133
35	16	86	0.0016	0.002133
35	16	105	0.0016	0.002133
35	16	115	0.0020	0.002133
35	16	130	0.0020	0.002133
35	16	173	0.0020	0.002133
50	16	80	0.0016	0.002339
50	16	116	0.0016	0.002339
50	16	140	0.0016	0.002339
50	16	157	0.0020	0.002339
50	16	170	0.0020	0.002339
50	16	230	0.0020	0.002339
65	16	80	0.0016	0.002342
65	16	146	0.0016	0.002342
65	16	170	0.0016	0.002342
65	16	200	0.0020	0.002342
65	16	210	0.0020	0.002342

Table 4.5: Δd_1 for an rc bridge deck with rebar diameters of 20 and 25 mm

c (mm)	d (mm)	s (mm)	Δd_1 (mm) (Zhou(2005)) (FEM)	Δd_1 (mm)(Author's results) (Eq.4.2)
35	20	80	0.0020	0.002667
35	20	90	0.0020	0.002667
35	20	110	0.0020	0.002667
35	20	120	0.0020	0.002667
35	20	130	0.0020	0.002667
35	20	182	0.0020	0.002667
50	20	80	0.0020	0.002900
50	20	120	0.0020	0.002900
50	20	140	0.0020	0.002900
50	20	160	0.0020	0.002900
50	20	180	0.0020	0.002900
50	20	240	0.0020	0.002900
65	20	120	0.0020	0.002924
65	20	150	0.0020	0.002924
65	20	180	0.0020	0.002924
65	20	204	0.0020	0.002924
65	20	220	0.0020	0.002924
65	20	297	0.0020	0.002924
35	25	80	0.0028	0.003333
35	25	95	0.0026	0.003333
35	25	130	0.0026	0.003333
35	25	160	0.0030	0.003333
35	25	200	0.0030	0.003333
50	25	80	0.0024	0.003641
50	25	125	0.0020	0.003641
50	25	160	0.0030	0.003641
50	25	252	0.0030	0.003641
65	25	130	0.0024	0.003650
65	25	155	0.0024	0.003650
65	25	190	0.0030	0.003650
65	25	310	0.0030	0.003650

The results listed in Tables 4.4 and 4.5 are also plotted in Fig. 4.8 as a function of *c/d* versus Δd_1, where "Zd=11mm" means the data from Zhou (2005) with rebar diameter equal to 11 mm and "Pd=11mm" means the data from the proposed model with rebar diameter equal to 11 mm, etc. In order to eliminate the interactive influence from the adjacent rebars, only the values of FEM Δd_1 with larger rebar spacing in Table 4.5 are plotted.

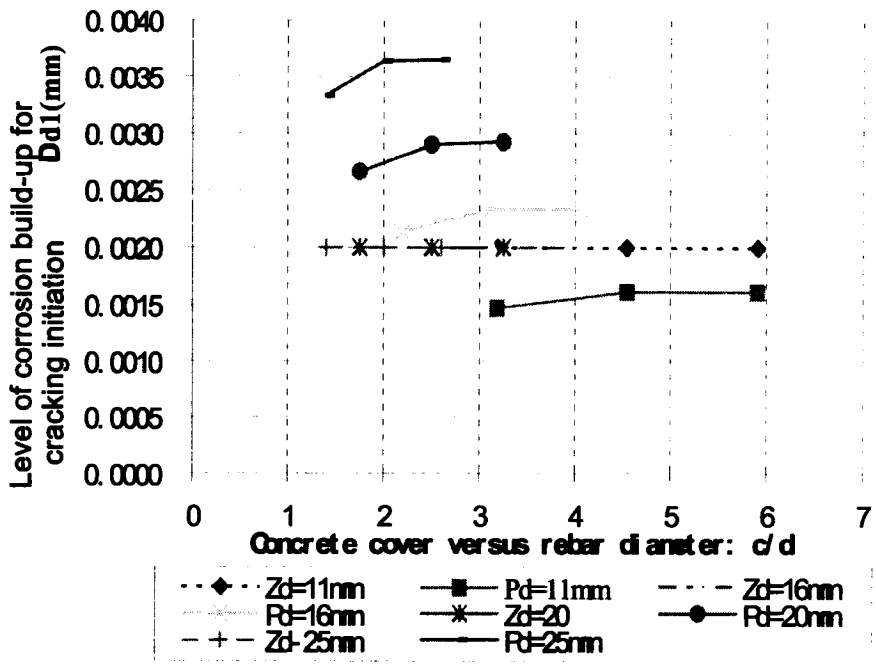

Fig. 4.8: Influence of *c/d* on the level of corrosion build-up for cracking initiation

Figure 4.8 illustrates that Δd_1 obtained from the proposed model is not constant. The computed values vary with the change of rebar diameter and the ratio of concrete cover to rebar diameter. On the contrary, the finite element results reported by Zhou (2005) show the unchanged constant values through all the range of the ratio *c/d*. However, the average value from the proposed model shows the same trends as that of the FEM results.

4.3.2. Longitudinal cracking

The model for longitudinal cracking of the concrete cover is formulated by combining Eq. 3.26 and Eq. 3.49 as follows:

$$\Delta d_2 = \frac{2}{E_c[(d/2+c)^2-(d/2)^2]}[(d/2)^3+(d/2)(d/2+c)^2]\,p_{b\max} \tag{4.3}$$

where $p_{b\max}$ is the maximum value given by Eq. 3.26 with e varying from $d/2$ to $d/2+c$.

Tables 4.6 and 4.7 present the comparative results between the finite element results obtained from Zhou (2005) for an rc bridge deck and the proposed model from Eq. 4.3. Material properties used in this comparison between the finite element model and the proposed model are taken as follows: f'_c = 30 MPa, f'_t = 1.8 MPa, E_c = 25.7 GPa, ν = 0.2, n=3, l_p=240 mm. The characteristic length l_p is a value dependent on the fracture energy G_f, concrete modulus E_c, and concrete splitting strength f_t' (see section 3.2.2). For a concrete with f'_t = 1.8 MPa and E_c = 25.7 GPa, the characteristic length l_p=240mm. Noghabai (1995) experiments showed that when the number of cracks-n ranged between 2 and 10, the bar failure pressures were very sensitive to it. Although the crack number-n can take any value, it is not realistic for a concrete cylinder to show such cracking behaviour, and also it is very conservative to estimate the concrete cylinder splitting capacity when it fails with only 2 radial cracks. Hence, in this section, the crack number-n is taken as 3. For the influence of the crack number-n on the bar failure pressure due to the corrosion build-up, chapter 5 will give more details.

Table 4.6: Δd_2 for an rc bridge deck with rebar diameters of 11 and 16 mm

c (mm)	d (mm)	s (mm)	Δd_2 (mm) (Zhou(2005)) (FEM)	Δd_2 (mm)(Author's results) (Eq.4.3)
35	11	92	0.0230	0.002752
35	11	100	0.0226	0.002752
35	11	110	0.0240	0.002752
35	11	120	0.0240	0.002752
35	11	160	0.0230	0.002752
50	11	111	0.0354	0.003760
50	11	120	0.0350	0.003760
50	11	152	0.0350	0.003760
50	11	160	0.0340	0.003760
50	11	218	0.0340	0.003760
65	11	80	0.0520	0.004403
65	11	141	0.0516	0.004403
65	11	160	0.0510	0.004403
65	11	195	0.0500	0.004403
65	11	205	0.0500	0.004403
65	11	275	0.0510	0.004403
35	16	86	0.0178	0.002842
35	16	105	0.0164	0.002842
35	16	115	0.0170	0.002842
35	16	130	0.0170	0.002842
35	16	173	0.0160	0.002842
50	16	80	0.0290	0.003831
50	16	116	0.0286	0.003831
50	16	140	0.0278	0.003831
50	16	157	0.0260	0.003831
50	16	170	0.0270	0.003831
50	16	230	0.0290	0.003831
65	16	146	0.0402	0.004784
65	16	170	0.0394	0.004784
65	16	200	0.0380	0.004784
65	16	210	0.0390	0.004784

Table 4.7: Δd_2 for an rc bridge deck with rebar diameters of 20 and 25 mm

c (mm)	d (mm)	s (mm)	Δd_2 (mm) (mm) (Zhou(2005)) (FEM)	Δd_2 (mm)(Author's results) (Eq.4.3)
35	20	90	0.0150	0.002931
35	20	110	0.0150	0.002931
35	20	120	0.0150	0.002931
35	20	130	0.0150	0.002931
35	20	182	0.0140	0.002931
50	20	80	0.0264	0.003900
50	20	120	0.0272	0.003900
50	20	140	0.0270	0.003900
50	20	160	0.0260	0.003900
50	20	180	0.0260	0.003900
50	20	240	0.0230	0.003900
65	20	120	0.0426	0.004846
65	20	150	0.0364	0.004846
65	20	180	0.0350	0.004846
65	20	204	0.0350	0.004846
65	20	220	0.0350	0.004846
65	20	297	0.0350	0.004846
35	25	80	0.0186	0.003051
35	25	95	0.0172	0.003051
35	25	130	0.0174	0.003051
35	25	160	0.0160	0.003051
35	25	200	0.0170	0.003051
50	25	80	0.0258	0.003998
50	25	125	0.0258	0.003998
50	25	160	0.0270	0.003998
50	25	252	0.0210	0.003998
65	25	130	0.0396	0.004622
65	25	155	0.0352	0.004622
65	25	190	0.0370	0.004622
65	25	310	0.0370	0.004622

The comparison results in Tables 4.6 and 4.7 are plotted in Fig. 4.9 as a function of c/d versus Δd_1. In general, the proposed analytical model underestimates the required level of corrosion build-up to induce longitudinal cracking.

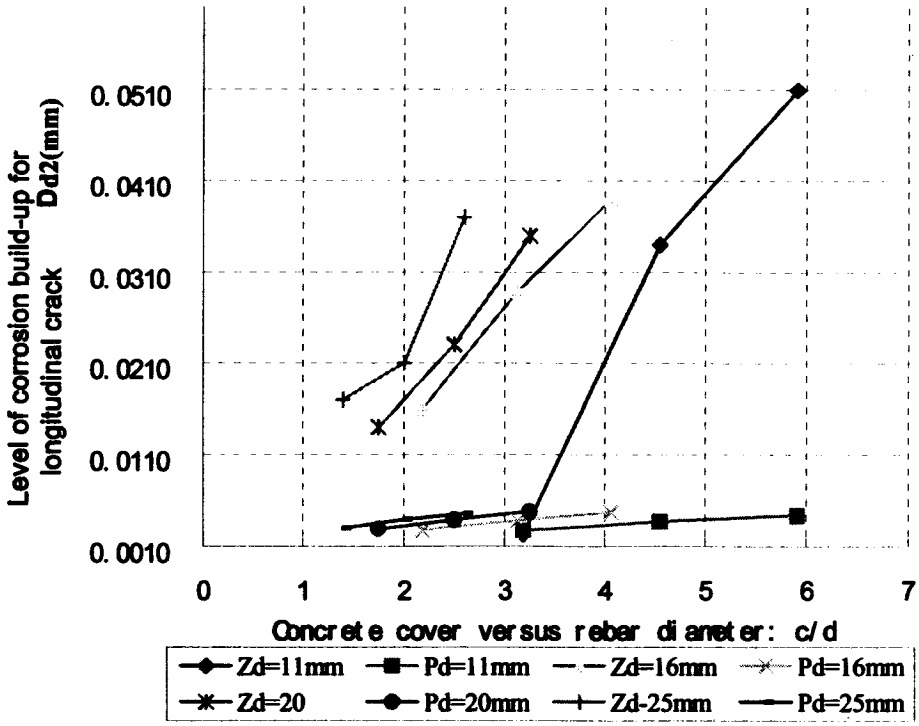

Fig. 4.9: Influence of *c/d* on the level of corrosion build-up for longitudinal cracking

4.4. Summary of model behaviour

By introducing the linear relationship of ϵ_t and σ_t in the concrete softening region, the proposed model shows close results when compared with the experimental/numerical data from Morinaga (1988), Noghabai (1995), Williamson and Clark (2000), and Zhou (2005). Compared with models that do not account for the concrete softening behaviour in the calculation of the failure bar pressures due to the corrosion build-up around the rebars, the proposed model presents very high values of the bar failure pressures. The bar failure pressures depend on many parameters such as the ratio of concrete cylinder cover to rebar

diameter-c/d, crack number-n, characteristic length-l_p, equivalent length of confinement-l_{eq}, as well as the location of confinement r_s. When changing these parameters, the maximum bar failure pressures correspondingly change. This process is validated by the comparison results with some researchers' experimental/numerical data.

Chapter 5. Parametric Analysis

5.1. Introduction

In chapter 3, equations 3.26, 3.41, and 3.47 are proposed based on the strain compatibility of $\varepsilon_t = \varepsilon_{cr}$ (see Eq. 3.17) and the relationship between σ_t and w (see Eq. 3.16) in the concrete softening region. The model presented in Eq. 3.26 illustrates the relationship of bar pressure and crack front in unconfined concrete. The model in Eq. 3.41 shows the influence of the confinement on the bar pressure when the confinement is located in the uncracked concrete region. The model described by Eq. 3.47 exhibits the effects of the confinement on the bar pressure when the confinement is located in the cracked concrete region.

In order to study the sensitivity of Eqs. 3.26, 3.41, and 3.47, simulations are presented in Appendix A, and the effects of the input parameters on the bar failure pressures are studied in this chapter. The chosen analyses cover normal strength concrete (NSC), high strength concrete (HSC), and very high strength concrete (VHSC). In this thesis, NSC refers to concrete with a tensile strength of 3.8 MPa, HSC refers to a concrete with a tensile strength of 5 MPa, and VHSC refers to a concrete with a tensile strength of 8 MPa. This division has been adopted to compare the results with the experimental data reported by Noghabai (1995).

5.2. Sensitivity analysis

An analysis was conducted to study the sensitivity of the proposed models to the various input parameters, and it is presented in Appendix A. In each concrete strength level, two different rebar diameters d (8 and 16 mm) with various concrete cover thicknesses c ($0.5d$ to $2d$) were considered in the analyses using Eqs. 3.26, 3.41, and 3.47. Because of the nonlinearity of the above equations, in order to find the maximum bar failure pressures in the concrete cover, iterative calculations were performed with respect to an arbitrary crack front e. The maximum rebar pressure was selected as the bar failure pressure inducing cracking in the concrete cover due to corrosion build-up. The values of the crack front-e corresponding to the bar failure pressures are the critical crack fronts, at which levels the longitudinal cracks occur.

5.2.1. Input parameters

Input parameters related to concrete material properties used in the sensitivity analysis are listed in Table 5.1.

Table 5.1: Summary of concrete properties

Specimen	E_c (GPa)	f_t' (MPa)	G_f (N/mm)	l_p (mm)	f_c' (MPa)
NSC	33	3.8	0.105	240	40
HSC	39.4	5.0	0.142	228.5	70
VHSC	41.2	8.0	0.172	110.7	178

where E_c is the elastic modulus of concrete, G_f is the fracture energy of concrete, f_t' is the

tensile strength of concrete, l_p is the characteristic length for concrete, and f'_c is the concrete compressive strength. This latter parameter was obtained from converting the tensile strengths reported by Noghabai (1995) according to $f_t' = 0.6\sqrt{f_c'}$ for high strength concrete (ACI Committee 363, 1997) and $0.33\sqrt{f_c'}$ for normal strength concrete. Other input parameters required in Eqs. 3.26, 3.41, and 3.47 are the equivalent area of spiral bar A_{eq}, which was set to 1.01 mm^2/mm for an spiral bar of Ø6@28 mm, and the elastic modulus of steel E_s, set equal to 210 GPa. Values of l_{eq} corresponding to different number of cracks are listed in Table 5.2 (based on Noghabai's experimental data).

Table 5.2: Values of l_{eq}

Crack No.	1	3	4	5	6	7
l_{eq} (mm)	254	85	64	51	42	36

To make systematical and continuous comparisons, the analyses are sorted into several groups. Each group has the same strength properties (see Table 5.1), same crack numbers (here, n is only taken as 2 for all analyses), same bar diameters (d), and same concrete cover thickness (c). In order to find the maximum bar failure pressures p_{max}, the crack front e is varied from $d/2$ to $d/2+c$ for unconfined specimens, from $d/2$ to r_s for specimens where the confining reinforcement is located in the uncracked region of the concrete cover, and from r_s to $c+d/2$ for specimens where confinement is provided in the cracked region of the concrete cover. All results are tabulated in Tables A1 through A24. The format of each table is as follows: material characteristics are displayed on the first row of the table; crack front (e)

varies as previously described and is presented on the second row of the table; the third, fourth, and fifth rows of the tables exhibit the bar pressures calculated using Eqs. 3.26, 3.41, and 3.47, respectively, at the corresponding crack fronts; finally, the last column of the table gives the maximum bar failure pressure. For visualization purposed, the results are also plotted in Figs. A1 to A24.

5.2.2. Summary of test results

In order to easily make comparisons, the maximum bar pressures of all analyses from Tables A1 through A24 are listed and illustrated in Tables 5.3, 5.4, 5.5, and Figs. 5.1, 5.2, and 5.3. The notation used in the following tables and figures is as follows:

c/d: ratio of concrete cover thickness to rebar diameter

p_{max}: maximum bar failure pressure (MPa)

Nd: normal-strength concrete

Hd: high-strength concrete

Vd: very-high-strength concrete

UNd: normal-strength concrete and no confinement provided

UHd: high-strength concrete and no confinement provided

UVd: very-high-strength concrete and no confinement provided

CUNd: normal-strength concrete and confinement in uncracked region

CUHd: high-strength concrete and confinement in uncracked region

CUVd: very-high-strength concrete and confinement in uncracked region

CCNd: normal-strength concrete and confinement in cracked region

CCHd: high-strength concrete and confinement in cracked region

CCVd: very-high-strength concrete and confinement in cracked region

Table 5.3: Maximum bar pressures for unconfined concrete

Unconfined	p_{max} (MPa)					
c/d	Nd=8mm	Nd=16mm	Hd=8mm	Hd=16mm	Vd=8mm	Vd=16mm
0.5	3.75	3.71	4.93	4.87	7.9	7.6
1	7.4	7.25	9.73	9.5	15.2	14.6
1.5	11	10.6	14.3	14	22.3	21
2	14.5	13.9	19	18.2	29	27

Table 5.4: Maximum bar pressures for concrete confined at uncracked region (r_s =*d/2+3c/4* mm)

Confined @ uncrackedpart	p_{max}(MPa)					
c/d	Nd=8mm	Nd=16mm	Hd=8mm	Hd=16mm	Vd=8mm	Vd=16mm
0.5	9.85	6.7	11.7	8.2	18	12.7
1	13.5	10.3	16.4	12.8	25.4	19.4
1.5	17	13.6	21.1	17.1	32.2	25.5
2	20.5	16.7	25.6	21.3	38.7	31.4

Table 5.5: Maximum bar pressures of concrete confined at cracked region (r_s = *d/2+c/5* mm)

Confined @ crackedpart	p_{max}(MPa)					
c/d	Nd=8mm	Nd=16mm	Hd=8mm	Hd=16mm	Vd=8mm	Vd=16mm
0.5	28.1	16.4	40.2	23.3	94.2	52.8
1	32.9	21	46.7	29.6	106	63.5
1.5	37.6	25.6	53	35.6	117	73.3
2	42.2	29.6	59.2	41.3	127	82.2

The data in Tables 5.3, 5.4, and 5.5 are illustrated in Figs. 5.1, 5.2, and 5.3, respectively.

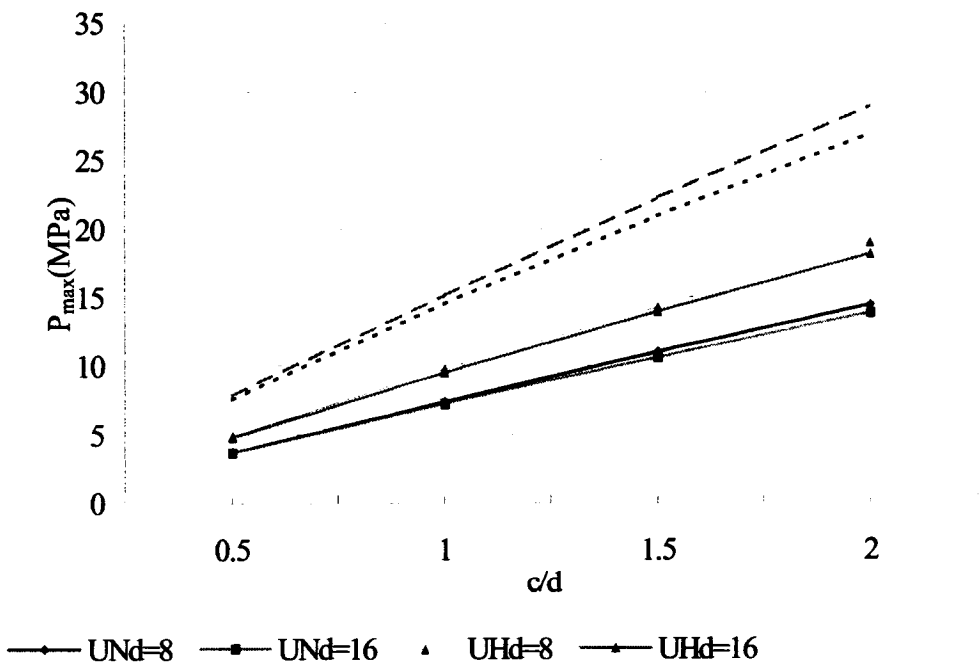

Fig. 5.1: Illustration of p_{max} versus *c/d* for unconfined concrete (Eq. 3.26)

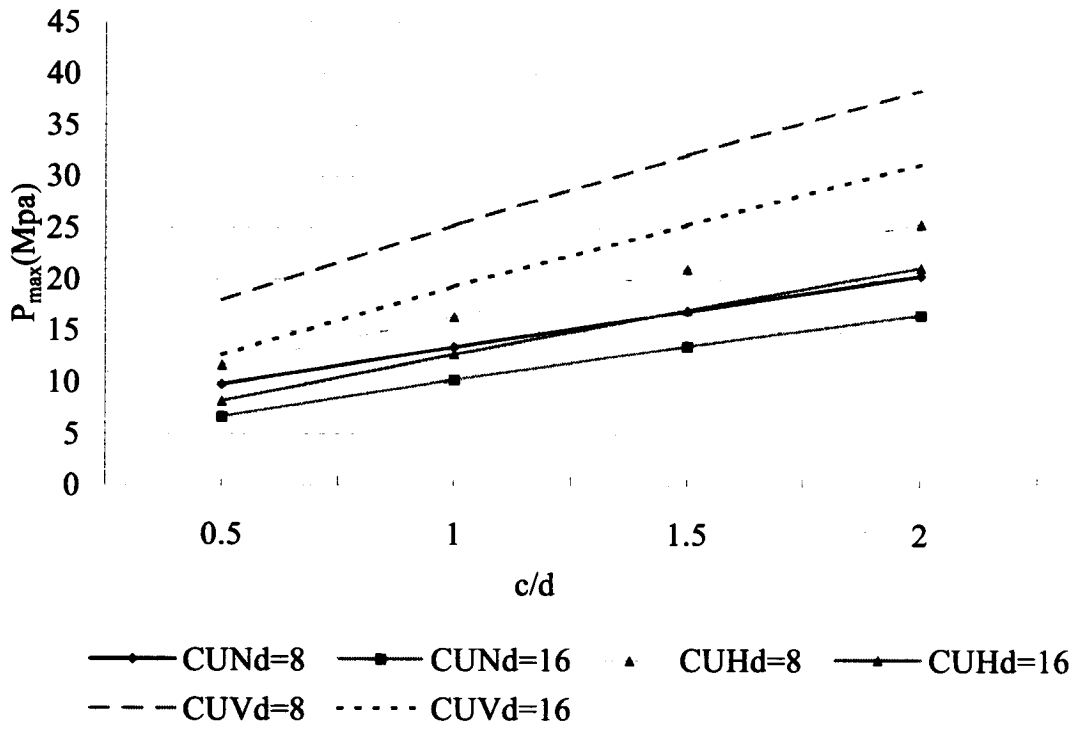

Fig. 5.2: Illustration of p_{max} versus *c/d* with confinement at uncracked region (Eq. 3.41)

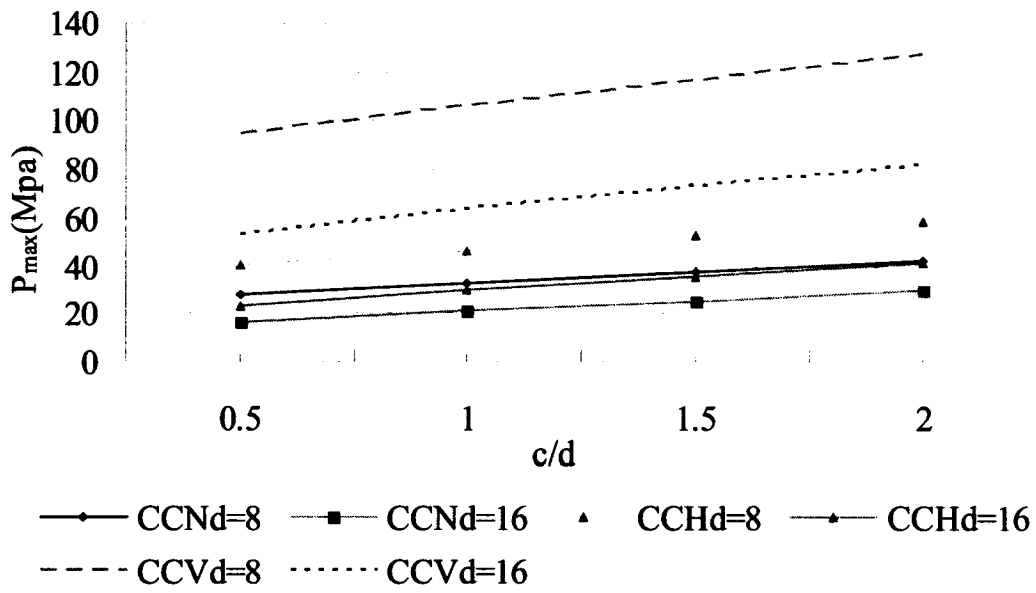

Fig. 5.3: Illustration of p_{max} versus *c/d* with confinement at cracked part (Eq. 3.47)

5.3. Effect of f_c'

From the above results, it is found that the bar failure pressures increase slightly with the increase of the concrete tensile strength f_t'. In other words, the bar failure pressures of the proposed models are basically independent of parameter f_t'. In order to compare the test results in terms of p_{max} versus f_c', the concrete tensile strength f_t' is converted to f_c' according to $f_t'=0.6\sqrt{f_c'}$ for high and very high strength concretes (ACI Committee 363, 1997) and $0.33\sqrt{f_c'}$ for normal strength concrete, and the new comparison results are plotted in Fig. 5.4.

Figure 5.4 shows that the effects of the concrete strength f_c' on the rebar failure pressures p_{max} for both Eq. 3.26 (longitudinal cracking without confinement) and Eq. 3.41 (longitudinal cracking with confinement in uncracked region) are very slight. On the contrary, the influence of concrete strength on rebar failure pressure for Eq. 3.47 (longitudinal cracking with confinement in cracked region) is very obvious.

5.4. Effect of *c/d*

The ratio of concrete cover to the rebar diameter-*c/d* has significant effect on the bar failure pressure. With the increase of the ratio of *c/d* from 0.5 to 2, the bar failure pressures increase almost 2 to 3 times of the original values. To illustrate the effect of *c/d* on the bar failure pressure, the results for the concrete cylinder model with rebar diameter d=16mm is plotted in Fig. 5.5 as an example.

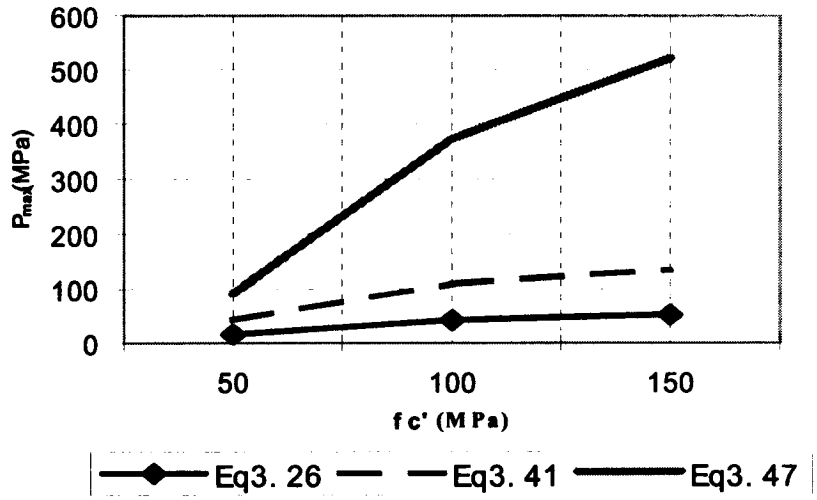

Fig. 5.4: Effect of concrete strength on the rebar failure pressures

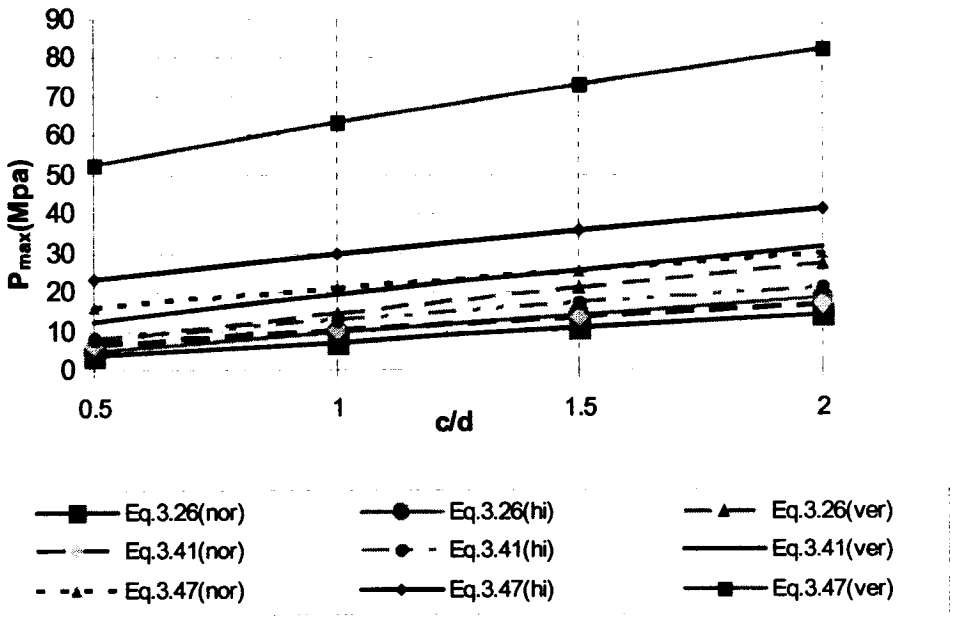

Fig. 5.5: Effect of *c/d* on the bar failure pressures

5.5. Effect of *n*

In order to find the effect of the number of cracks *n* on the bar failure pressures, Eqs. 3.26, 3.41, and 3.47 are plotted against the number of cracks-*n*. Parameters used in the calculation are set as follows: A_{eq} = 1.01 mm^2/mm for the spiral bar confinement of Ø6@28 mm, E_s = 210 GPa, E_c = 41.2GPa for elastic modulus of VHSC concrete, G_f = 0.172 N/mm, f_t' = 8 MPa for the tensile strength of VHSC concrete, d = 16 mm, c = 32 mm, l_{eq} = 254 mm for the equivalent length of the confining rebar crossing cracks, and l_p = 111 mm.

The above parameters were plugged into Eqs. 3.26, 3.41, and 3.47 to determine the maximum pressures required to induce cracking of the concrete cover for different values of *n* ranging from 1 to 10. The influence of the number of cracks on the rebar pressure p_{max} is illustrated in Fig. 5.6.

From Fig. 5.6, it is found that the bar failure pressures are slightly dependent on the number of cracks-*n*. Although the crack number-*n* can take any value, it is not realistic for a concrete cylinder to show such cracking behaviour (Noghabai, 1995), and it is also very conservative to estimate the concrete cover splitting capacity when it fails with only 1 or 2 radial cracks. Hence, it is suggested that the number of cracks-*n* be taken as 3 in the proposed equations.

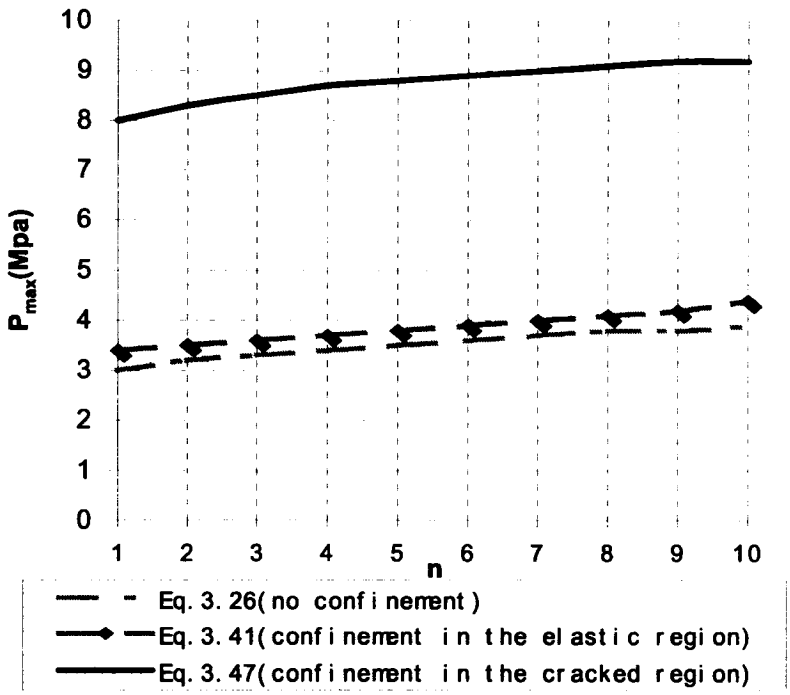

Fig. 5.6: Effect of number of cracks on the bar failure pressures

5.6. Effect of l_p

In chapter 3, it was shown that $l_p \approx E_c G_F / f_t'^2$ where G_F is the true fracture energy calculated from $G_F = \int_0^{w_c} \sigma(w)dw$. The concrete characteristic length l_p reflects the flexibility of concrete, and it is in inverse proportion to the concrete strength. Increasing l_p means reducing the material brittleness, and the material becomes more plastic. The parameters mentioned in section 5.5 are used in Eqs. 3.26, 3.41, and 3.47 to find the effect of l_p on the bar failure pressures. The results are shown in Fig. 5.7.

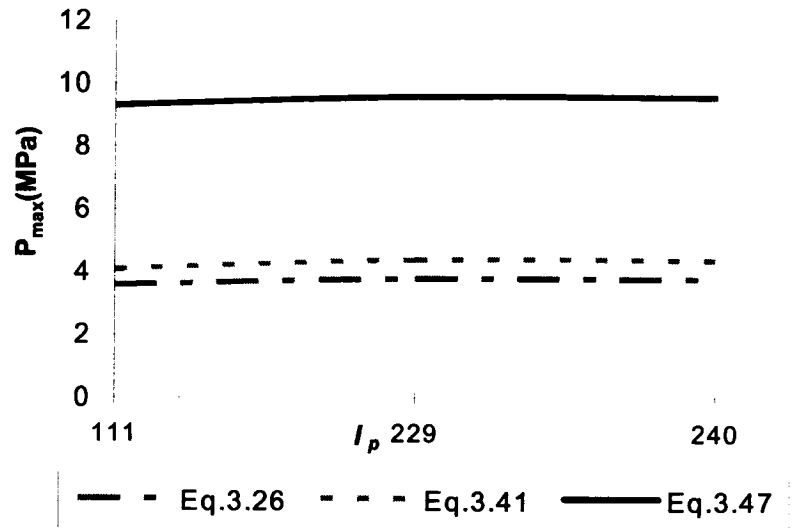

Fig. 5.7: Effect of l_p on the bar failure pressures

By increasing the values of the concrete characteristic length l_p from 111 to 240 mm, a slight increase of the critical bar pressures is observed. In other words, the bar failure pressures are independent of l_p. This is because the characteristic length l_p reflects the fracture properties of concrete. Without correspondingly modifying the concrete strength, modulus, as well as the fracture energy (see the expression of l_p in chapter 3), the characteristic length does not affect the bar failure pressures.

5.7. Effect of confinement

Because the confinement index A_{eq} does not affect Eqs. 3.26, only Eqs. 3.41 and 3.47 are chosen to make the comparison. The parameters mentioned in section 5.5 are used in the calculations using Eqs. 3.41 and 3.47 to find the effect of the confinement on the bar failure pressures with respect to A_{eq}. The results are shown in Fig. 5.8, wherein A_{eq} is ranged from 1

mm^2/m to 3.5 mm^2/m.

By comparing to the confinement located at the concrete uncracked regions, the confinement located at the concrete cracked regions can substantially increase the cracking capacity of the concrete cover as illustrated in Fig. 5.8.

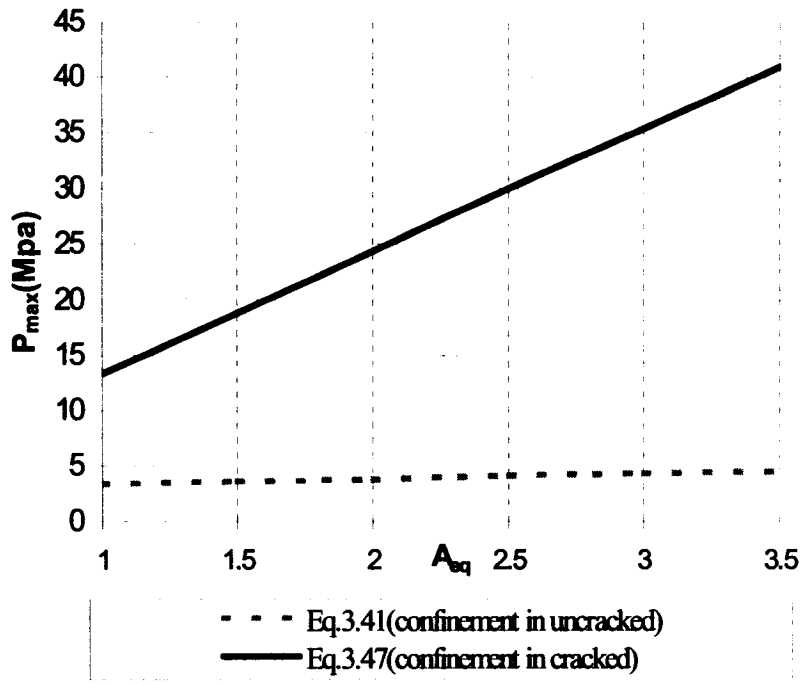

Fig. 5.8: Effect of confinement on the bar failure pressures

On the contrary, when the confinement is located at the cracked regions, the splitting capacity of the concrete cylinder decreases with the increase of the ratio of r_s to d. This is because when the confinement is located near the rebar center at the cracked regions, the spiral reinforcing steel sustains higher tensile stresses, which contributes to the higher concrete splitting capacity.

In order to study the effect of the location of the confinement on the bar failure pressures, the location r_s of the confinement is set as the variable in the calculations using Eqs. 3.41 and 3.47, with all the parameters defined in section 5.5 remaining the same. The results are shown in Fig. 5.9.

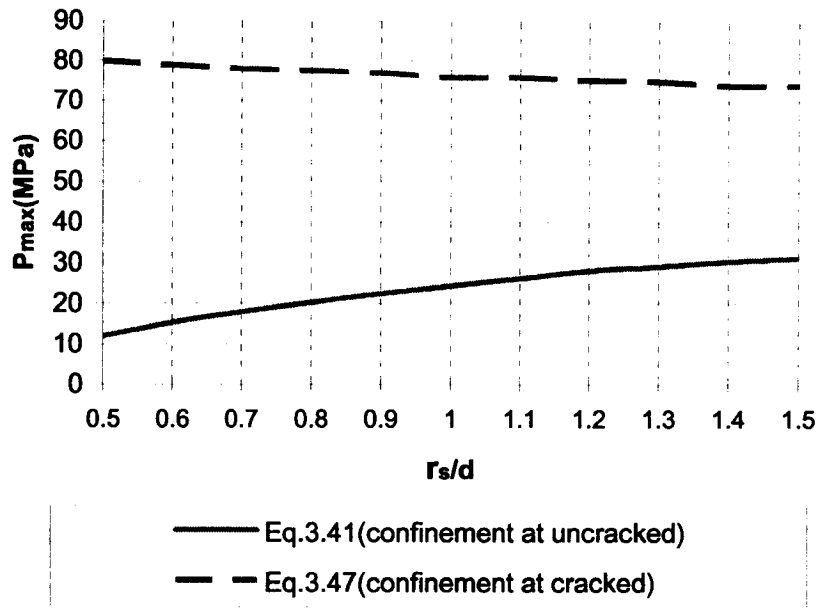

Fig. 5.9: Effect of the location of the confinements on the bar failure pressures

It is found that the contribution of the location of the confinement on the bar failure pressures decreases with the increase in the distance when the confinement is located in the cracked regions and increases with the distance when the confinement is located in the uncracked regions. Usually, when the confinement is located very close to the rebar, the maximum bar failure pressure is governed by the location of the confinement r_s. This is because the crack front quickly reaches the confinement, whereas the function established in

Eq. 3.41 does not exhibit a parabola–like peak point yet. In other words, the maximum bar failure pressure is obtained from Eq. 3.41 by setting the crack front e equal to r_s. Once the crack front e exceeds the confinement r_s, Eq. 3.41 must be replaced by Eq. 3.47 to calculate the maximum bar failure pressure.

Compared with the concrete characteristic length l_p and the number of cracks-n, the confinement provided in the cracked concrete can make a larger contribution to the bar failure pressure. Considering many factors such as economy, conditions of construction site, and current engineering technology, confinement in concrete will be the first choice to enhance the concrete splitting capacity in resisting the cracking of the concrete cover.

Chapter 6. Concluding Remarks

6.1. Summary

In this thesis, a concrete thick-wall cylinder subjected to internal pressure is used to simulate corrosion-induced damage and describe the relationship between stresses and strains in the concrete cover. The concrete discussed in this thesis is assumed isotropic and elastic. Under these assumptions, formulae describing the relations of stresses and strains, stresses and corrosion build-up, and stresses and confinement in the cylinder ring model were derived. In order to assess the sensitivity of these models, simulations where the concrete strength varied from normal strength to very high strength were carried out. Comparisons between the results from the proposed models in this thesis and that from other researchers were made. At last, the effects on the proposed models due to some parameters such as the number of cracks, the concrete characteristic length, and confinement were clearly identified.

6.2. Conclusions

From the parametric analysis, it is found that bar failure pressures increased with the increase of the ratio of *c/d*. The number of cracks n and concrete characteristic length l_p have a smaller effect on bar pressures compared with the ratio of *c/d*. Confinement played a very

important role in enhancing the concrete cover tensile capacity, and the effect of confinement is obvious from the results. For the same concrete cover thickness, smaller diameter bars have higher bar failure pressures than larger diameter bars do. Among the above factors, the most significant parameter affecting bar failure pressure is the ratio of *c/d*, and the least significant parameter affecting bar failure pressure is the reinforcing bar diameter-*d*.

The models proposed in this thesis use for the first time a linear relationship of stress/strain and a constant elongation in the concrete softening region. This approach differs from previous researchers such as Tepfers (1979), Van der veen (1990), and Noghabai (1995). By applying fracture mechanics in the proposed models, the state of stresses and strains in the concrete cover can be reasonably predicted, as illustrated in chapter 4, where comparisons are made with the experimental data from Williamson and Clark (2000) and Morinaga (1988), and numerical data from Zhou (2005). The comparison results between the proposed model and experimental data show that the results from the proposed model follow the same trends as the experimental data. In other words, the proposed models are practical and feasible.

Compared with the finite element results from Zhou (2005), the proposed models show some conservative trends in predicting the bar failure pressures. This source of discrepancy is mostly due to the use of different geometries of the models, as well as the application of the anisotropic behaviour of the concrete under softening conditions (e.g. the linear

relationship of stress/strains and the constant elongation in the concrete softening regions) in the calculation of bar failure pressures. Realistically, most concrete structures are in the shapes of rectangle rather than circle, such as the rectangular rc deck, which can provide more resistance to cracking than just assuming the cover as a thick-wall cylinder. Therefore, idealizing the concrete cover as a thick-wall cylinder subjected to internal pressure provides conservative estimates of the cover's resistance to corrosion-induced cracking. In order to eliminate the discrepancy of the results between the proposed model and the finite element data, and also improve the accuracy of predicting the bar failure pressures, influence from the geometry as well as the more accurate relationship between the stresses and the strains in the softening regions should be introduced in the future.

6.3. Future work

Due to the lack of some parameters of anisotropic material such as E_{rt}, E_{tr}, ν_{tr}, and ν_{rt}, the assumption that the material is isotropic is applied in this thesis. As a result, the effects of anisotropy are neglected. However, concrete under softening behaviour is known to show very strong anisotropic properties, which cannot be neglected in the model analysis. Consequently, the introduction of these anisotropic effects will be necessary in future research works. Nonetheless, in this thesis, the model developed provides a basic tool for understanding and analysis of the associated mechanical problem. Along with the extension of research and the development of technology, more detailed and general cases such as

members with irregular cross sections rather than circular, and steel cables rather than straight single steel rebars need to be studied.

References

ACI Committee 363 (1997). "State-of-the-Art Report on High-Strength Concrete." *ACI 363R-92*, American Concrete Institute.

Andrade, C., Alonso, C., and Molina, F.J. (1993). "Cover cracking as a function of bar corrosion: part I-experimental test." *Materials and Structures*, **26**, 453–464.

Bažant, Z. (1979). "Physical model for steel corrosion in concrete sea structures – Application." *Journal of the Structural Division*, **105**(6), 1155–1166.

Guiriani, E., Plizzari, G., and Schumm, C. (1991). "Role of stirrups and residual tensile strength of cracked concrete on bond." *Journal of Structural Engineering*, **117**(1), 1–18.

Hansen, E.J., and Saouma, V. E. (1999). "Numerical simulation of reinforced concrete deterioration: part II—steel corrosion and concrete cracking." *ACI Materials Journal*. 96(3), 331–338.

Karihaloo, B.L. (1995). *Fracture Mechanics and Structural Concrete* (2nd ed.), Longman Scientific & Technical, Sydney.

Liu, Y., and Weyers, R. E. (1998). "Modelling the time-to-corrosion cracking in chloride contaminated reinforced concrete structures." *ACI Materials Journal*, **95**(6), 675-681.

Martín-Pérez, B. (1999). *Service Life Modelling of R.C. Highway Structures Exposed to Chlorides*. Ph.D. dissertation, Dept. of Civil Engineering, University of Toronto.

Molina, F.J., Alonso, C., and Andrade, C. (1993). "Cover cracking as a function of rebar corrosion: part 2—numerical model." *Materials and Structures*, **26**, 532–548.

Morinaga, S. (1988). "Prediction of service lives of reinforced concrete buildings based on the rate of corrosion." Special Report No. 23, Institute of Technology, Shimuzu Corporation.

Noghabai, K. (1995). *Splitting of Concrete in the Anchoring Zone of Deformed Bars – A*

Fracture Mechanics Approach to Bond. Licentiate thesis, Dept. of Civil Engineering, Luleå University of Technology.

Pantazopoulou, S.J., and Papoulia, K.D. (2001). "Modeling cover-cracking due to reinforcement corrosion in RC structures." *Journal of Engineering Mechanics*, **127**(4), 342–351.

Reinhardt, H. (1992). "Bond of steel to strain-softening concrete taking account of loading rate." *Fracture Mechanics of Concrete Structures*, Z. Bažant (ed.), Elsevier Applied Science, Essex, England, 809–820.

Rosati, G., and Schumm, C. (1992). "Modeling of local bond to concrete bond in reinforced concrete beams," *Bond in Concrete*, Vol. 3, A. Skudra and A. Tepfers, eds., Riga Technical University, Riga, Latvia, 34–43.

Rosenberg, A., Hansson, C., and Andrade, C. (1989). "Mechanisms of corrosion of steel in concrete". Materials Science of Concrete I, J. Skalny (ed.), The American Ceramic Society, Westerville, OH, 285–313.

Seki, H., and Oya, T. (1996). "Estimation of service life on concrete bridge." *Concrete for Infrastructure and Utilities*, R. Dhir and N. Henderson (eds.), E & FN Spon, London, UK, 73–82.

Tepfers, R. (1979). "Cracking of concrete cover along anchored deformed reinforcing bars." *Magazine of Concrete Research*, **31**(106), 3–12.

Timoshenko, S. (1956). *Strength of Materials. Part II: Advanced Theory and Problems* (3rd ed.). D. van Nostrand Company, Princeton, New Jersey.

Tuutti, K. (1982). *Corrosion of Steel in Concrete.* Swedish Cement and Concrete Research Institute, Stockholm.

Van der Veen. (1990). "Model for tensile strength in cracked concrete." *Journal of the Structural Engineering*, **137**(4), 222–248.

Willianmson, S.J. and Clark, L.A. (2000). "Pressure required to cause cover cracking of concrete due to reinforcement corrosion." *Magazine of Concrete Research*, **52**(6), 455–467.

Zhou, K. (2005). *Models for Predicting Corrosion-Induced Cracking, Spalling/Delamination of Rehabilitated RC Bridge Decks.* Master thesis, Dept. of Civil Engineering, University of Ottawa.

Appendix A

Table A1: Results for group 1

NSC d=8mm c=4mm c/d=0.5 $\frac{d}{2}<e<c+\frac{d}{2}$ n=2											
	e	4	4.5	5	5.5	6	6.5	7	7.5	8	p_{bmax}
Eq. 3.26	p_b	2.28	2.70	3	3.28	3.48	3.62	3.7	3.74	3.75	3.75
Eq. 3.41 $e<r_s<c+r_d$	p_b	4.62	5.57	6.4	7.2	7.9	8.53	9.05	9.49	9.85	9.85
Eq. 3.47 $r_d<r_s<e$	p_b	25.5	26	26.5	26.9	27.2	27.5	27..7	27.9	28.1	28.1

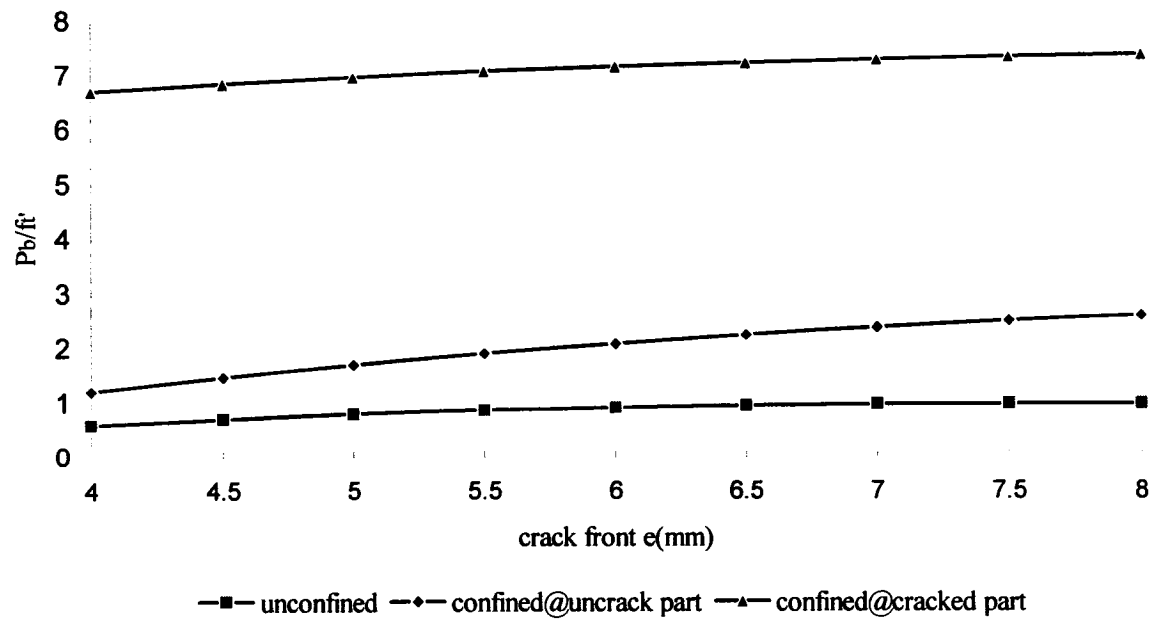

Fig. A1: Illustration of p_b/f_i' versus crack front e for group 1

Table A2: Results for group 2

NSC d=8mm c=8mm c/d=1 $\frac{d}{2}<e<c+\frac{d}{2}$ n=2											
	e	4	5	6	7	8	9	10	11	12	p_{bmax}
Eq.3.26	p_b	3.04	4.29	5.3	6.09	6.67	7.06	7.3	7.4	7.4	7.4
Eq.3.41 $e<r_s<c+r_d$	p_b	4.28	6.19	7.92	9.42	10.6	11.7	12.5	13.1	13.5	13.5
Eq.3.47 $r_d<r_s<e$	p_b	26.2	27.8	29	30.1	31	31.7	32.2	32.6	32.9	32.9

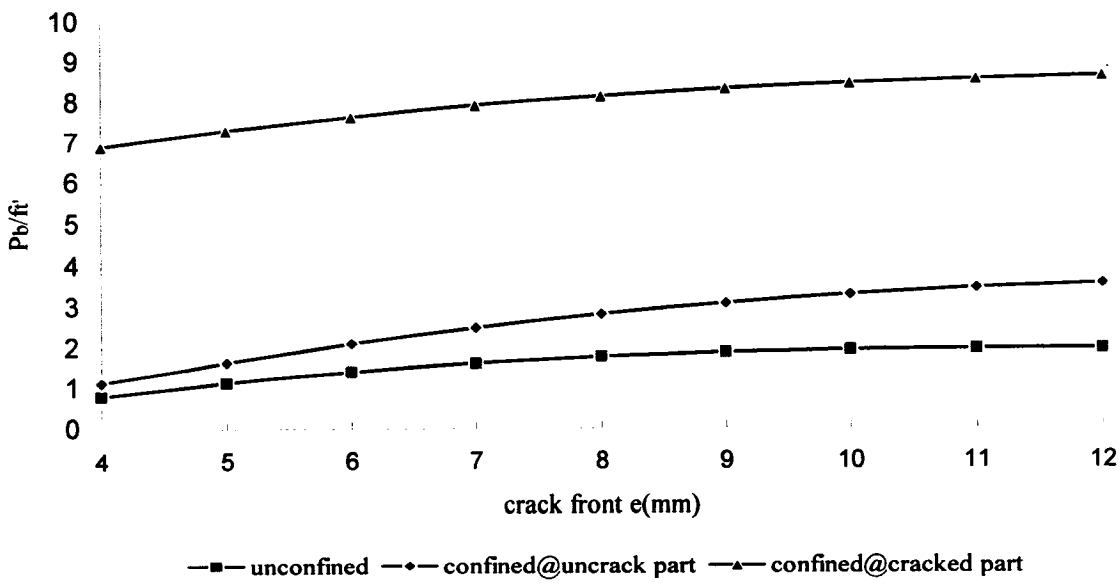

Fig. A2: Illustration of p_b/f_t' versus crack front e for group 2

Table A3: Results for group 3

NSC d=8mm c=12mm c/d=1.5 $\frac{d}{2}<e<c+\frac{d}{2}$ n=2											
	e	4	5.5	7	8.5	10	11.5	13	14.5	16	p_{bmax}
Eq.3.26	p_b	3.35	5.5	7.3	8.7	9.75	10.4	10.8	11	10.9	11
Eq.3.41 $e<r_s<c+r_d$	p_b	4.1	7	9.6	11.8	13.6	15	16	16.6	17	17
Eq.3.47 $r_d<r_s<e$	p_b	26.5	29.1	31.4	33.2	34.7	35.8	36.6	37.2	37.6	37.6

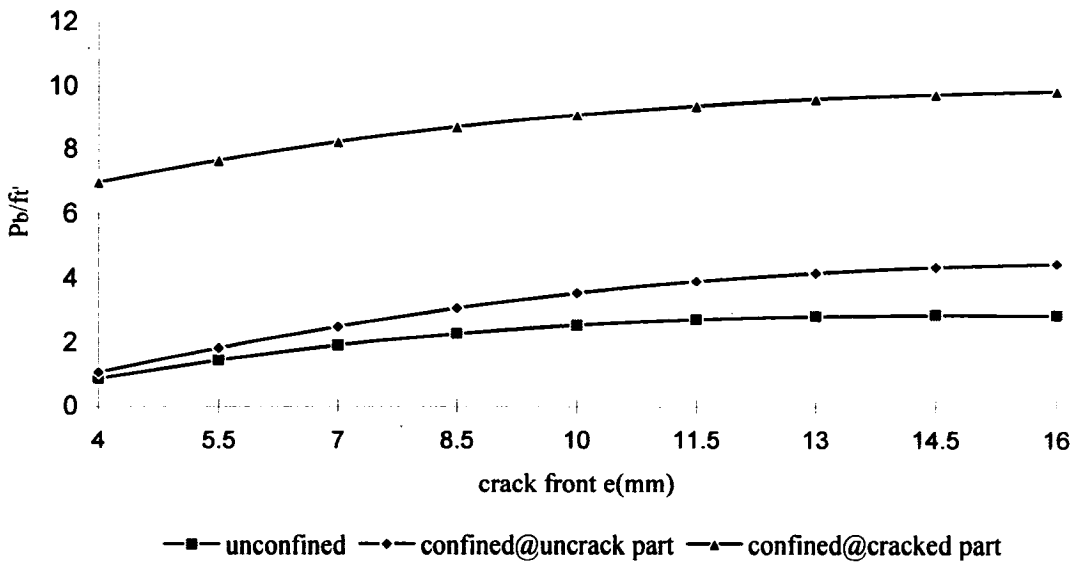

Fig. A3: Illustration of p_b/f_t' versus crack front e for group 3

Table A4: Results for group 4

NSC d=8mm c=16mm c/d=2 $\frac{d}{2}<e<c+\frac{d}{2}$ n=2											
	e	4	6	8	10	12	14	16	18	20	p_{bmax}
Eq.3.26	p_b	3.5	6.6	9.3	11.3	12.8	13.7	14.3	14.5	14.4	14.5
Eq.3.41 $e<r_s<c+r_d$	p_b	4	7.8	11.3	14.2	16.5	18.2	19.4	20.1	20.5	20.5
Eq.3.47 $r_d<r_s<e$	p_b	26.7	30.4	33.6	36.2	38.3	39.8	40.9	41.7	42.2	42.2

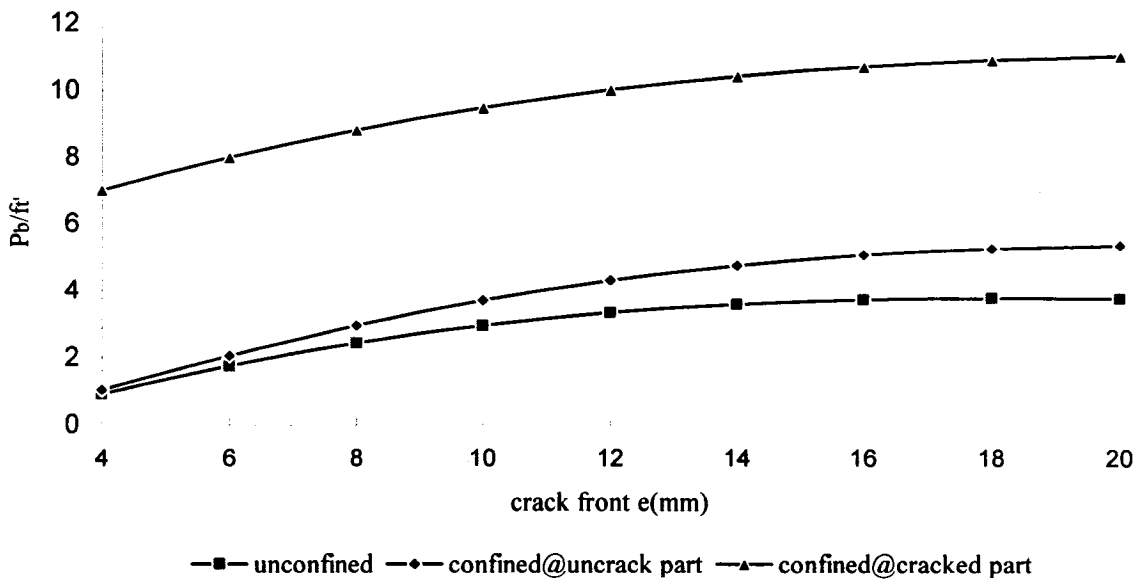

Fig. A4: Illustration of p_b/f_t' versus crack front e for group 4

Table A5: Results for group 5

NSC d=16mm c=8mm c/d=0.5 $\frac{d}{2}<e<c+\frac{d}{2}$ n=2											
	e	8	9	10	11	12	13	14	15	16	p_{bmax}
Eq.3.26	p_b	2.28	2.7	3	3.3	3.5	3.6	3.67	3.71	3.7	3.71
Eq.3.41 $e<r_s<c+r_d$	p_b	3.67	4.34	4.9	5.4	5.8	6.2	6.4	6.6	6.7	6.7
Eq.3.47 $r_d<r_s<e$	p_b	13.9	14.4	14.9	15.3	15.6	15.9	16.1	16.3	16.4	16.4

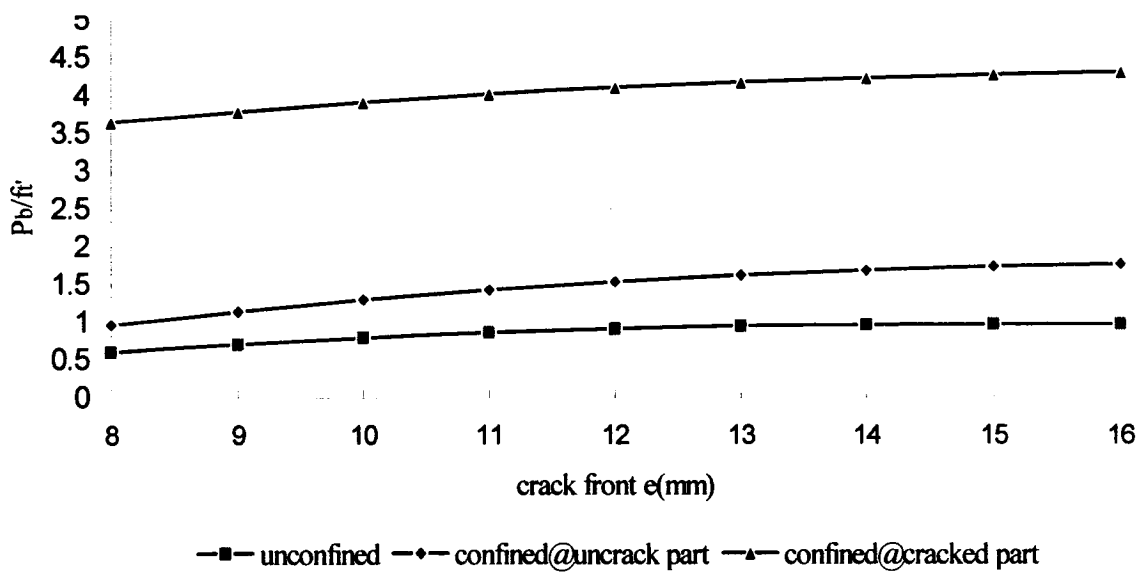

Fig. A5: Illustration of p_b/f_t' versus crack front e for group 5

Table A6: Results for group 6

NSC d=16mm c=16mm c/d=1 $\frac{d}{2}<e<c+\frac{d}{2}$ n=2											
	e	8	10	12	14	16	18	20	22	24	p_{bmax}
Eq.3.26	p_b	3	4.3	5.3	6.1	6.6	7	7.19	7.25	7.2	7.25
Eq.3.41 $e<r_s<c+r_d$	p_b	3.8	5.4	6.8	7.9	8.8	9.4	9.9	10.1	10.3	10.3
Eq.3.47 $r_d<r_s<e$	p_b	14.6	16.2	17.5	18.5	19.4	20	20.5	20.9	21	21

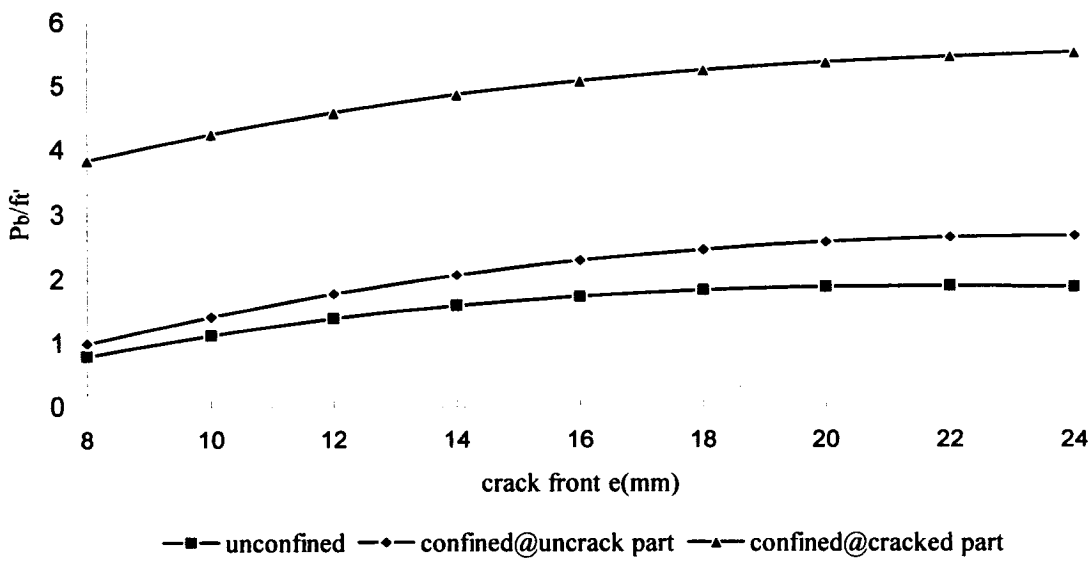

Fig. A6: Illustration of p_b/f_t' versus crack front e for group 6

Table A7: Results for group 7

NSC d=16mm c=24mm c/d=1.5 $\frac{d}{2}<e<c+\frac{d}{2}$ n=2											
	e	8	11	14	17	20	23	26	29	32	p_{bmax}
Eq.3.26	p_b	3.4	5.5	7.3	8.7	9.6	10.3	10.6	10.6	10.5	10.6
Eq.3.41 $e<r_s<c+r_d$	p_b	3.8	6.4	8.6	10.3	11.7	12.6	13.2	13.5	13.6	13.6
Eq.3.47 $r_d<r_s<e$	p_b	15	17.6	19.8	21.5	23	24	24.8	25.3	25.5	25.5

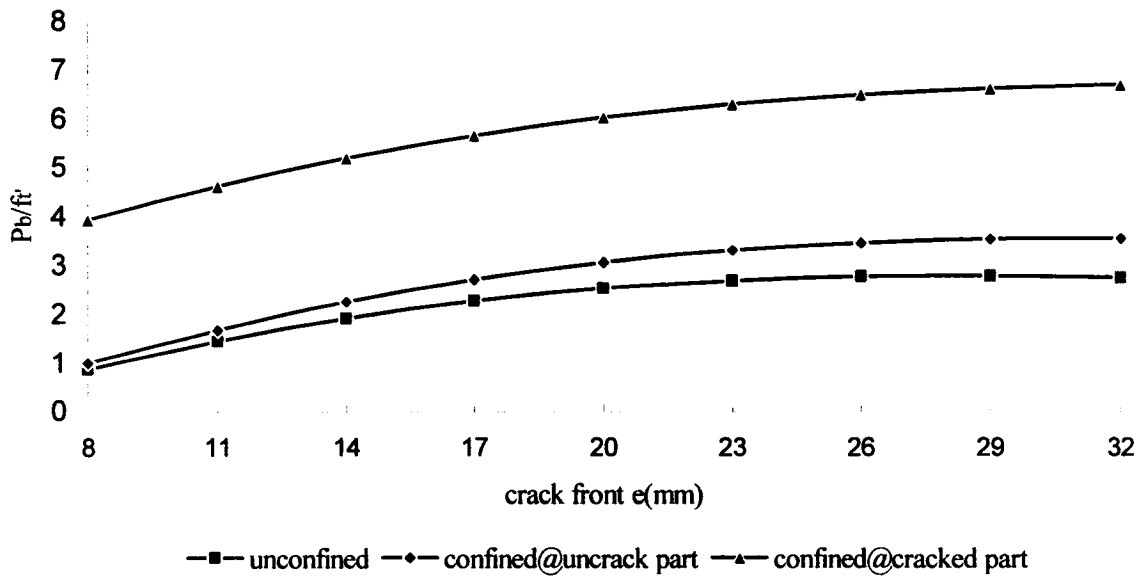

Fig. A7: Illustration of p_b/f_t' versus crack front e for group 7

Table A8: Results for group 8

NSC d=16mm c=32mm c/d=2 $\frac{d}{2}<e<c+\frac{d}{2}$ n=2											
	e	8	12	16	20	24	28	32	36	40	p_{bmax}
Eq.3.26	p_b	3.5	6.6	9.2	11.2	12.6	13.4	13.8	13.9	13.6	13.9
Eq.3.41 $e<r_s<c+r_d$	p_b	3.8	7.3	10.3	12.7	14.5	15.7	16.4	16.7	16.6	16.7
Eq.3.47 $r_d<r_s<e$	p_b	15.1	18.8	21.9	24.4	26.5	27.9	28.9	29.5	29.8	29.8

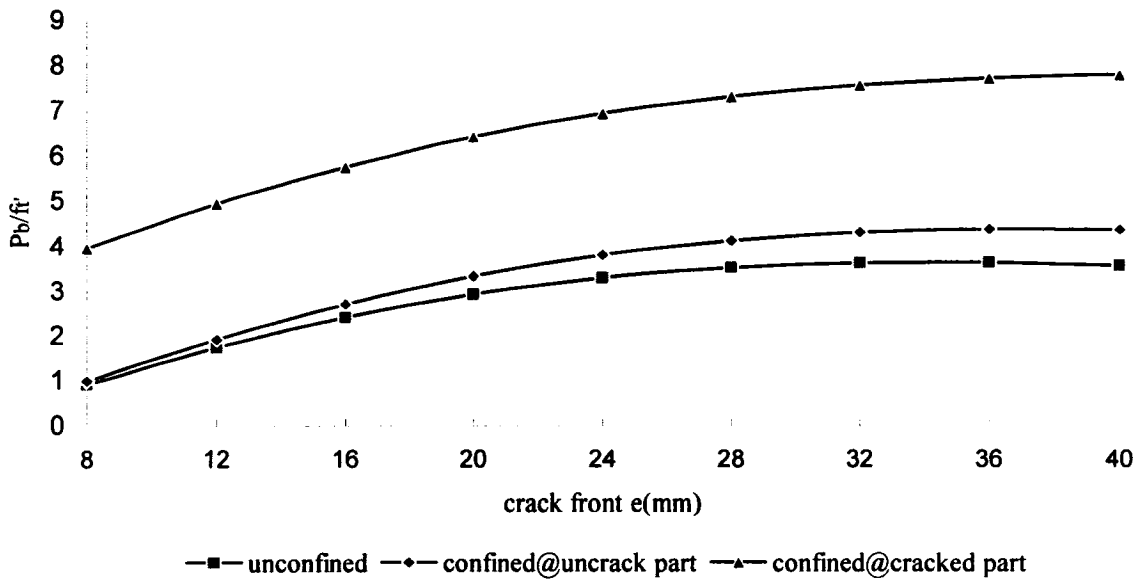

Fig. A8: Illustration of p_b/f_i' versus crack front e for group 8

Table A9: Results for group 9

HSC d=8mm c=4mm c/d=0.5 $\frac{d}{2}<e<c+\frac{d}{2}$ n=2											
	e	4	4.5	5	5.5	6	6.5	7	7.5	8	p_{bmax}
Eq.3.26	p_b	3.5	4	4.3	4.5	4.7	4.8	4.9	4.92	4.93	4.93
Eq.3.41 $e<r_s<c+r_d$	p_b	5.7	6.8	7.9	8.8	9.6	10.2	10.8	11.3	11.7	11.7
Eq.3.47 $r_d<r_s<e$	p_b	36.6	37.4	38	38.6	39	39.4	39.8	40	40.2	40.2

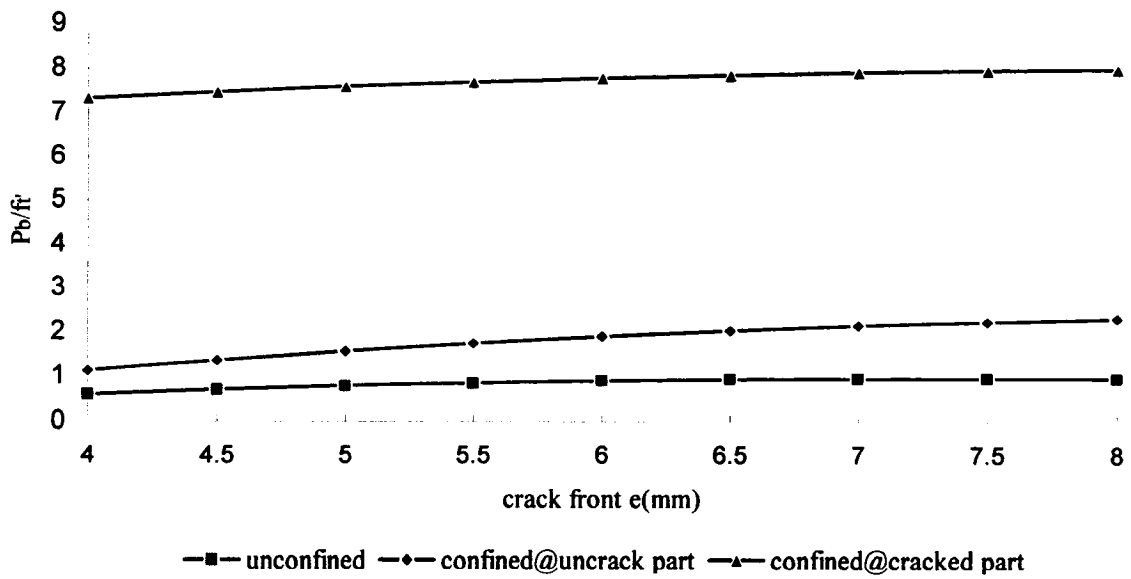

Fig. A9: Illustration of p_b/f_t' versus crack front e for group 9

Table A10: Results for group 10

HSC d=8mm c=8mm c/d=1 $\frac{d}{2}<e<c+\frac{d}{2}$ n=2											
	e	4	5	6	7	8	9	10	11	12	p_{bmax}
Eq.3.26	p_b	4	5.6	7	8	8.7	9.3	9.6	9.73	9.72	9.73
Eq.3.41 $e<r_s<c+r_d$	p_b	5.4	7.9	10	11.7	13.2	14.5	15.4	16	16.4	16.4
Eq.3.47 $r_d<r_s<e$	p_b	37.6	40	41	43	44	45	45.7	46.3	46.7.	46.7

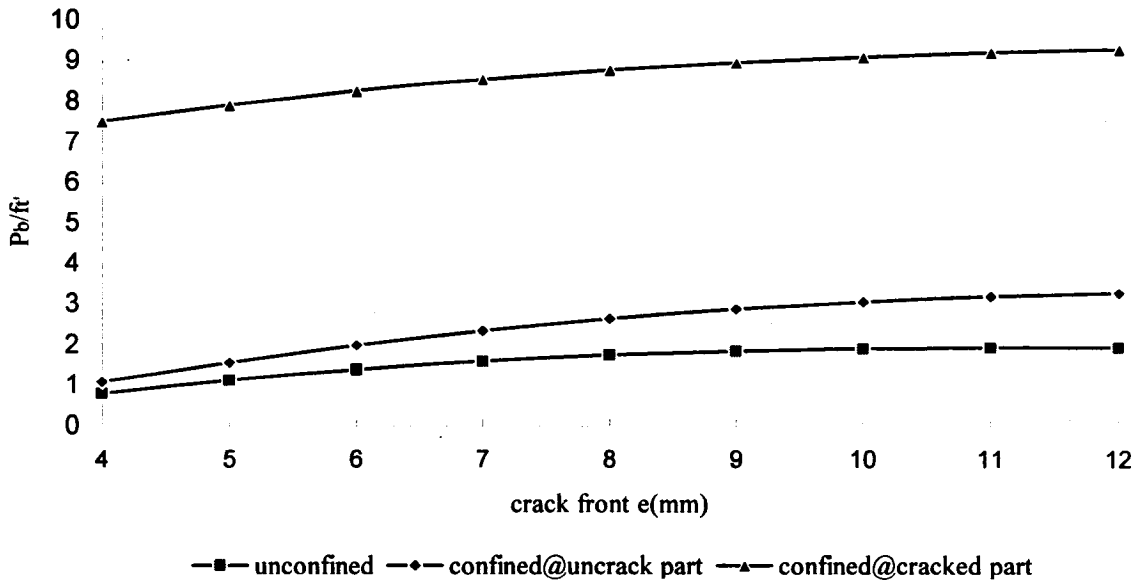

Fig. A10: Illustration of p_b/f_t' versus crack front e for group 10

Table A11: Results for group 11

HSC d=8mm c=12mm c/d=1.5 $\frac{d}{2}<e<c+\frac{d}{2}$ n=2											
	e	4	5.5	7	8.5	10	11.5	13	14.5	16	p_{bmax}
Eq.3.26	p_b	4.4	7.3	9.6	11.4	12.8	13.7	14.2	14.3	14.2	14.3
Eq.3.41 $e<r_s<c+r_d$	p_b	5.3	9	12.2	15	17.1	18.8	19.9	20.7	21.1	21.1
Eq.3.47 $r_d<r_s<e$	p_b	38	41.5	44.5	47	49	50.5	51.6	52.4	53	53

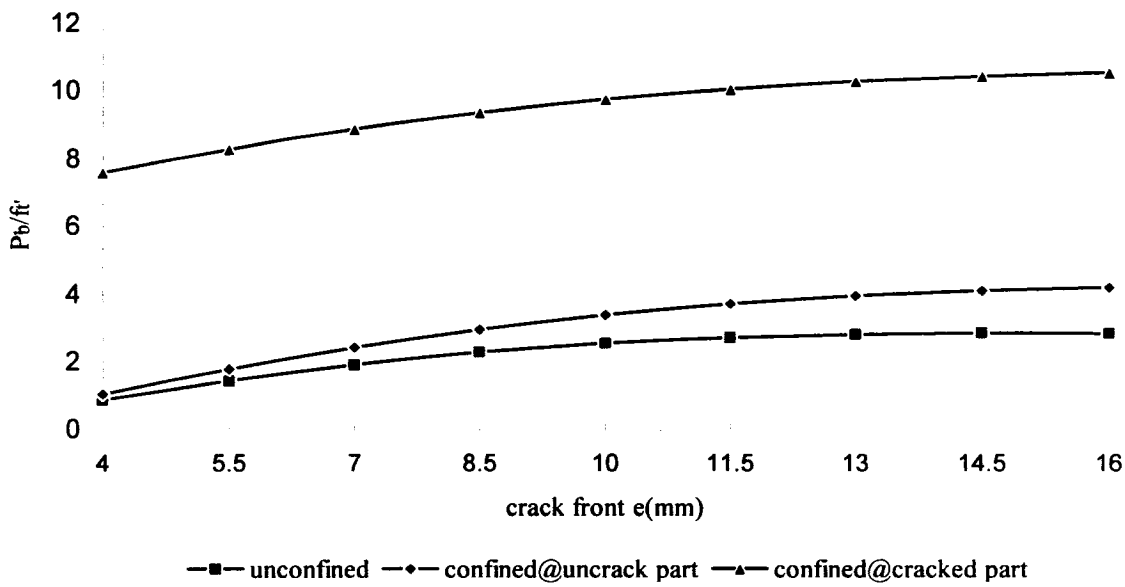

Fig. A11: Illustration of p_b/f_t' versus crack front e for group 11

Table A12: Results for group 12

HSC d=8mm c=16mm c/d=2 $\frac{d}{2}<e<c+\frac{d}{2}$ n=2											
	e	4	6	8	10	12	14	16	18	20	p_{bmax}
Eq.3.26	p_b	4.6	8.7	12.2	14.8	16.8	18	18.8	19	18.9	19
Eq.3.41 $e<r_s<c+r_d$	p_b	5.2	10.1	14.5	18	20.9	23	24.4	25.3	25.6	25.6
Eq.3.47 $r_d<r_s<e$	p_b	38.2	43	47.5	51	53.8	55.9	57.4	58.5	59.2	59.2

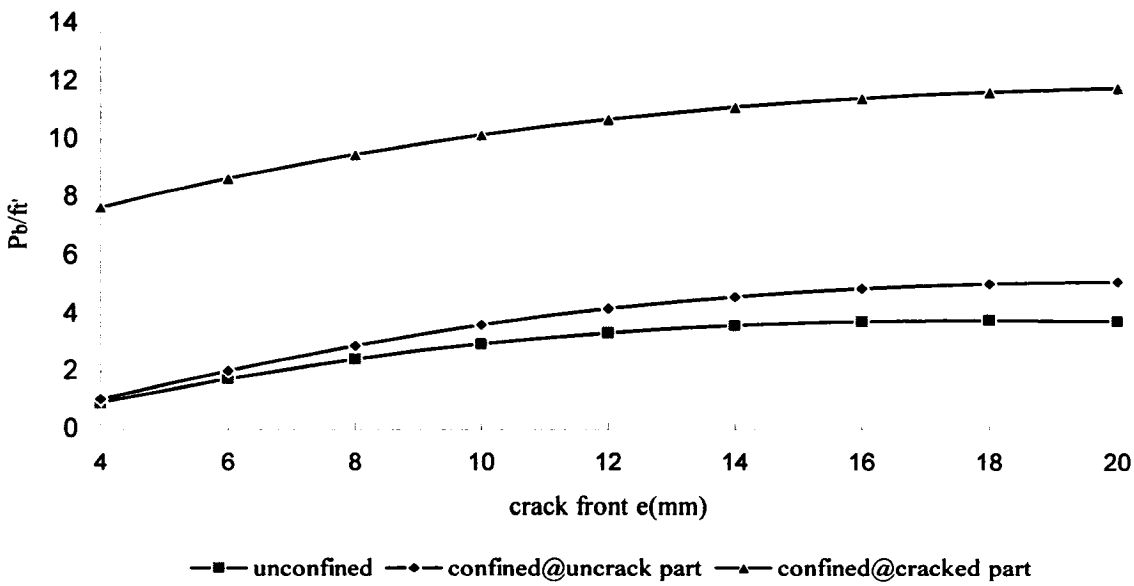

Fig. A12: Illustration of p_b/f_t' versus crack front e for group 12

Table A13: Results for group 13

HSC d=16mm c=8mm c/d=0.5 $\frac{d}{2}<e<c+\frac{d}{2}$ n=2											
	e	8	9	10	11	12	13	14	15	16	p_{bmax}
Eq.3.26	p_b	3	3.5	4	4.3	4.6	4.7	4.8	4.87	4.86	4.87
Eq.3.41 $e<r_s<c+r_d$	p_b	4.6	5.4	6.1	6.7	7.2	7.5	7.9	8	8.2	8.2
Eq.3.47 $r_d<r_s<e$	p_b	20	20.6	21.2	21.7	22.2	22.6	23	23.1	23.3	23.3

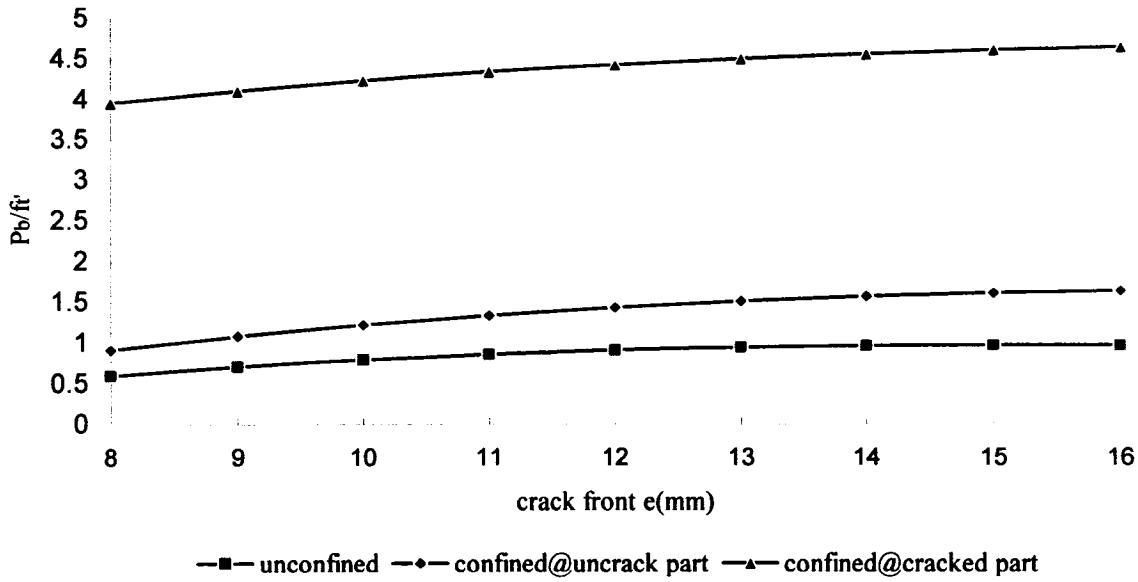

Fig. A13: Illustration of p_b/f_t' versus crack front e for group 13

Table A14: Results for group 14

HSC d=16mm c=16mm c/d=1 $\frac{d}{2}<e<c+\frac{d}{2}$ n=2											
	e	8	10	12	14	16	18	20	22	24	p_{bmax}
Eq.3.26	p_b	4	5.6	7	8	8.7	9.1	9.4	9.5	9.45	9.5
Eq.3.41 $e<r_s<c+r_d$	p_b	4.9	7	8.6	10	11	11.9	12.4	12.7	12.8	12.8
Eq.3.47 $r_d<r_s<e$	p_b	20.8	22.9	24.6	26	27.2	28	28.8	29.3	29.6	29.6

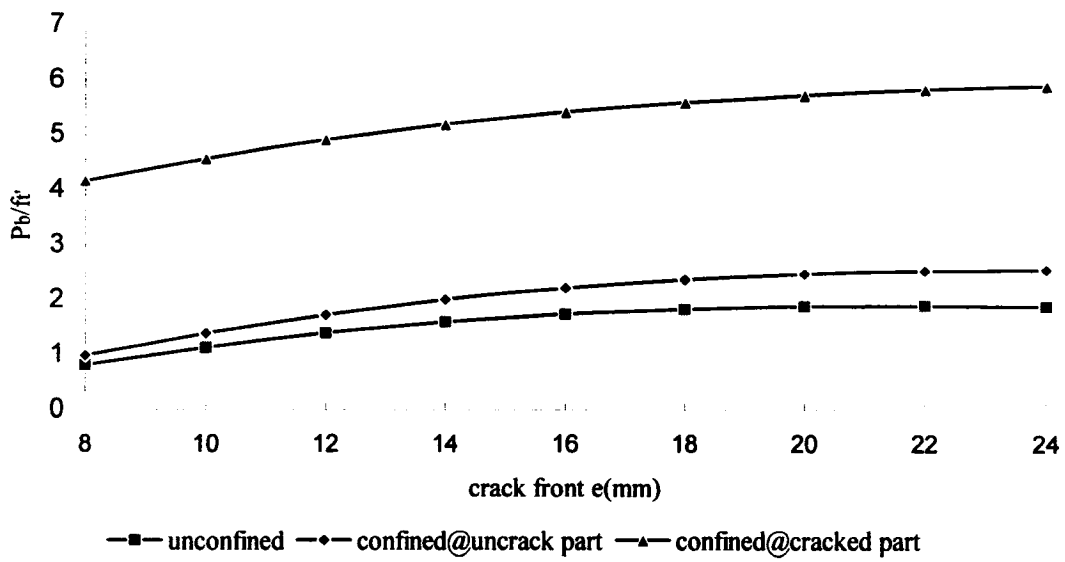

Fig. A14: Illustration of p_b/f_t' versus crack front e for group 14

Table A15: Results for group 15

HSC d=16mm c=24mm c/d=1.5 $\frac{d}{2}<e<c+\frac{d}{2}$ n=2											
	e	8	11	14	17	20	23	26	29	32	p_{bmax}
Eq.3.26	p_b	4.4	7.3	9.6	11.4	12.6	13.5	13.9	14	13.7	14
Eq.3.41 $e<r_s<c+r_d$	p_b	5	8.2	11	13.3	14.9	16	16.7	17.1	17.1	17.1
Eq.3.47 $r_d<r_s<e$	p_b	21.2	24.7	27.7	30	32	33.5	34.4	35.1	35.6	35.6

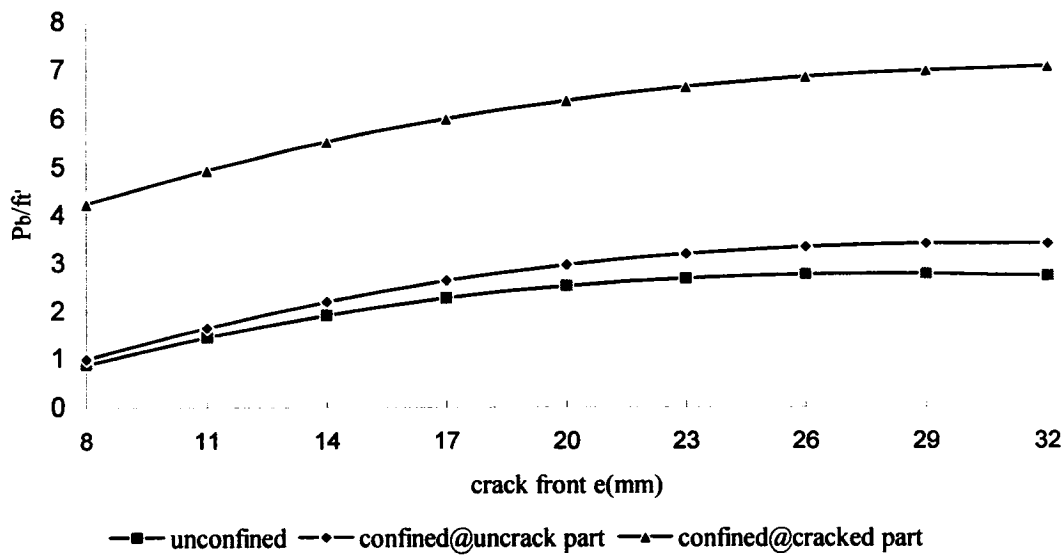

Fig. A15: Illustration of p_b/f_t' versus crack front e for group 15

Table A16: Results for group 16

HSC d=16mm c=32mm c/d=2 $\frac{d}{2}<e<c+\frac{d}{2}$ n=2											
	e	8	12	16	20	24	28	32	36	40	p_{bmax}
Eq.3.26	p_b	4.6	8.3	12.1	14.7	16.5	17.6	18.1	18.2	17.8	18.2
Eq.3.41 $e<r_s<c+r_d$	p_b	5	9.5	13.4	16.4	18.7	20.2	21	21.3	21.2	21.3
Eq.3.47 $r_d<r_s<e$	p_b	21.4	26.4	30.6	34	36.7	38.6	40	40.8	41.3	41.3

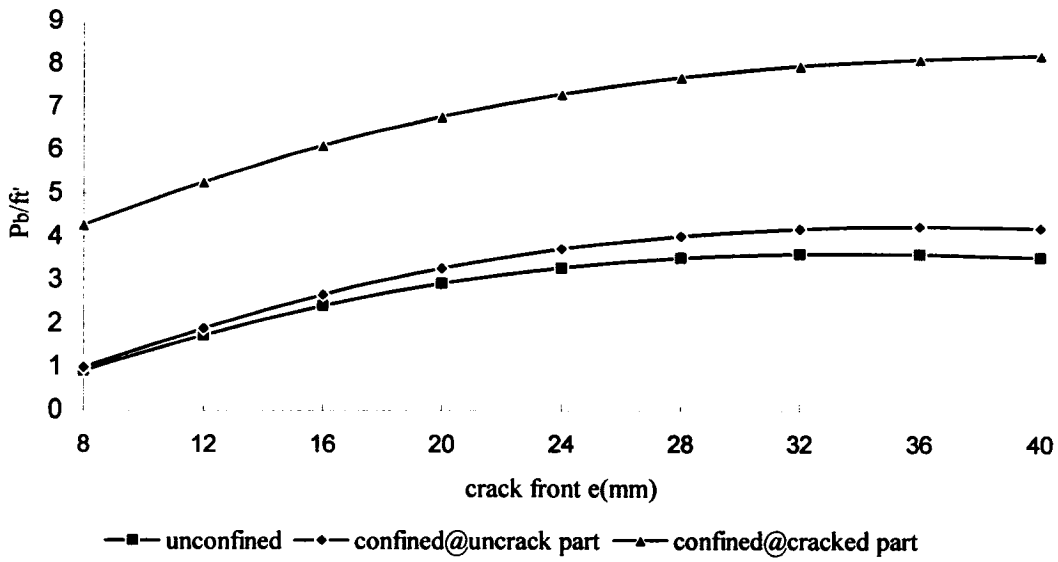

Fig. A16: Illustration of p_b/f_t' versus crack front e for group 16

Table A17: Results for group 17

VHSC d=8mm c=4mm c/d=0.5 $\frac{d}{2}<e<c+\frac{d}{2}$ n=2											
	e	4	4.5	5	5.5	6	6.5	7	7.5	8	p_{bmax}
Eq.3.26	p_b	4.8	5.7	6.4	6.9	7.3	7.6	7.7	7.9	7.7	7.9
Eq.3.41 $e<r_s<c+r_d$	p_b	9	10.8	12.4	13.8	15	16	16.8	17.5	18	18
Eq.3.47 $r_d<r_s<e$	p_b	87.2	88.5	89.7	90.8	91.7	92.5	93.2	93.7	94.2	94.2

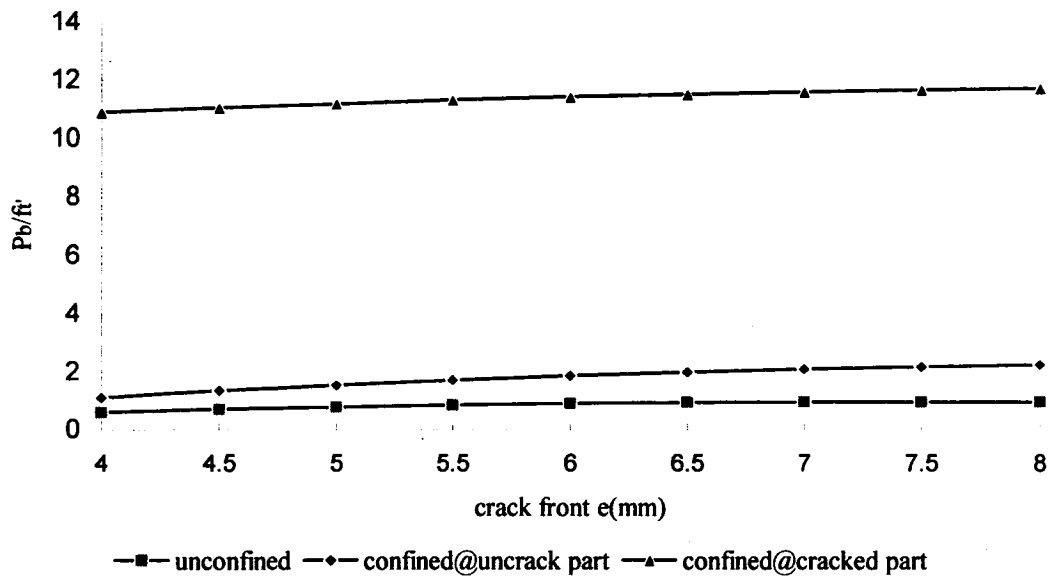

Fig. A17: Illustration of p_b/f_t' versus crack front e for group 17

Table A18: Results for group 18

VHSC d=8mm c=8mm c/d=1 $\frac{d}{2}<e<c+\frac{d}{2}$ n=2											
	e	4	5	6	7	8	9	10	11	12	p_{bmax}
Eq.3.26	p_b	6.4	9	11.1	12.8	13.9	14.7	15	15.2	15.1	15.2
Eq.3.41 $e<r_s<c+r_d$	p_b	8.7	12.4	15.8	18.6	21	22.6	23.9	24.8	25.4	25.4
Eq.3.47 $r_d<r_s<e$	p_b	88.8	92.4	95.5	98.2	100	102	103	105	106	106

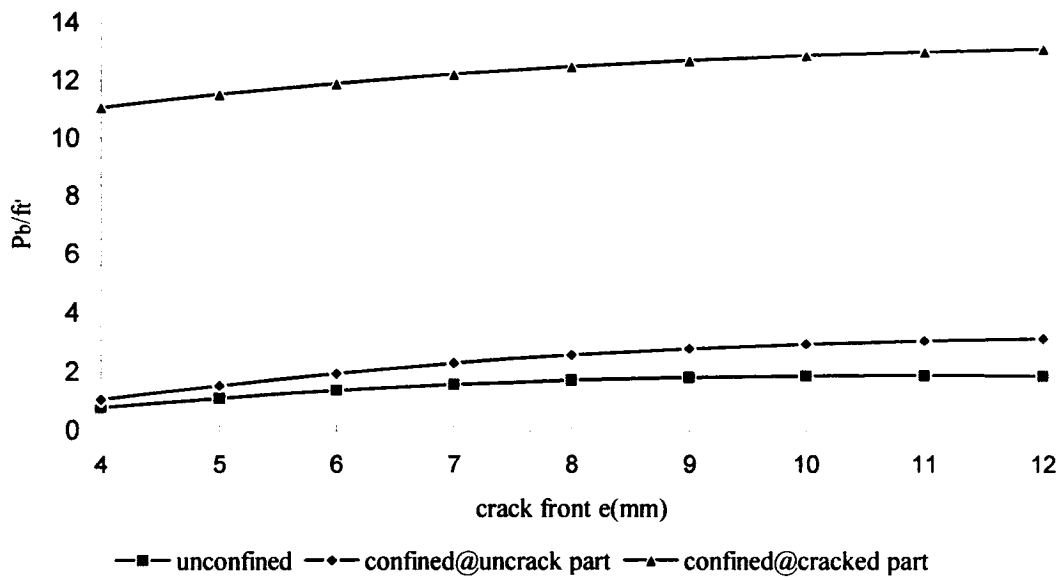

Fig. A18: Illustration of p_b/f_t' versus crack front e for group 18

Table A19: Results for group 19

VHSC d=8mm c=12mm c/d=1.5 $\frac{d}{2}<e<c+\frac{d}{2}$ n=2											
	e	4	5.5	7	8.5	10	11.5	13	14.5	16	p_{bmax}
Eq.3.26	p_b	7	11.6	15.4	18.2	20.3	21.5	22.2	22.3	21.9	22.3
Eq.3.41 $e<r_s<c+r_d$	p_b	8.4	14.2	19.3	23.5	26.8	29.3	3.9	31.9	32.2	32.2
Eq.3.47 $r_d<r_s<e$	p_b	89.4	95.5	101	105	109	112	114	115	117	117

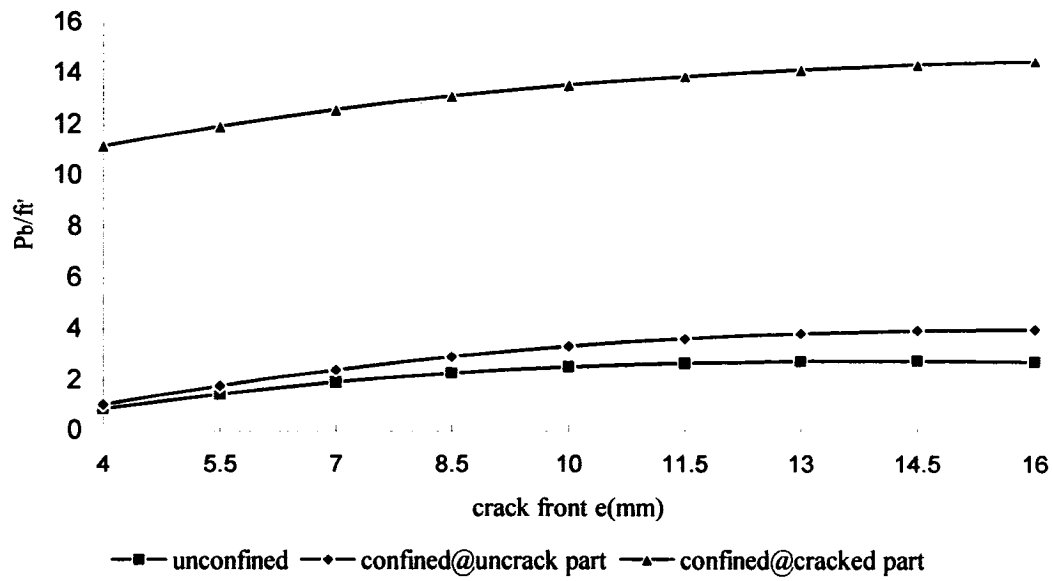

Fig. A19: Illustration of p_b/f_t' versus crack front e for group 19

Table A20: Results for group 20

VHSC d=8mm c=16mm c/d=2 $\frac{d}{2}<e<c+\frac{d}{2}$ n=2											
	e	4	6	8	10	12	14	16	18	20	p_{bmax}
Eq.3.26	p_b	7.4	14	19.4	23.5	26.4	28.2	29	29	28.4	29
Eq.3.41 $e<r_s<c+r_d$	p_b	8.3	16.1	22.9	28.5	32.7	35.8	37.7	38.6	38.7	38.7
Eq.3.47 $r_d<r_s<e$	p_b	89.7	98.4	106	112	117	121	124	126	127	127

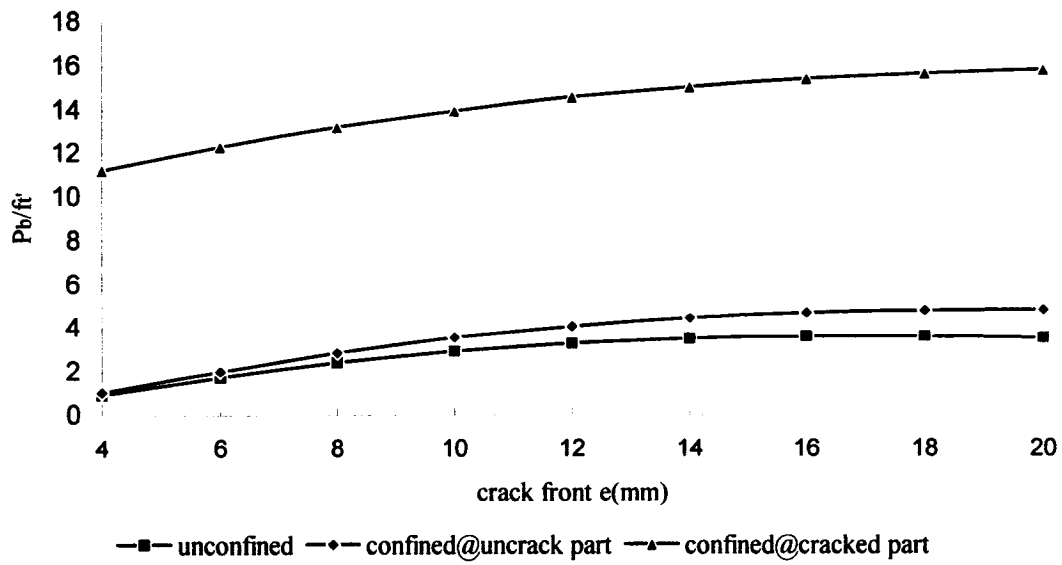

Fig. A20: Illustration of p_b/f_t' versus crack front e for group 20

Table A21: Results for group 21

VHSC d=16mm c=8mm c/d=0.5 $\frac{d}{2}<e<c+\frac{d}{2}$ n=2											
	e	8	9	10	11	12	13	14	15	16	p_{bmax}
Eq.3.26	p_b	4.8	5.7	6.4	6.8	7.2	7.5	7.6	7.6	7.5	7.6
Eq.3.41 $e<r_s<c+r_d$	p_b	7.2	8.5	9.6	10.6	11.3	11.9	12.3	12.5	12.7	12.7
Eq.3.47 $r_d<r_s<e$	p_b	45.9	47.3	48.6	49.6	50.5	51.2	51.8	52.4	52.8	52.8

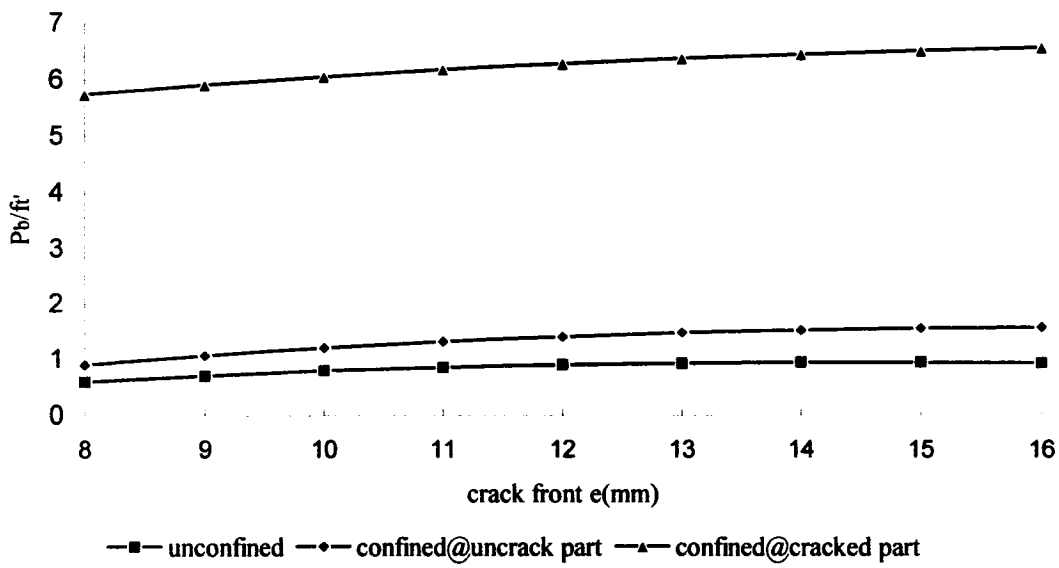

Fig. A21: Illustration of p_b/f_t' versus crack front e for group 21

Table A22: Results for group 22

VHSC d=16mm c=16mm c/d=1 $\frac{d}{2}<e<c+\frac{d}{2}$ n=2											
	e	8	10	12	14	16	18	20	22	24	p_{bmax}
Eq.3.26	p_b	6.4	9	11	12.6	13.7	14.3	14.6	14.5	14.2	14.6
Eq.3.41 $e<r_s<c+r_d$	p_b	7.7	11	13.6	15.8	17.4	18.4	19.1	19.4	19.3	19.4
Eq.3.47 $r_d<r_s<e$	p_b	47.6	51.2	54.3	56.9	59	60.6	62	62.8	63.5	63.5

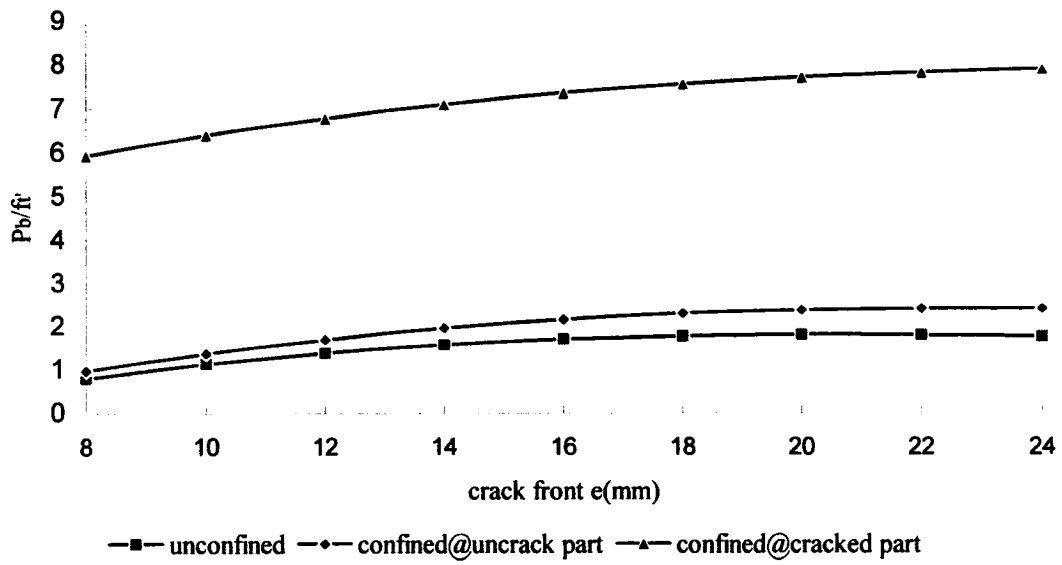

Fig. A22: Illustration of p_b/f_t' versus crack front e for group 22

Table A23: Results for group 23

VHSC d=16mm c=24mm c/d=1.5 $\frac{d}{2}<e<c+\frac{d}{2}$ n=2											
	e	8	11	14	17	20	23	26	29	32	p_{bmax}
Eq.3.26	p_b	7.1	11.6	15.2	18	19.7	20.7	21	20.7	20	21
Eq.3.41 $e<r_s<c+r_d$	p_b	7.9	13.1	17.4	20.8	23.2	24.7	25.5	25.5	25.1	25.5
Eq.3.47 $r_d<r_s<e$	p_b	48.2	54.3	59.5	63.7	67	70	71.4	72.6	73.3	73.3

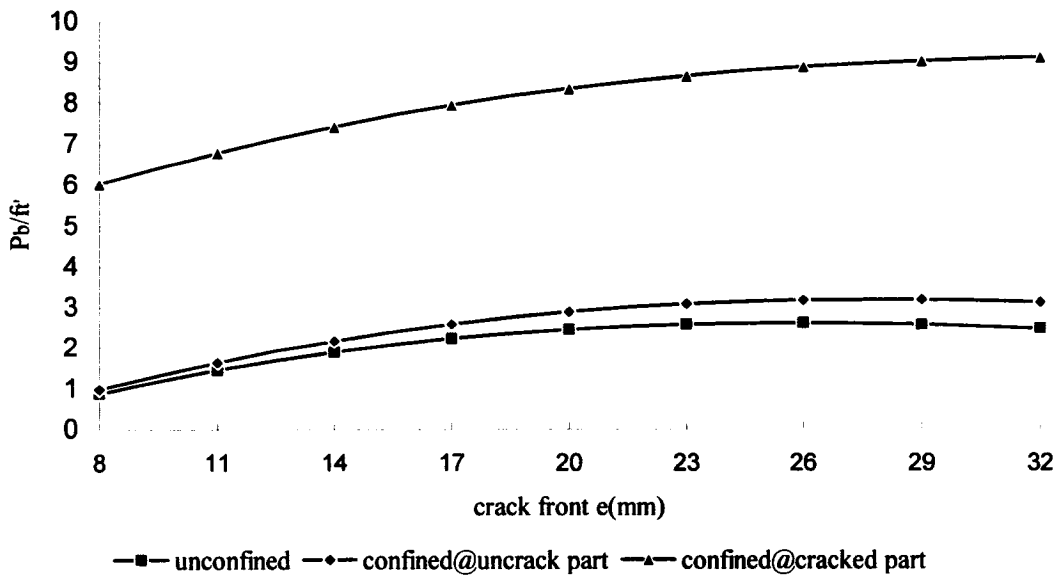

Fig. A23: Illustration of p_b/f_t' versus crack front e for group 23

Table A24: Results for group 24

VHSC d=16mm c=32mm c/d=2 $\frac{d}{2}<e<c+\frac{d}{2}$ n=2											
	e	8	12	16	20	24	28	32	36	40	p_{bmax}
Eq.3.26	p_b	7.4	14	19.1	23	25.5	26.7	27	26.2	24.7	27
Eq.3.41 $e<r_s<c+r_d$	p_b	8	15.1	21.1	25.6	28.8	30.7	31.4	31	30	31.4
Eq.3.47 $r_d<r_s<e$	p_b	48.5	57.1	64.4	70.3	74.8	78.1	80.3	81.6	82.2	82.2

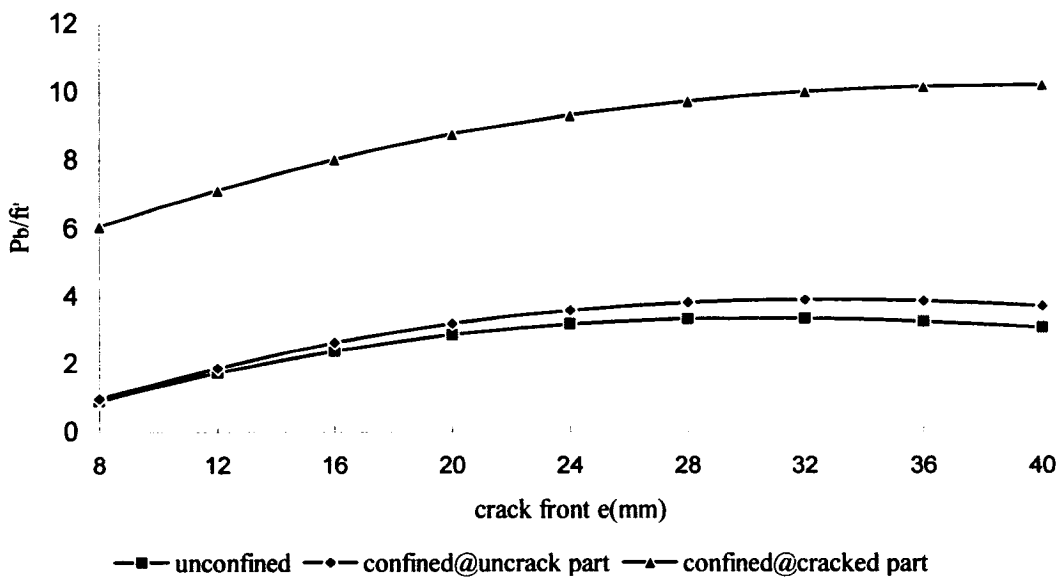

Fig. A24: Illustration of p_b/f_t' versus crack front e for group 24